Functionalization of Reactive Surfaces and of Metal-Supported Graphene using N-heterocyclic Carbenes

Thèse

Tianchi Zhang

Doctorat en chimie
Philosophiæ doctor (Ph. D.)

Québec, Canada

Functionalization of Reactive Surfaces and of Metal-Supported Graphene using N-heterocyclic Carbenes

Tianchi Zhang

Doctorat en chimie

Philosophiæ doctor (Ph. D.)

Directeur de recherche

Prof. Dr. Peter McBreen

Résumé

Cette thèse rapporte des études de la fonctionnalisation covalente des surfaces du groupe Pt, du graphène supporté par un métal et du carbure de molybdène bidimensionnel (2D) à l'aide de carbènes. Des mesures de spectroscopie photoélectronique à rayons X (XPS) et de spectroscopie infrarouge d'absorption par réflexion (RAIRS) ont été utilisées pour explorer la liaison covalente entre les carbènes N-hétérocycliques (NHC) et Pt(111), Ru(0001), graphène (Gr) sur Pt(111), Gr sur des surfaces Ru(0001) et 2D-Mo_2C. La formation, l'orientation de l'adsorption et la stabilité thermique du NHC lié à la surface ont été étudiées dans chaque cas. Le sel précurseur utilisé dans la plupart des expériences était l'hydrogénocarbonate de 1,3-diisopropyl-6-(trifluorométhyl)-1H-benzo[d]imidazol-3-ium. Un état à plat et un état orienté verticalement ont été observés sur Pt(111) et Ru(0001) après adsorption du précurseur à température ambiante. Le signal pour les états orientés verticalement a été détecté au-dessus de 600 K. Il a été constaté que les groupes de bout d'aile isopropyle subissaient une rupture de liaison à 400-450 K sur Pt(111) et Ru(0001) avec rétention du noyau du squelette NHC. L'adsorption du précurseur sur Gr/Pt(111) et Gr/Ru(0001) a entraîné une fonctionnalisation covalente, formant un état NHC à plat. Le NHC greffé se forme proprement sur les deux systèmes, indiquant que le transfert d'électrons réduit le sel précurseur et que la couche de graphène protège également contre la décomposition du NHC. La stabilité thermique du NHC greffé est similaire à celle rapportée pour les groupes aryle greffés en utilisant la méthode au diazonium. Les différences observées entre la stabilité thermique du NHC greffé sur les deux surfaces sont attribuées à la formation d'une couche de graphène dopé n sur Ru(0001) et d'une couche dopée p sur Pt(111). La formation de NHC a été utilisée pour sonder l'intercalation d'oxygène et la gravure induite par l'oxygène de la couche de graphène sur Ru (0001). L'intercalation d'oxygène s'est avérée transformer le système Gr/Ru(0001) en un système démontrant les mêmes propriétés d'adsorption que pour Gr/Pt(111). Une série de mesures a été effectuée sur 2D-Mo_2C sur des échantillons de cuivre qui ont été préparés par une méthode de dépôt chimique en phase vapeur (CVD). Des protocoles pour nettoyer les échantillons 2D-Mo_2C/Cu en éliminant l'excès de carbone ont été explorés, en se concentrant sur le traitement à l'hydrogène atomique et la pulvérisation ionique O/Ar. Le traitement à l'hydrogène atomique a été efficace pour réduire la contamination par le carbone, mais un excès de carbone est resté après le traitement. La pulvérisation ionique O/Ar a été efficace pour éliminer l'excès de carbone. Un recuit supplémentaire à haute température (1100 K) après les deux traitements a fortement réduit la teneur en oxygène. En raison des fortes propriétés de donneur σ des ligands NHC, les NHC peuvent se lier faiblement au carbone de surface après un traitement à l'hydrogène atomique. En revanche, le NHC a pu former une forte interaction avec 2D-Mo_2C/Cu à 300 K après un traitement de pulvérisation ionique O/Ar. L'interaction du précurseur NHC avec des échantillons pulvérisés Ar/O_2 a produit de faibles signaux NHC compatibles avec une décomposition moléculaire étendue sur la surface réactive. Des expériences supplémentaires ont été réalisées pour explorer l'utilisation de la scission de liaison carbonyle dans le benzaldéhyde portant un substituant CF_3 aux positions méta (3-CF_3) ou para

(4-CF_3) pour préparer des groupes carbène sur 2D-Mo_2C. Des expériences utilisant du 3-CF_3-benzaldéhyde et du 4-CF_3-benzaldéhyde indiquent que cette méthode, produisant des alkylidènes de surface, est plus prometteuse que la méthode NHC. Le 3-CF_3-benzaldéhyde et le 4-CF_3-benzaldéhyde ont été désoxygénés sur 2D-Mo_2C/Cu à 250 K, ce qui a donné du styrylidène et de l'O co-adsorbés dans les deux cas.

Abstract

This thesis reports studies of the covalent functionalization of Pt-group surfaces, metal-supported graphene and two-dimensional (2D) molybdenum carbide using carbenes. X-ray photoelectron spectroscopy (XPS) and reflection absorption infrared spectroscopy (RAIRS) measurements were used to explore covalent bonding between N-heterocyclic carbenes (NHCs) and Pt(111), Ru(0001), graphene (Gr) on Pt(111), Gr on Ru(0001) and 2D-Mo_2C surfaces. The formation, adsorption orientation and thermal stability of the surface-bound NHC was investigated in each case. The precursor salt used in most of the experiments was 1,3-diisopropyl-6-(trifluoromethyl)-1H-benzo[d]imidazol-3-ium hydrogen carbonate. Both a flat-lying and a vertically oriented state were observed on Pt(111) and Ru(0001) following adsorption of the precursor at room temperature. Signal for the vertically oriented states was detected to above 600 K. The isopropyl wingtip groups were found to undergo bond breaking at 400-450 K on both Pt(111) and Ru(0001) with retention of the NHC backbone core. Adsorption of the precursor on Gr/Pt(111) and Gr/Ru(0001) resulted on covalent functionalization, forming a flat-lying NHC state. The grafted NHC is formed cleanly on both systems, indicating that electron transfer reduces the precursor salt and that the graphene layer also protects against decomposition of the NHC. The thermal stability of the grafted NHC is similar to that reported for grafted aryl groups using the diazonium method. Observed differences between the thermal stability of the grafted NHC on the two surfaces are attributed to the formation of an n-doped graphene layer on Ru(0001) and a p-doped layer on Pt(111). NHC formation was used to probe oxygen intercalation and oxygen induced etching of the graphene layer on Ru(0001). Oxygen intercalation was found to transform the Gr/Ru(0001) system to one demonstrating the same adsorption properties as for Gr/Pt(111). A series of measurements was carried out on 2D-Mo_2C on copper samples that were prepared by a chemical vapor deposition (CVD) method. Protocols to clean the 2D-Mo_2C/Cu samples by removing excess carbon were explored, focusing on atomic hydrogen treatment and O/Ar ion sputtering. Atomic hydrogen treatment was effective to reduce carbon contamination, but excess carbon still remained after the treatment. O/Ar ion sputtering was effective to remove the excess carbon. Additional high temperature annealing (1100 K) after the two treatments greatly reduced the oxygen content. Due to the strong σ-donor properties of NHC ligands, NHCs can weakly bond with surface carbon after atomic hydrogen treatment. In contrast, the NHC was able to form a strong interaction with 2D-Mo_2C/Cu at 300 K after O/Ar ion sputtering treatment. The interaction of the NHC precursor with Ar/O_2 sputtered samples produced weak NHC signals consistent with extensive molecular decomposition on the reactive surface. Additional experiments were performed to explore the use carbonyl bond scission in benzaldehyde bearing a CF_3 substituent at the meta (3-CF_3) or para (4-CF_3) positions to prepare carbene groups on 2D-Mo_2C. Experiments using 3-CF_3-benzaldehyde and 4-CF_3-benzaldehyde indicate that this method, producing surface alkylidenes, is more promising than the NHC method. 3-CF_3-benzaldehyde and 4-CF_3-benzaldehyde were deoxygenated on 2D-Mo_2C/Cu at 250 K, resulting in co-adsorbed styrylidene and O in both cases.

Table of contents

List of Tables

List of Figures

List of Schemes

Abbreviations

ABTF	Aminobenzotriflouride
AFM	Atomic Force Microscopy
CVD	Chemical Vapor Deposition
DFT	Density Functional Theory
DOS	Density of States
EC	Electrochemical
E_F	Fermi Level
fcc	Face Centered Cubic
Gr	Graphene
hcp	Hexagonal Close Packed
HOPG	Highly Oriented Pyrolytic Graphite
InSb	Indium Antimonide
LEEM	Low-Energy Electron Microscopy
MCT	Mercury-Cadmium-Telluride
NEXAFS	Near Edge X-Ray Absorption Fine Structure
NHCs	N-Heterocyclic Carbenes
NPs	Nanoparticles
RAIRS	Reflectance Absorbance Infrared Spectroscopy
SAMs	Self-Assembled Monolayers
STM	Scanning Tunneling Microscopy
THF	Tetrahydrofuran

UHV	Ultra-High Vacuum
XPS	X-Ray Photoelectron Spectroscopy

Symbols

T_x	Surface Termination Groups
E_k	Kinetic Energy (XPS)
E_b	Binding Energy (XPS)
$h\upsilon$	Photon Energy (XPS)
ΔE	Reduction in Photoelectron Kinetic Energy due to Inelastic Collisions (XPS)
n	Multiple of Energy Loss Collisions (XPS)
λ	Mean Free Path (XPS)
I_0	Signal Intensity on Photoionization (XPS)
I_d	Signal Intensity of after Distance of Travel d in the Sample (XPS)
p-	Parallel to the Plane of Incidence (RAIRS)
s-	Perpendicular to the Plane of Incidence (RAIRS)
E_i	Amplitude of the Incident Radiation Field (RAIRS)
$E_\perp$	Amplitude at the Field at the Surface (RAIRS)
E_p^i	Amplitude of Incident p-Polarized Radiation (RAIRS)
E_p^r	Amplitude Reflected p-Polarized Radiation (RAIRS)
I	Infrared Signal Intensity (RAIRS)
M	Transition Dipole Moment (RAIRS)
a'	C_s Symmetry Species (In-Plane)
a''	C_s Symmetry Species (Out-of-Plane)
υ_{asym}	Asymmetric Stretching
υ_{sym}	Symmetric Stretching

V_{bur}	Buried Volume (NHC)
E_{vac}	Vacuum Level

to the friends, to the family, to the love

Acknowledgement

Firstly, I would like to thank my supervisor Prof. Peter McBreen. He is a very knowledgeable professor. Before becoming his student, I had a very shallow understanding of science. Take experiments as an example, I focused on the phenomenon of chemical reactions before, and did not think too much about the logic of chemical reactions. Under his guidance, I learned not only to pay attention to the superficial phenomena in scientific research, but more importantly, to pay attention to the logic and mechanism of reactions itself. In addition, my professor also provided me with financial support.

Secondly, I would like to thank the China Scholarship Council (CSC) for providing me with scholarship support. Without the help of CSC's resources and funds, it would be impossible for me to come to Laval University to study.

Thirdly, I would like to thank my colleagues, Yang Zeng and Yi Dong, they provided me a great help in my daily life and academic aspects in Québec. My colleague, Sonali Khomane, she helped me a lot in scientific experiments. I also would like to thank my roommates and friends in Québec, I cannot live without them in Québec.

Finally, I would like to thank my girlfriend, Yaoting Wen. She was in China and I was in Canada for the past four years, she firmly accompanied me and encouraged me to successfully complete my Ph.D. graduation. I also need to thank my parents, they do not fight against decisions I made, but support my opinions and thoughts.

General Introduction

Molecular Functionalization of Surfaces and 2D Materials

The properties of 2D materials and the surfaces of bulk materials can be tuned by the adsorption of molecules. This thesis describes experiments on the covalent functionalization of Pt(111) and Ru(0001) surfaces, with graphene (Gr), and of 2D-Mo_2C. The functionalization method explored is vapor-phase exposure to a benzimidazolium hydrogen carbonate salt so as to form N-heterocyclic carbene surface ligands (NHCs). In addition, a method to form alkylidene ligands on 2D-Mo_2C was explored.

N-Heterocyclic Carbenes (NHCs) on Metal Surfaces

NHCs are among the most common ligands in homogeneous transition-metal chemistry. They have also found widespread use as surface ligands on metal nanoparticles. More recently, there are many investigations of the formation and properties of NHCs on extended metal surfaces. In this context, **Figure 1**, taken from a review by Glorius et al. [1], reproduces a timeline of the development of the field, with emphasis on recent surface studies of NHCs. The intense study of the surface science of NHCs began following pioneering work by Johnson et al [2]. and by Crudden and co-workers [3]. The general motivation for the early work was to explore if NHCs could perform better than thiols as surface ligands. Results reported by Crudden, Horton et al. [3] showed clearly that NHCs form surface layers on gold that display greater thermal and chemical stability than thiol layers.

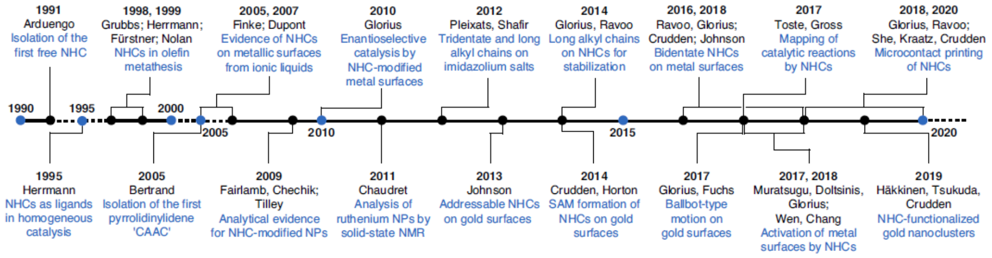

Figure 1 Timeline from the discovery of NHCs to the recent work on their adsorption on solid surfaces. Reproduced with permission from Ref. [1], copyright 2021 Springer Nature Limited.

The remarkable utility of NHCs stems from three notable properties. First, NHCs are called persistent carbenes because they are markedly more stable than other types of carbenes. The stability arises from electronic interactions (**Figure 2a**) between the nitrogen atoms and the carbenic carbon, combining a negative inductive effect (σ-withdrawal) and a positive mesomeric effect (π-donation), resulting in a stabilization of the singlet state [4]. Second, they are σ-donor, nucleophilic, ligands that form strong single bonds to metals [5]. Third, as illustrated in **Figure 2b**, the R wingtip groups provides steric hindrance, again enhancing their stability. Their stability makes NHCs relatively easy to store and handle. NHCs can be used to modify both electronic and steric properties of metal centers. **Figure 2c** shows one of the two NHCs used in this study.

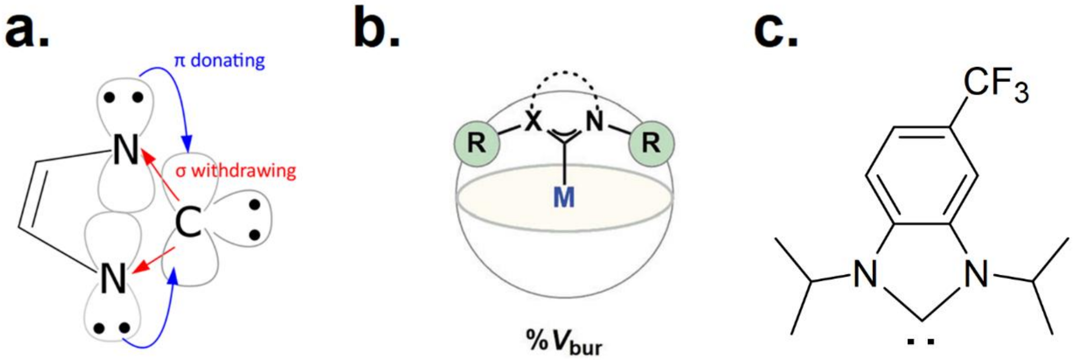

Figure 2 (a) Electronic structure of imidazole-2-ylidenes. σ-withdrawing and π-donating interactions with the heteroatoms contribute to stabilizing the singlet carbene. Reproduced with permission from Ref. [4], copyright 2014 Springer Nature Limited. (b) Steric hindrance due to the wingtip groups (R). The percent buried volume (% V_{bur}) is the percentage of a sphere around the metal atom that is occupied by the rotating R groups. Reproduced with permission from Ref [5], copyright 2017 The Royal Society of Chemistry. (c) Structure of the CF_3-diisopropylbenzimidazolium NHC used in this work.

Figure 3 presents a summary, reproduced from the 2021 review by Glorius et al. of some methods, insights and concepts associated with the formation of NHC ligands on gold surfaces [1]. Surface ligands are formed by exposing the surface to an NHC precursor (**Figure 3a**), typically a CO_2 adduct or a hydrogen carbonate salt. The present project employed hydrogen carbonate salt precursors. The precursor for the NHC shown in **Figure 2c** is 1,3-diisopropyl-6-(trifluoromethyl)-1*H*-benzo[*d*]imidazol-3-ium hydrogen carbonate. The structures formed by NHCs on gold are complex at an atomic level. The different structures shown in **Figure 3b** include a vertical (upright) geometry on an atomically flat surface, a tilted geometry and structures formed to gold adatoms. One of the latter structures is a dimer in which the gold adatom separates the two NHCs, both of which are lying down on the surface.

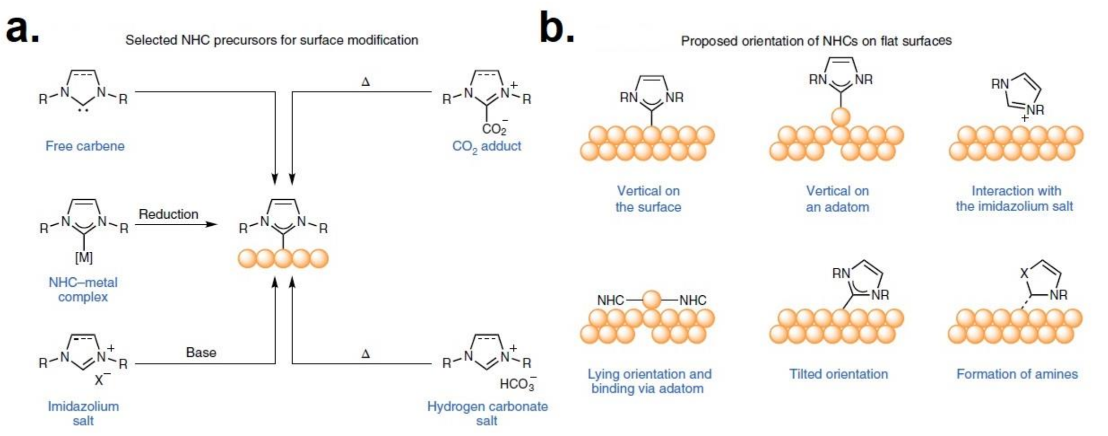

Figure 3 Summary of (a) methods for forming NHCs on gold surfaces and (b) various adsorption geometries that may be formed. Reproduced with permission from Ref. [1], copyright 2021 Springer Nature Limited.

The first study of NHCs on a gold surface was reported by Siemeling and co-workers in 2011 [6]. Based on near edge X-ray absorption fine structure (NEXAFS) measurements, they determined that the NHC ligands were tilted by 30° ± 6° to the surface normal. Johnson and co-workers reported the first detailed experimental and theoretical study of the formation of NHC layers on Au surfaces in 2013 [2]. They found the length of the N,N-dialkyl NHC-Au bond to be 1.98 Å, significantly shorter than a thiol-Au bond. The calculated NHC-Au bond dissociation energy was 67 kcal/mol, which is much higher than the value for a typical S-Au bond (45 kcal/mol) [7]. They measured the amount of deposited NHC and demonstrated polymer growth from Grubbs catalyst initiators bound to the addressable NHC. In 2014, Crudden and co-workers proved that NHC-Au(111) ligands display greater heat resistance and chemical resistance than thiol-based self-assembled monolayers (SAMs) on Au(111) [3]. In a pioneering set of experiments, they demonstrated that NHC-Au(111) ligands are stable under boiling tetrahydrofuran (THF), boiling water and even in a 1 % H_2O_2 environment [3]. It was an important landmark for NHCs to emerge as alternatives to thiol-based SAMs (self-assembled monolayers) on gold surfaces. Before this discovery the formation of SAMs of thiolate ligands was the dominant method to functionalize metal surfaces [8–12].

Much more work is required to define the properties of NHC layers on metal surfaces. An example of the complexity of the interaction with gold surfaces is given by an important study by Fuchs' group [13]. They found that the strong NHC-Au bond energy enables the movement of NHC-Au, $Au(NHC)_2$, even $Au(NHC)_3$ adatom complexes on Au(111). That is, NHC molecules pull out a gold atom from the surface, or capture a diffusing gold atom to form adatom complexes which move together on the Au(111) surface. The authors called this phenomenon ballbot-type motion. The structures formed by NHCs on gold depend on the N,N-substituents. Fuchs *et al.* found that 1,3-dibutylimidazol-2-ylidene formed a flat-lying NHC-Au-NHC structure attributed to effect of van der Waals interactions of the long chain alkyls with the surface [14]. In contrast, steric hindrance effects of bulky isopropyl N-substituents, caused 1,2-di-isopropylimidazol-2-ylidene to form a vertical adatom-NHC structure. Crudden *et al.* studied NHCs formed on Cu(111) and Au(111) by exposure to benzimidazolium hydrogen carbonates bearing methyl, ethyl or isopropyl wingtip groups [15]. They found that ethyl and methyl substituted NHCs formed flat-lying NHC-adatom-NHC structures on both surfaces. The di-isopropyl substituted NHC formed a vertical (upright) structure on both surfaces. The latter NHC desorbed cleanly from Cu(111) at approximately 570 K. In contrast, the flat-lying structures (methyl and ethyl substituents) underwent, in competition, both decomposition and desorption.

There are few articles reported for NHC adsorption on surfaces other than Au, Cu and Ag (the coinage metals). Gross and co-workers used infrared nano-spectroscopy based on synchrotron radiation to detect oxidation and reduction processes of functional groups on the wingtips of NHCs on supported Pt nanoparticles (NPs) [16,17]. They found that low coordination metal sites (such as edges sites of Pt NPs) are more active than high coordination sites (such as center sites)[16]. In a preliminary part of the present study, our group published an reflectance absorbance infrared spectroscopy (RAIRS) study of the interaction of 1,2-di-isopropylbenzimidazolium hydrogen carbonate with Pt(111). The precursor converted into an upright NHC on the surface. The isopropyl groups were found to undergo bond breaking at ~435 K but the NHC skeleton remained stable until ~515 K [18].

Graphene on Pt(111) and Ru(0001)

Graphene (Gr) can be created by chemical vapor deposition (CVD) on the surface of transition metal substrates. In this method, the hot metal is exposed to a hydrocarbon such as methane or ethylene. The clean metal catalyzes dehydrogenation of the carbon source. The resulting adsorbed hydrogen atoms combine and desorb as H_2 leaving carbon on the surface. Surface diffusion of carbon results in the nucleation and growth of supported graphene. **Figure 4** shows a proposed sequence of steps in the growth of Gr/Pt(111) from exposure to ethylene [19].

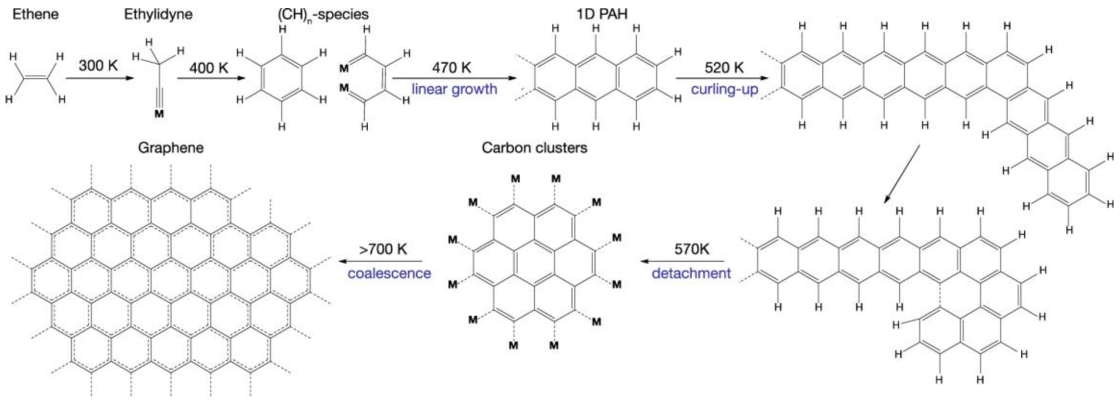

Figure 4 Schematic illustration of the transformation of adsorbed ethylene on Pt(111) to graphene. Reproduced with permission from Ref. [19], copyright 2017 American Chemical Society.

Of great significance for our studies, the properties of the graphene layer depend on the substrate. Gr/metal systems are often divided into two general categories (**Figure 5a**) in relation to the strength of the graphene-metal interaction [20]. Ru [21,22], Ni [23], Re [24], Co [25], Rh [26], Pd [27] surfaces display a strong interaction with Gr, while Pt [28], Ir [29], Cu [30], Ag [31] surfaces display a weak interaction. Thus, by studying Gr/Pt(111) and Gr/Ru(0001) we investigate two very different systems. The strength of interaction between graphene and the metal substrate correlates with the electronic structure of the metal (**Figure 5a**), as expressed by the energy difference between the Fermi level of the metal and the center of the d-band (the average energy of d-states) [32].

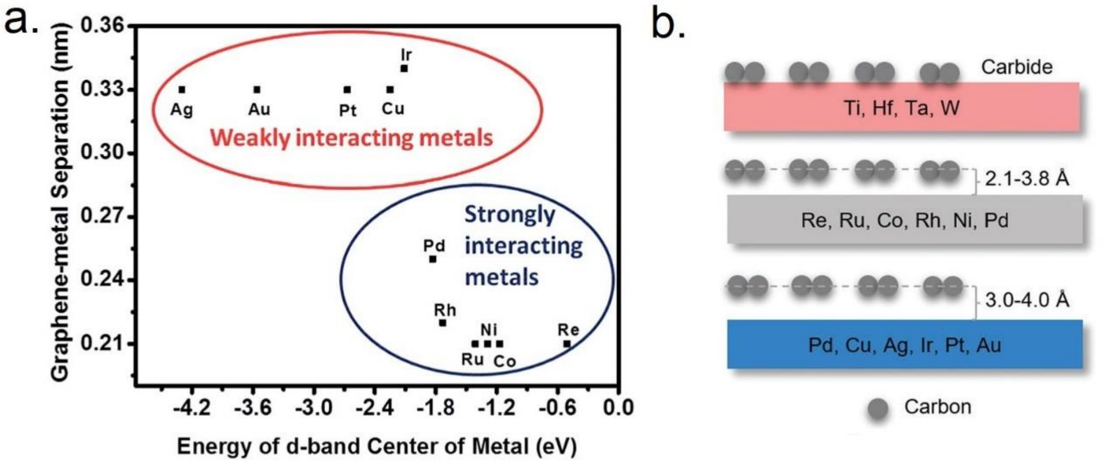

Figure 5 (a) The C-metal distance and strength of interaction as a function of the average energy of the valence band d-states of the metal. Reproduced with permission from Ref. [32], copyright 2014 The Royal Society of Chemistry. (b) Categories of graphene-metal interactions classified in terms of the C-metal distance. Reproduced with permission from Ref. [33], copyright 2017 The Royal Society of Chemistry.

The lattice constants of graphene and the Pt(111) and Ru(0001) surfaces are 2.46, 2.77 and 2.71 Å, respectively. The ~9% lattice mismatch between graphene and the Ru(0001) surface results in a Moiré pattern with a periodicity of 2.95 nm [34]. As shown in **Figure 6**, the Moiré superstructure is formed by 25 x 25 graphene hexagons on 25 x 25 unit cells of the metal surface. It can be seen from **Figure 6a** that the position of carbon relative to atoms in the first (A-layer) and second (B-layer) varies continuously across the superstructure. As a result, the chemical interaction and the C-Ru distance also varies, forming hill and valley (flat) regions (**Figure 6b**).

An atomistic description of different regions of the superstructure is given in **Figure 6c** in terms of a top-view of four different adsorption sites for graphene hexagons [33]. Considering a given side of the hexagon, the site indicated in blue places one carbon atom over a Ru atom in the second layer and one over the third layer where there is no Ru atom. None of the carbon atoms in the hexagon are over the Ru atom in the first (surface) layer. This adsorption site is called the *atop* site. The site indicated in green places one carbon atom over a first layer Ru atom and the second over the third layer where there is no Ru atom. This is called the *fcc* site. The site indicated in purple places one carbon atom over a first layer Ru atom and the second over a second layer Ru atom. This is called the *hcp* site. The fourth site, indicated in black, is called the *bridge* site. These sites are illustrated in **Figure 6d** using a side-view and indicating the approximate corresponding Ru-C distances [35]. The specific distances are 2.2 and 3.7 Å. It can be seen that the *atop* sites give rise to the hill regions. Returning to **Figure 6a**, the red, green and blue circles show, respectively, *atop*, *fcc* and *hcp* regions of the Moiré superstructure [36].

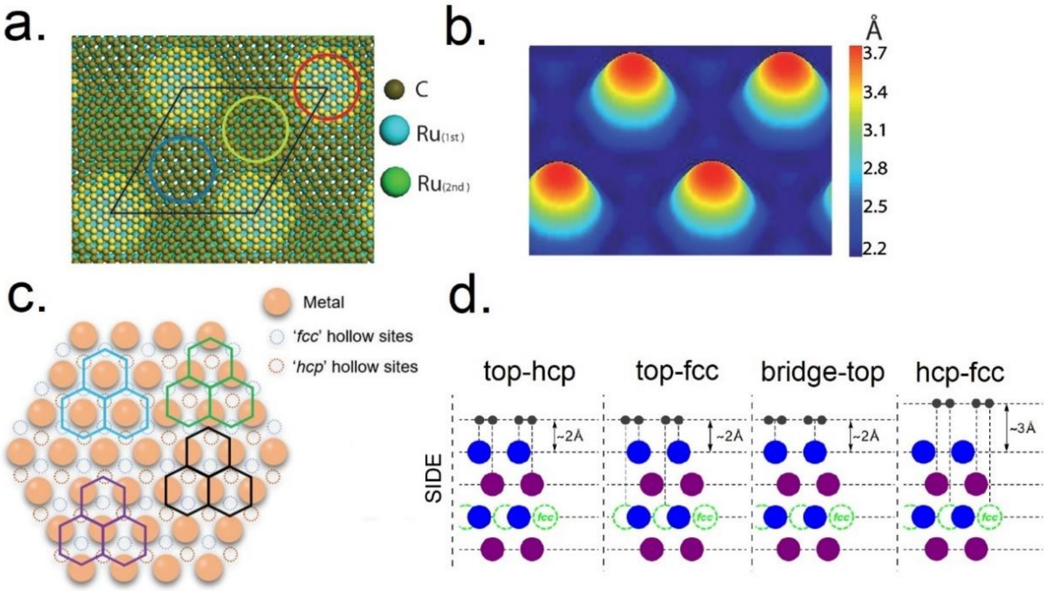

Figure 6 DFT-optimized model (a) of the Moiré superstructure formed by graphene on Ru(0001) and (b) map of carbon height within the structure. Reproduced by permission from Ref. [36], copyright 2010 IOP

Publishing Ltd and Deutsche Physikalische Gesellschaft. (c) Well-defined adsorption sites for graphene hexagons on Ru(0001). Reproduced with permission from Ref. [33], copyright 2017 The Royal Society of Chemistry. (d) Side-view of the four adsorption sites shown in (c). Reproduced with permission from Ref. [35], copyright 2020 American Physical Society.

Graphene forms a single carpet-like domain on Ru(0001) surfaces [37]. The periodic variation of the Ru-C interaction is clearly seen in STM (scanning tunneling microscopy) images. For example, the dashed triangle in **Figure 7b** indicates a region presenting graphene on *fcc* sites while the very bright protrusions arise from graphene at *atop* sites [37].

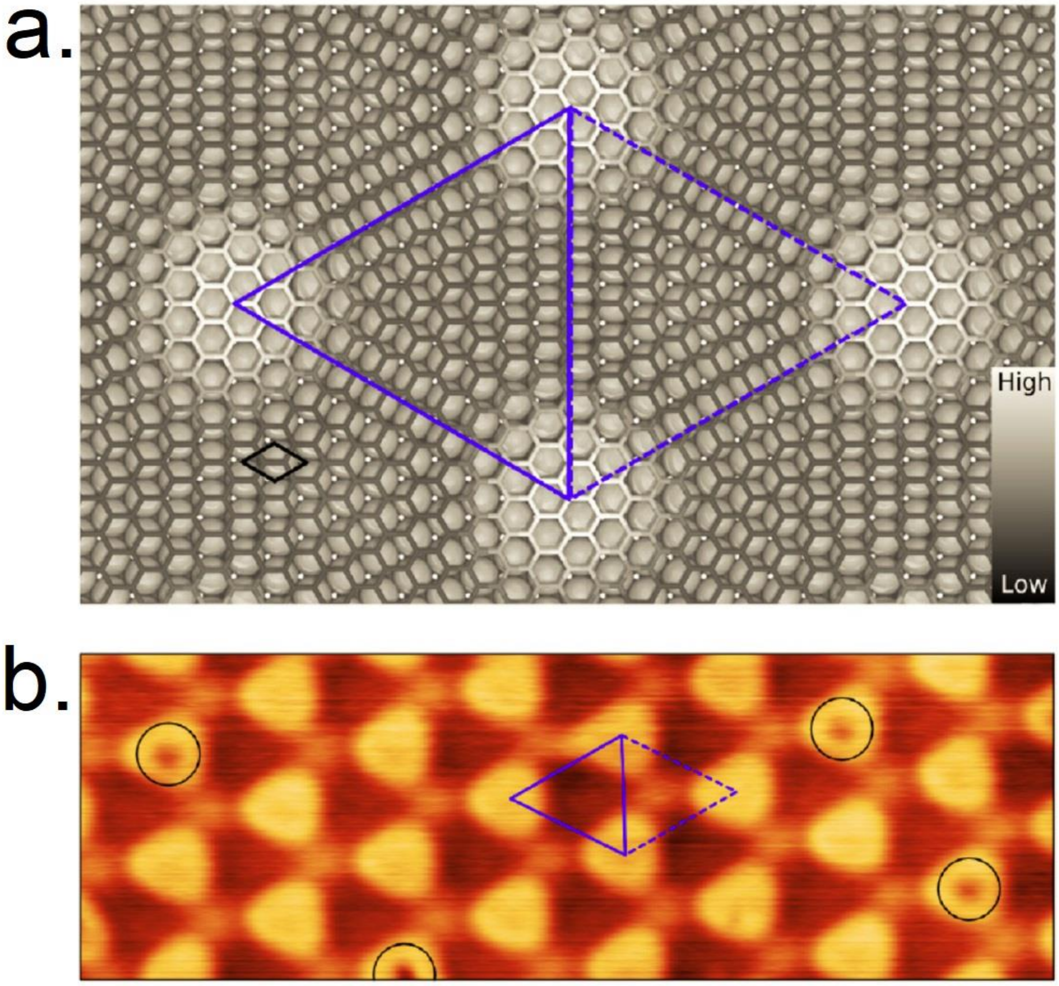

Figure 7 (a) (25 x 25)C/(23 x 23)Ru Moiré superstructure. (b) STM image showing the periodicity of the superstructure. Reproduced with permission from Ref [37], copyright 2015 American Chemical Society.

As summarized in **Figure 8a-c**, model calculations show that electron redistribution from the metal to graphene occurs in the *fcc* and *hcp* regions of the superstructure, where C-Ru bonds are formed and graphene is close to the surface. Graphene on Ru(0001) is n-doped [38]. Furthermore, as shown in **Figure 8d**, the strong chemical interaction with the surface in the *fcc* and *hcp* regions leads to a significant lengthening of the C-C bonds [39]. Thus, the sp^2 network and corresponding electronic structure of graphene is significantly perturbed on Ru(0001).

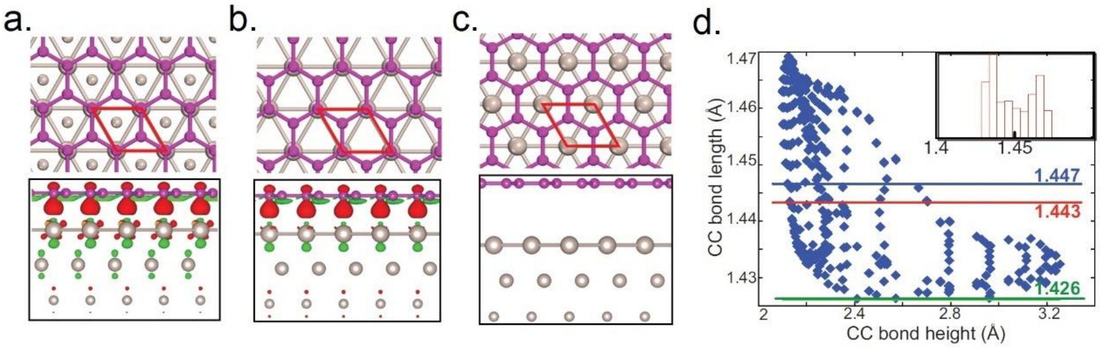

Figure 8 Model structures of (a) *hcp*, (b) *fcc* and (c) *atop* configurations of graphene on Ru(0001) and, underneath, their corresponding side views of charge density. Reproduced with permission form Ref [38], copyright 2019 The Royal Society of Chemistry. (d) DFT-calculated CC bond lengths as a function of their height in the Moiré superstructure. Reproduced with permission from Ref. [39], copyright 2013 American Physical Society.

Graphene can be decoupled from Ru(0001) through intercalation of atomic oxygen, formed through the dissociative adsorption of O_2, between graphene and the metal [40]. The process is illustrated in **Figure 9**. The decoupled layer is strongly p-doped with the Fermi energy (referenced to E_{vac}) rising to ~800 meV higher than the Dirac point as the oxygen surface coverage is increased [40]. Thus, oxygen intercalation transforms graphene on Ru(0001) from an n-doped to a p-doped material.

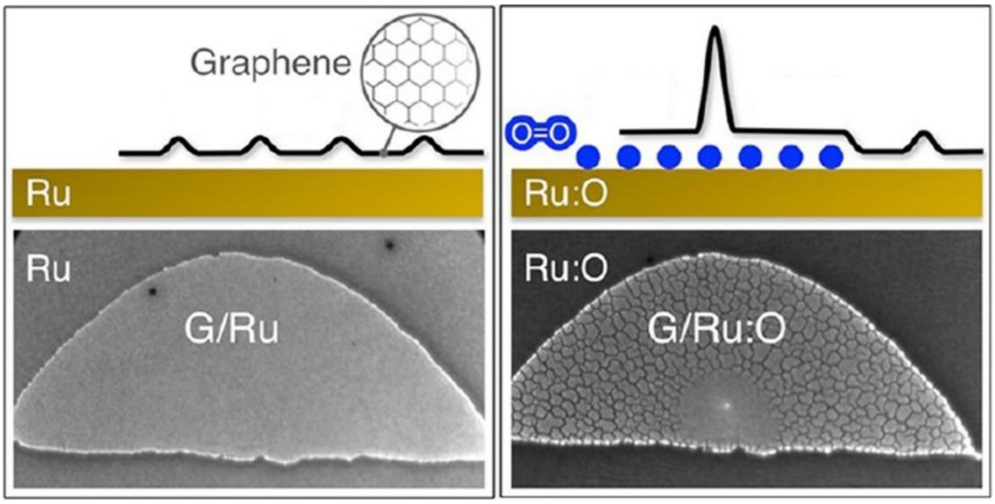

Figure 9 Top panels: Schematic illustration of oxygen intercalation between graphene and Ru(0001). Bottom panels: LEEM (low-energy electron microscopy) data for oxygen intercalation under a graphene island on Ru(0001). The features in the Gr/O/Ru(0001) layer are wrinkles. Reproduced with permission from Ref. [40], copyright 2013 American Chemical Society.

Figure 10 shows a simplified diagram of the band structure of pristine, n-doped and p-doped graphene. In pristine graphene, the π-orbital derived valence band is full and the π*-orbital derived conduction band is empty. The Fermi level (E_F) is thus the highest energy in the valence band. Its value is defined with respect to the energy of an electron (E_{vac}) just outside the material. The Dirac point is the energy at which the spherical cones describing the density of states (DOS) of the valence and conduction bands meet. Hence, for pristine graphene, the Dirac point is at the Fermi level.

Graphene forms a quasi-freestanding layer (**Figure 5b**) on Pt(111) where the interaction with the surface is through van der Waals forces. As a result, it displays the Dirac cone band structure characteristic of pristine graphene. However, equilibration of the Fermi levels of graphene and Pt leads to electron transfer from graphene to the metal. Because the DOS close to the Dirac point is very low, electron transfer causes a strong shift in the Fermi level making graphene on Pt(111) strongly p-doped.

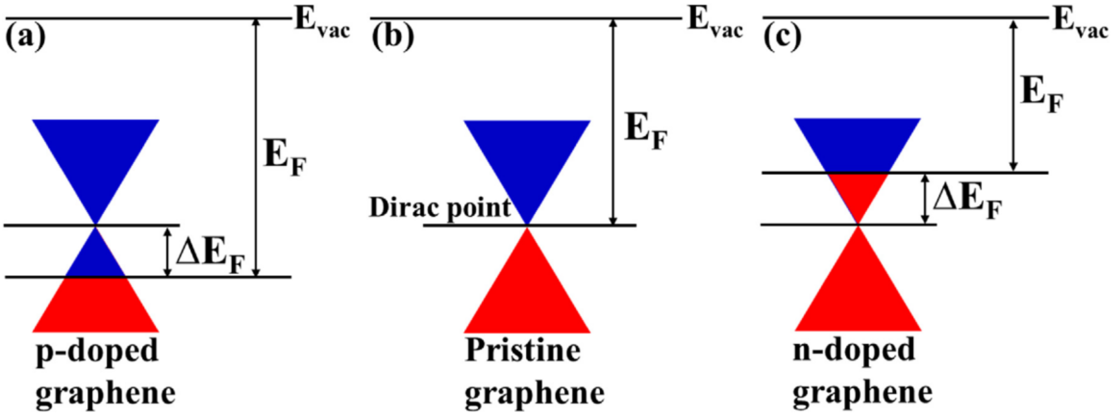

Figure 10 Simplified illustration of the valence band structure of pristine graphene and of electron transfer to (p-doping) or from (n-doping) a substrate. Reproduced with permission from Ref. [41], copyright 2017 Elsevier B.V. The band structure is drawn to indicate spherical cones that meet at the Dirac point. The filled density of states (red) and unoccupied density of states (blue) are separated at the Fermi level (E_F). The Fermi energy is given relative to the vacuum level (E_{vac}). The electronic structure of graphene on Pt(111) retains its Dirac cone structure as it is a quasi-freestanding layer. However, it is p-doped through equilibration with the metal. Graphene on Ru(0001) loses its Dirac cone structure because of strong C-Ru rehybridization. The chemical bonding interaction causes the layer to be n-doped. Oxygen intercalation to form Gr/O/Ru(0001) decouples the layer, restoring its Dirac cone electronic structure and making it p-doped.

Wrinkle formation is an important phenomenon in graphene systems [42]. As shown in **Figure 11**, wrinkle formation occurs on cooling down following the CVD growth of graphene on Pt(111) at high temperatures, as a result of the different thermal expansion coefficients of graphene and Pt. Note, from **Figure 9,** that wrinkle formation also occurs following oxygen intercalation between graphene and Ru(0001) [42]. In contrast to graphene on Ru(0001), the overall graphene monolayer on Pt(111) is formed from different rotational domains.

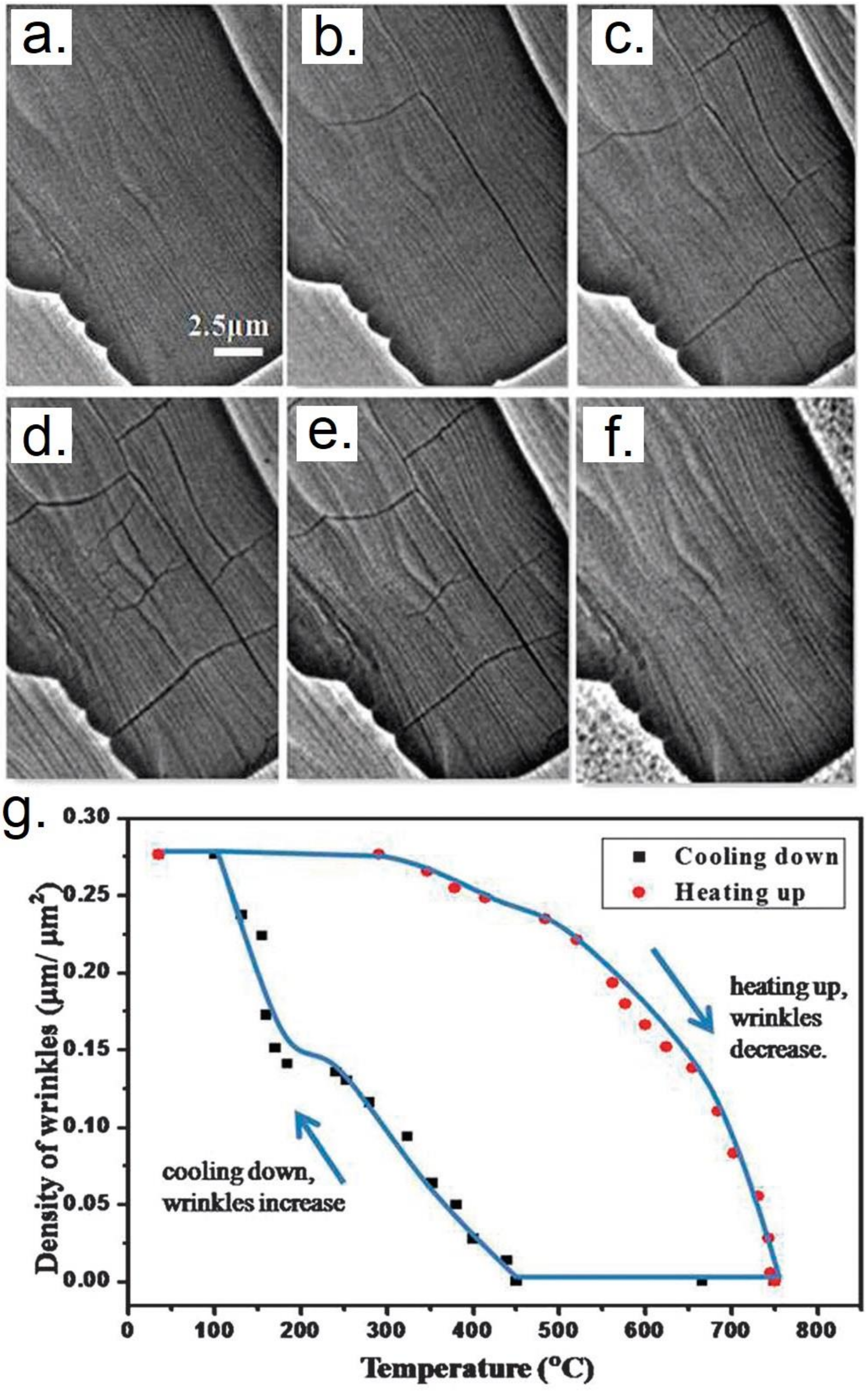

Figure 11 (a-f) LEEM data showing wrinkle formation as Gr/Pt(111) cooling down following CVD deposition, then heating up at different temperatures. (a) 665.8 °C; (b) 345.0 °C; (c) 130.8 °C; (d) 36.5 °C; (e) 601.9 °C; (f) 747.6 °C. (g) Density of wrinkles at different heating and cooling temperatures. Reproduced with permission from Ref. [42], copyright the Owner Societies 2013.

The literature experimental data shown in **Figure 9** and **Figure 11** were acquired using the low-energy electron microscopy (LEEM) technique [40,42]. LEEM is a powerful technique to image graphene growth, oxidation, etching and wrinkle formation [40,42–44]. The technique uses the reflection of low energy electrons (1-100 eV) to produce images of surface layers. The contrast in the images is sensitive to valence electron structure and hence to the chemical composition of the surface [45]. In our studies, we consulted LEEM data from the literature as a guide to define graphene layer growth on Pt(111) and Ru(0001)

Covalent Modification of Graphene

Chemical modification of graphene by grafting organic groups may be used to modify its intrinsic properties or to introduce new functions for applications in many areas, such as in electronics, photocatalysis [46], sensing [47] and gas storage [48]. Non-covalent functionalization has the advantage of not damaging the sp^2 hybridization of Gr but it normally provides low thermal stability especially when small molecules are used [49–55]. Covalent modification is more robust but it also more challenging because graphene is a relatively inert material [56,57]. Hence, several reactions involving highly reactive species, such as the aryne [58], nitrene [59], Diels-Alder [60], carbene [61] and diazonium [62,63] methods, were developed to modify graphene. Among these approaches, the diazonium method (**Figure 12**) is the most efficient and commonly used. The method forms an aryl radical either through electrochemical activation (electron transfer to the electrophile diazonium salt) or through spontaneous electron transfer from graphene. Electrochemical activation is used in order to functionalize the basal plane of graphene (**Figure 13**). Spontaneous activation may be sufficient to functionalize the more reactive edge sites of graphene.

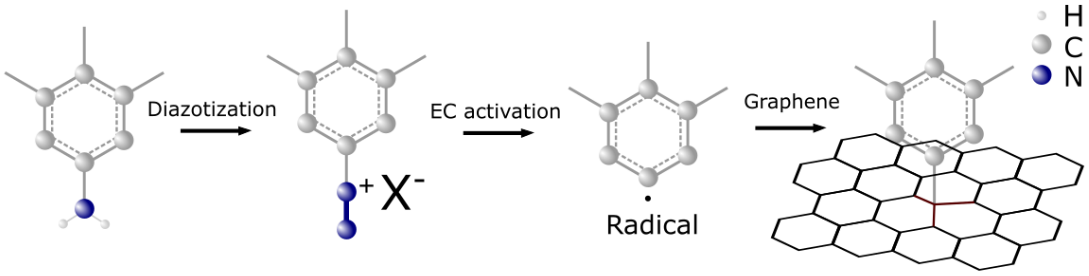

Figure 12 Method using diazonium salts to create covalent aryl-C bonds with graphene. Diazonium salts, where X$^-$ is the counterion, are generated from anilines and electrochemical activation (EC) is normally used to generate the aryl radical [63].

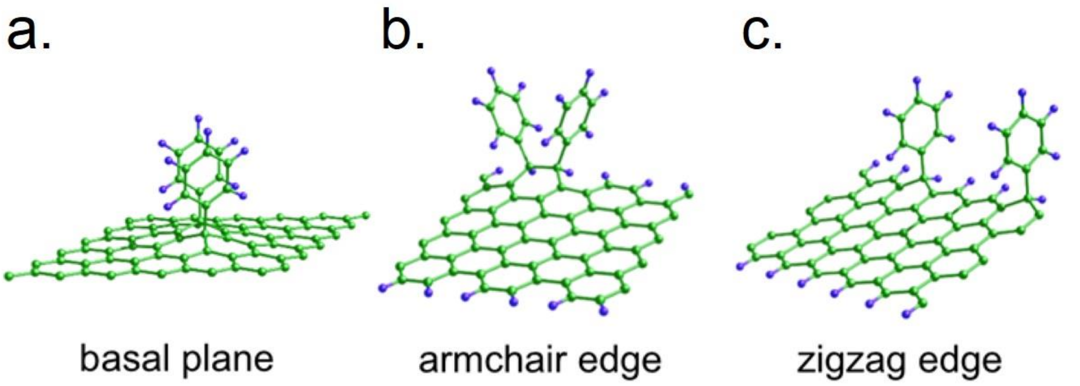

Figure 13. Calculated structures of aryl groups on the (a) basal plane and at (b-c) edge sites of graphene. Reproduced with permission from Ref. [64], copyright 2016 American Chemical Society.

There is continued research into methods to graft organic groups to graphene because the conventional diazonium method has some drawbacks. For example, diazonium salts are generally unstable under ambient conditions and the grafting process may be accompanied by unwanted side-reactions either in solution or with the grafted groups. In this thesis, I describe an investigation of the functionalization of graphene using an NHC. To the best of my knowledge, there is only one publication in the literature on the functionalization of graphene using the NHC approach. Yoon *et al.* used a pyrenyl-substituted diisopropylbenzimidazium NHC [65] (the same structure as the NHC shown in **Figure 2c** but with a pyrene substituent in the place of the CF_3 substituent that we use). They concluded that covalent modification occurs at edge sites and that, surprisingly, the interaction involves a π-backdonation component in addition to the electron-donation associated with NHC bonding.

In this work, RAIRS is used to detect the adsorbed NHC on graphene using CF_3 as a reporter group. The CF_3 substituent is characterized by three intense vibrational bands, making it easy to detect the presence of surface NHC. Furthermore, an analysis of the relative intensities of the three bands enables a determination of the adsorption geometry of the NHC.

Two-Dimensional Transition Metal Carbides

The last Chapter of the thesis describes exploratory measurements on the reactivity and functionalization of 2D-Mo_2C/Cu samples. These samples are composed of ultrathin molybdenum carbide crystallites on a planar copper support. Their study is related to the current intense research activity on MXenes [66].

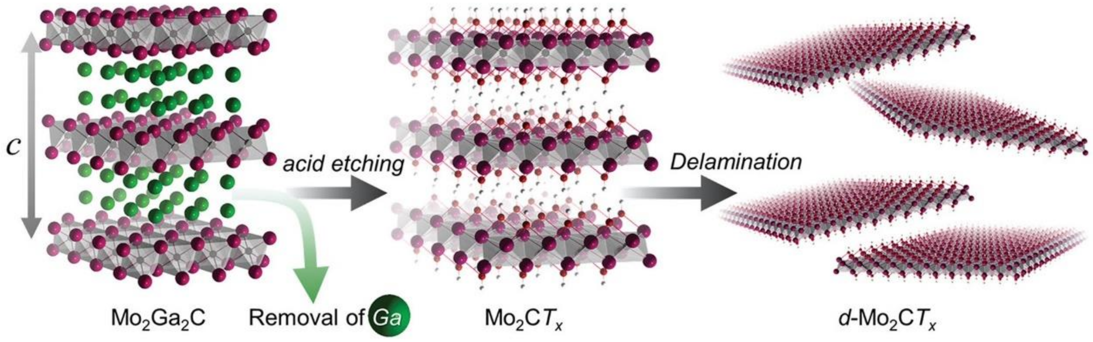

Figure 14 Acid etching of a layered parent Mo_2Ga_2C phase to produce 2D-Mo_2C-T_x flakes. Reproduced with permission from Ref. [67], copyright 2016 WILEY-VCH Verlag GmbH & Co. KGaA, Weinheim.

MXenes are produced by etching the A element (typically Al, Ga or Si) out of layered MAX materials where M is an early transition metal and X is carbon or nitrogen. **Figure 14** illustrates the synthesis of 2D-Mo_2C-T_x flakes from a Mo_2Ga_2C parent phase [67]. The etching process results in a mixture of surface termination groups (T_x), typically O, OH and F. Since the MXenes are only a few atoms thick the surface terminations have a major impact on their properties. Since their discovery in 2011, MXenes been shown to display remarkably strong performances in many applications ranging from catalysis to electromagnetic shielding. Their broad utility derives from a blend of properties including 2D (flake) topology, metallic conductivity, ceramic-like mechanical properties, and a chemical composition which gives them both catalytic activity and hydrophilicity [66].

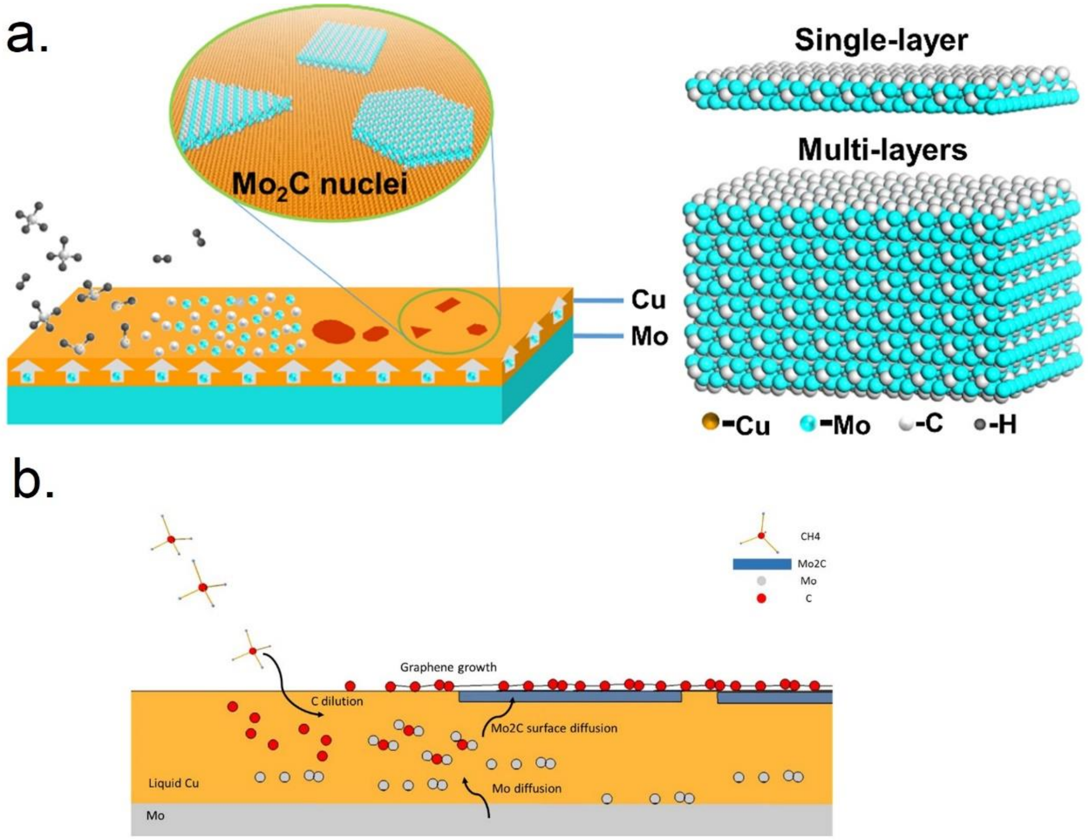

Figure 15 (a) CVD growth of 2D-Mo_2C crystallites at the surface of molten copper. These 2D-materials can be considered as bare MXenes since they do not have T_x groups resulting from an acid etching step. Reproduced with permission from Ref [68], copyright 2019 Elsevier Ltd. (b) A proposed mechanism molybdenum carbide growth at the surface of copper. This illustration also shows the formation of a graphene layer on the crystallites. Reproduced with permission from Ref [69], copyright 2019 IOP Publishing Ltd.

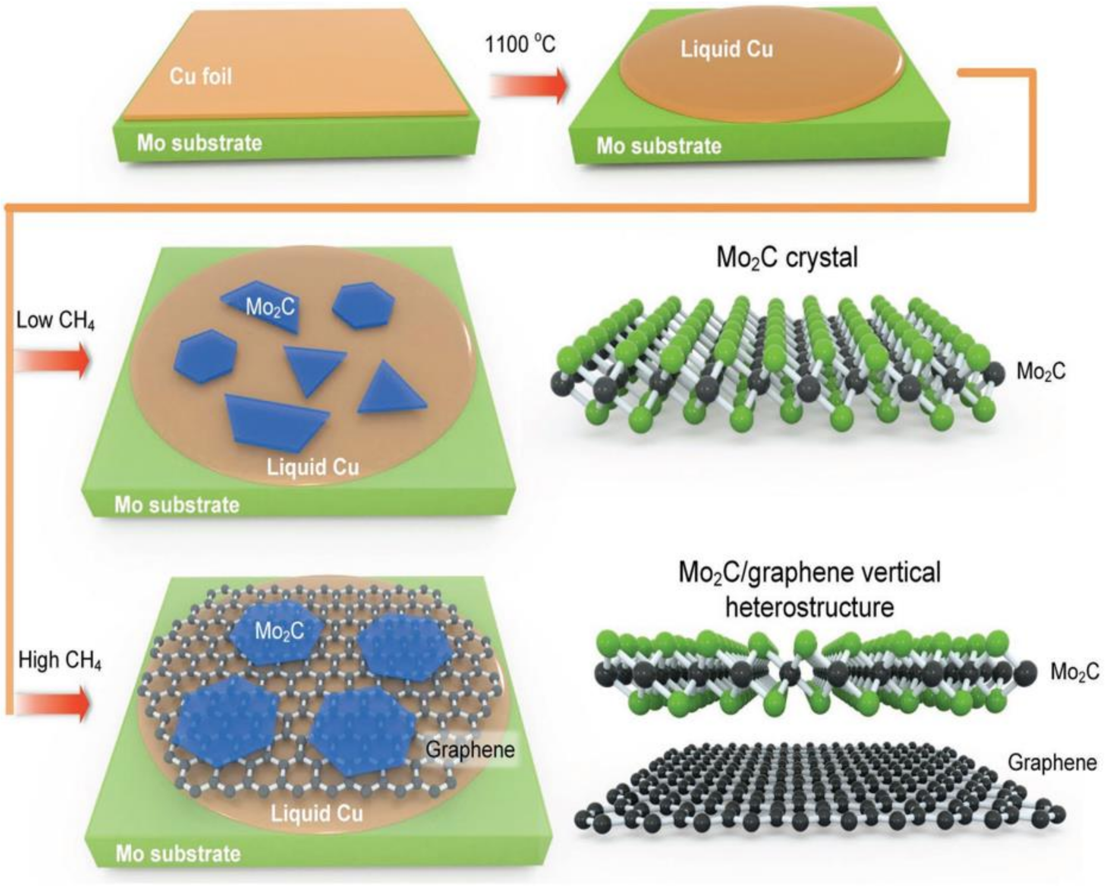

Figure 16 Illustration of the growth of 2D-Mo_2C and of a vertical 2D-Mo_2C/graphene/Cu heterostructure. Reproduced with permission from Ref [70], copyright 2017 WILEY-VCH Verlag GmbH & Co. KGaA, Weinheim.

Our 2D molybdenum carbide samples were prepared by the group of Professor Ren (Shenyang National Laboratory for Material Science, Institute of Metal Research, Chinese Academy of Sciences) using a chemical vapour deposition (CVD) method. This alternative synthesis method, first published by Ren *et al*. in 2015, relies on the diffusion of Mo atoms through molten copper where interaction with methane leads to the formation of 2D crystalites on the copper surface [71]. **Figure 15** and **Figure 16** show general aspects of the CVD method. The 2D-carbides prepared by this method form extremely high-quality regular shaped crystallites as shown by scanning tunneling microscopy, atomic force microscopy, optical microscopy and transmission electron microscopy characterization. The thickness and the shape of the crystallites depend on the preparation conditions. Furthermore, vertical 2D-Mo_2C/Gr heterostructures can be formed. There are conflicting reports in the literature as to whether the graphene layer is under or over the 2D-Mo_2C. Indeed, Turker and co-workers found a Gr/2D-Mo_2C/Gr sandwich structure when 2D-Mo_2C was synthesized by the CVD method on Cu (**Figure 17**) [72].

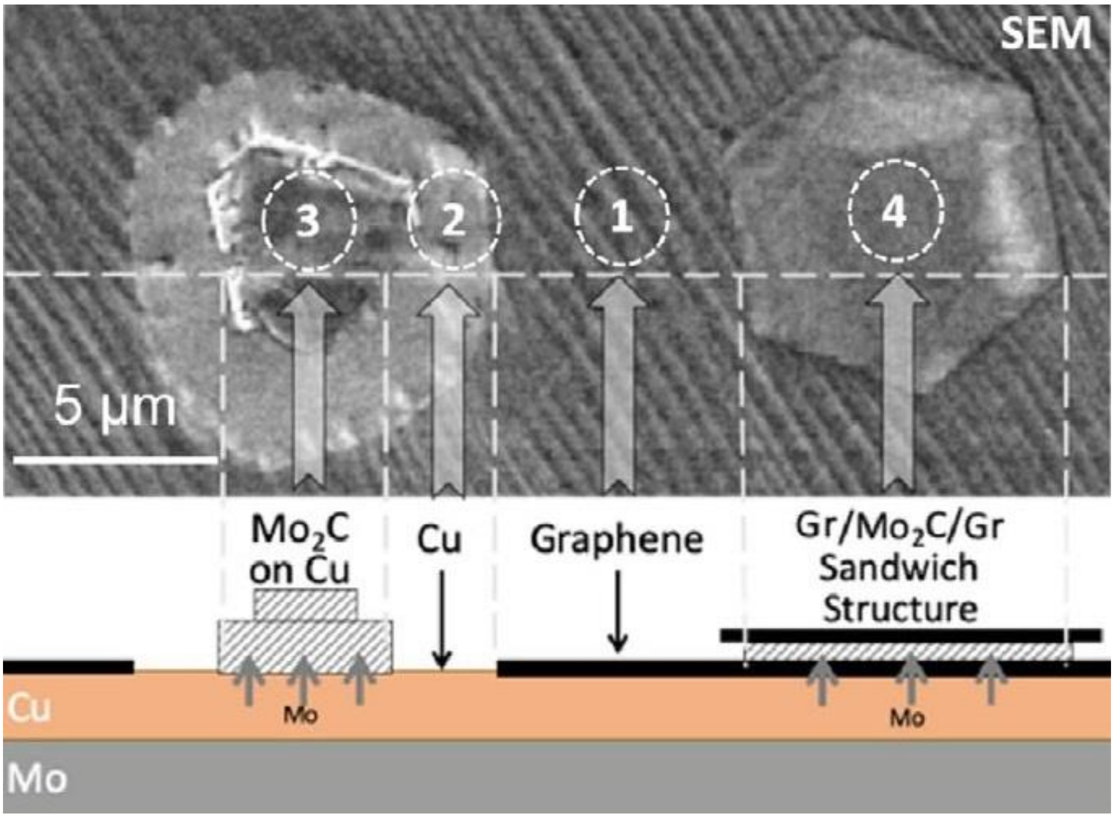

Figure 17 SEM image of Mo_2C growth on Cu layer by the CVD method. The numbers correspond to the different regions on SEM image, where number 4 represents the Gr/Mo_2C/Gr Sandwich structure. Reproduced with permission from Ref [72], copyright 2020 The American Ceramic Society.

It may be seen from **Figure 17** that the characterization of the structure and composition of CVD-grown Mo_2C on molten copper is an exceedingly difficult challenge. In Chapter 4, we report a preliminary exploration of methods to functionalize such samples without providing a detailed description of the structure and composition.

Chapter 1 Experimental Techniques

1.1 Ultra-High Vacuum (UHV) Chamber

All the experiments described in this thesis were carried out under ultra-high vacuum (UHV) conditions. The base chamber pressure of 5 × 10^{-10} Torr was achieved using a turbomolecular pump (Pfeiffer tc600) backed by a mechanical (rotary) pump. UHV conditions were necessary to ensure that the results were not modified by contamination effects and also to permit measurements by X-ray photoelectron spectroscopy (XPS). Reflection Absorption Infra-Red Spectroscopy (RAIRS) and XPS measurements were used to characterize the surfaces under study.

1.2 X-Ray Photoelectron Spectroscopy (XPS)

The XPS spectrometer used in these studies was a PHOIBOS 100 hemispherical energy analyzer equipped with a 5-channel MCD detector (SPECS GmbH). XPS is used to analyze the chemical composition of surfaces. There are three main units in a photoelectron spectrometer: an X-ray source; an analyzer for measuring the kinetic energy of the photoelectrons; a detector coupled to an acquisition system. As shown in **Figure 18**, a hot filament in the X-ray source emits electrons by thermionic emission. The electrons are accelerated by high voltage to bombard either an Al or a Mg anode, causing the emission of Al K_α ($h\upsilon$ = 1486.6 eV) or Mg K_α ($h\upsilon$ = 1253.6 eV) X-rays. The X-ray radiation is used to eject core level electrons. The kinetic energy ($\mathrm{E_k}$) of the photoelectrons is given by the energy conservation equation (subject to a correction for the spectrometer work function), where $\mathrm{E_b}$ is the binding energy, relative to the Fermi level, of the electron in the element. (**Equation 1**):

$$\mathrm{E_k} = h\upsilon - \mathrm{E_b} \quad \textit{\textbf{Equation 1}}$$

The technique is sensitive to the chemical environment of probed element. Chemical bonding and valence state information can be obtained by measuring shifts in $\mathrm{E_b}$.

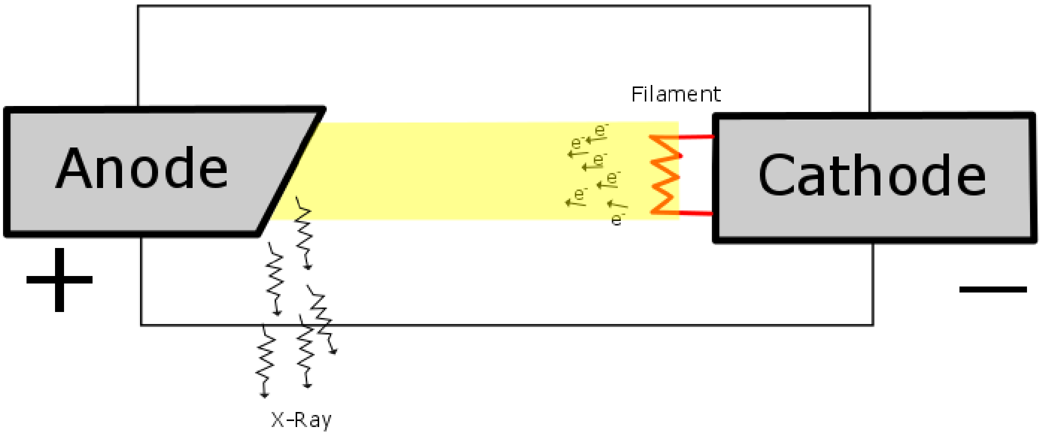

Figure 18 Electron bombardment induced emission of X-rays from Al or Mg anodes.

XPS is a surface sensitive technique. Although the X-ray radiation penetrates deeply into the sample, the detected kinetic energy $\mathrm{E_k}$ (**Equation 1**) only come from close to the surface. Consider photoionisation at, for example, 2 nm below the surface and subsequent travel of the photoelectron to the surface prior to ejection, energy analysis and detection. During the travel in the solid the photoelectron may undergo inelastic interactions (collisions) leading to a decrease in kinetic energy. Only photoelectrons that have not lost energy contribute to the intensity of a peak in the XPS spectrum. That is, an XPS peak at $\mathrm{E_k} = h\upsilon - \mathrm{E_b}$ is produced by photoelectrons that have undergone no energy loss. As the distance a photoelectron moves through a solid material increases the probability of multiple (n) energy loss collisions increases, each collision reducing the kinetic energy by $\Delta\mathrm{E}$. If detected, the latter photoelectrons, called secondary electrons, produce a broad inelastic scattering tail over the range $\mathrm{E_k} - \mathrm{n}(\Delta\mathrm{E})$, as illustrated in **Figure 19**. Since the tail resulting from inelastic collisions is at lower kinetic energies than the photoelectron peak, a rising background appears to the high binding energy side of photoelectron peaks.

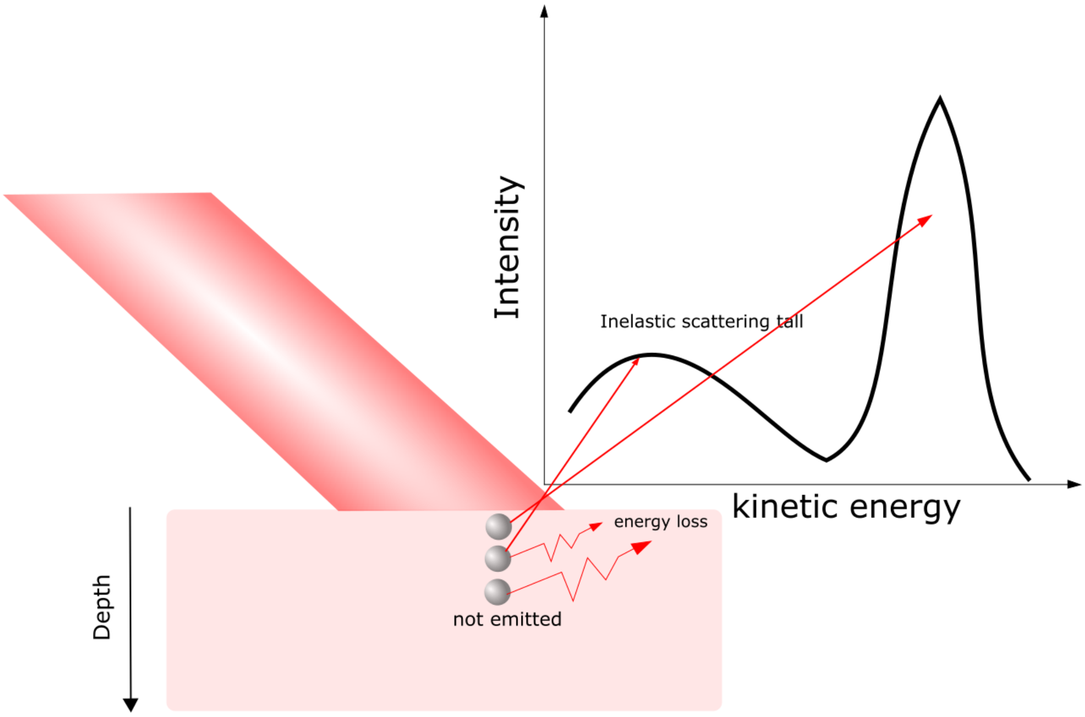

Figure 19 Schematic illustration of the origin of an inelastic scattering tail to the low kinetic energy side of a photoelectron peak. Photoelectrons emitted from the surface without energy loss generate the photoemission peak. Photoelectrons emitted from the surface following inelastic collisions generate the secondary electron scattering tail.

As shown in **Figure 20**, the mean free path determines the depth to which the solid sample is analyzed. The inelastic mean free path (λ) may be defined as the average distance that electrons of a given kinetic energy travel between successive inelastic collisions [73]. The attenuation of the measured signal intensity (I_d) at E_k as a function of the distance (d) that the photoelectrons travel between photoionization (I_0) and escape from the solid is given by **Equation 2** [74]:

$$I_d = I_0 e^{-d/\lambda} \quad \textbf{Equation 2}$$

From **Equation 2**, λ is defined as the distance over which the signal decays to $1/e$ of I_0.

When measurements are made with the electron analyzer placed normal to the surface (position A, **Figure 20a**), ~95 % of the electrons giving rise to a peak in the photoelectron spectrum originate from a depth that is less than 3λ from the surface. The equivalent depth of analysis can be reduced to $3\lambda\cos\theta$ by making measurements with the analyzer lens at an angle θ with respect to the surface normal (position

B). The value of λ depends on the kinetic energy of the photoelectron, as approximately described by the universal curve (**Figure 20b**).

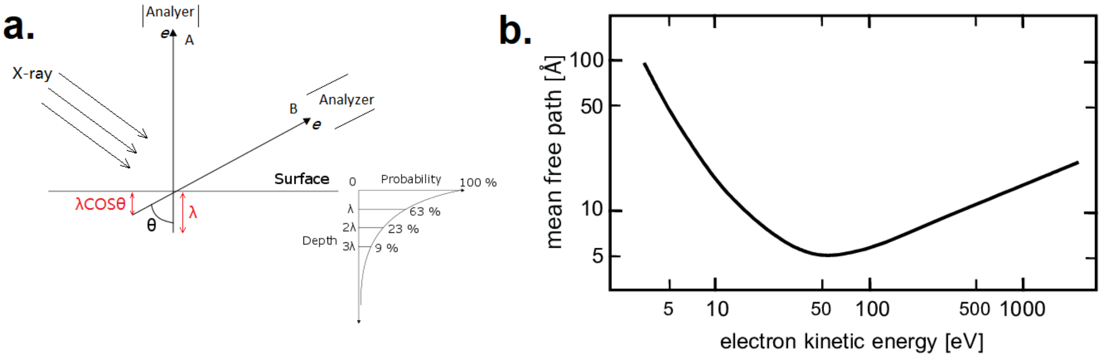

Figure 20 XPS analysis depth. (a) The take-off angle (θ) describes the orientation of the analyzer lens relative to the surface. In measurements with the analyzer orthogonal to the surface (position A), 63 % of the signal in a peak in the spectrum comes from a depth less than λ from the surface. For a measurement at position B, 63 % of the signal in a peak in the spectrum comes from a depth less than $\lambda\cos\theta$ from the surface. (b) The universal curve used to estimate the value of λ as a function of the kinetic energy of the photoelectron [74].

1.3 Reflection Absorption Infra-Red Spectroscopy (RAIRS)

RAIRS is a widely used vibrational spectroscopy method to study molecular absorption on flat metal surfaces. Measurements are performed at a grazing angle (~80-85° with respect to the normal to the surface) in order to achieve maximum signal/noise ratio. **Figure 21** illustrates the amplitudes, at the surface, of the parallel (p-) and perpendicular (s-) polarized IR fields at grazing incidence. p- and s-polarization refer to radiation polarized parallel to the incident plane and perpendicular to the incident plane, respectively. As shown in **Figure 22**, there is zero amplitude at the surface for s-polarized radiation due to the 90° change in phase on reflection but p-polarized radiation shows almost twice the amplitude at the surface due to constructive interference between the in-phase incident (E_p^i) and reflected (E_p^r) fields. The enhanced p-polarization field at the surface may be described as $E_\perp$ as it is perpendicular to the surface plane.

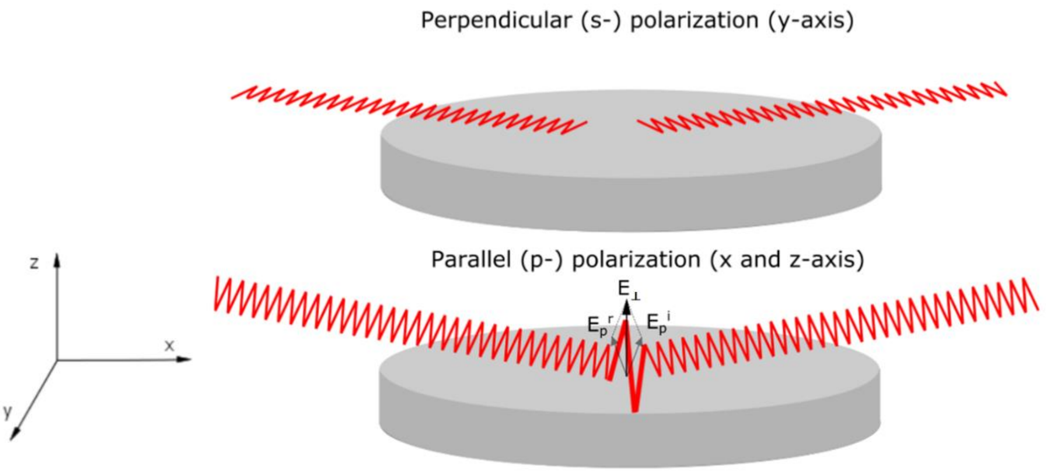

Figure 21 S-polarization and p-polarization amplitudes at grazing incidence in the RAIRS method.

The red curve in **Figure 22** shows the $E_\perp$ amplitude at the surface, relative to E_p^i, as a function of the angle of incidence. The blue curve shows the corresponding dependence of the RAIRS intensity as given by **Equation 3**. As the angle of incidence is increased towards grazing incidence an increasingly larger area of the surface is irradiated, as described by $1/\cos\theta$. Hence the maximum RAIRS intensity (I) is with the beam aligned at ~80-85° with respect to the normal to the surface.

$$I = \left(\frac{E_\perp}{E_i}\right)^2 \frac{1}{\cos\theta} \quad \textbf{Equation 3}$$

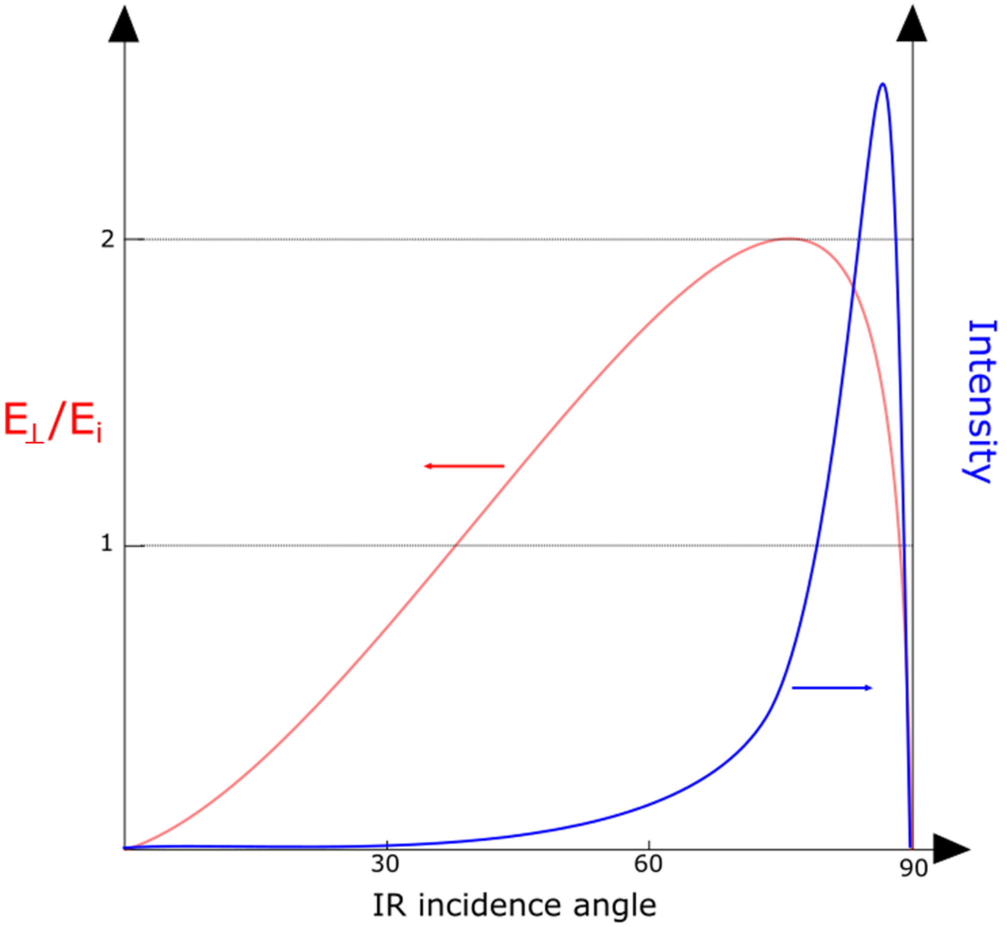

Figure 22 The red curve shows the amplitude of the electromagnetic field, $E_\perp$, at the surface as a function of the angle of incidence. E_i is the amplitude of the incident p-polarized field. The blue line shows the intensity of the field perpendicular to the surface, adjusted for the fact that a higher area of the surface is irradiated at very high angles of incidence [75].

Vibrational modes in RAIRS are subject to a strict metal surface selection rule: only transition dipole moments (M) with a component normal to the surface can produce active RAIRS bands. M is the dipole moment derivative with respect to the vibrational coordinate. The selection rule can be understood, as shown in **Figure 23**, by considering the vector sum of a molecular dipole on the surface and its image dipole in the metal. The intensity of a given band in a RAIRS spectrum of a molecule on a metal surface is proportional to the square of the scalar product of the transition dipole moment and the electric field at the surface (**Equation 4**).

$$I \propto |M \cdot E_\perp|^2 \qquad \textbf{Equation 4}$$

The resulting RAIRS intensity of a given mode then scales as $\cos^2 \theta$ with respect to the angle between transition dipole moment (M) and the normal to the surface (**Figure 23**). No signal is detected for the case where the transition dipole moment is parallel to the surface. Maximum absorbance occurs for case where the transition dipole moment is perpendicular to the surface.

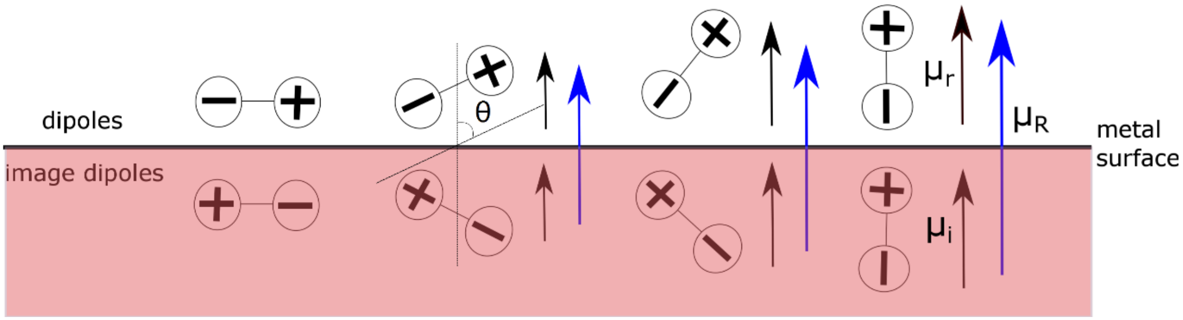

Figure 23 Schematic illustration of the RAIRS selection rule on a metal surface in terms of the sum of molecular and image dipoles. The example to the extreme left shows zero dipole moment perpendicular to the surface. The example to the extreme right shows a doubling of the dipole moment perpendicular to the surface and zero dipole moment parallel to the surface.

The RAIRS metal surface selection rule may also be considered in terms of the molecular symmetry of the adsorbed molecule. An example is shown in **Figure 24** by considering three CF_3 vibrational modes of 3-aminobenzotriflouride (3ABTF). Joshua et al. interpreted the IR spectrum of 3ABTF under the assumption that the molecule displays C_s symmetry [76]. The aromatic ring lies in the mirror plane. The vibrational modes transform either in the plane (a´ symmetry species) or out of the plane (a´´ symmetry species). As summarized in **Table 1**, Joshua et al. assigned a band at 1341 cm^{-1} to a C_{aryl}-CF_3 symmetric stretching vibration (a´), a band at 1161 cm^{-1} to an in-plane (a´) CF_3 stretching vibration, and a band at 1123 cm^{-1} to an out-of-plane (a´´) CF_3 stretching vibration 76. **Figure 24** shows two extreme orientations of non-distorted 3ABTF on a metal surface. In structure I, where the molecule is perpendicular to the surface, the two a´ modes are RAIRS active and the a´´ mode is RAIRS inactive. In structure II, where the molecule is parallel to the surface, only the a´´ mode is strongly RAIRS active. For simplicity, the C_{3v} point group terminology, in-plane asymmetric vibration and out-of-plane asymmetric vibration, will be used in this thesis to describe the bands at 1161 and 1123 cm^{-1}, respectively.

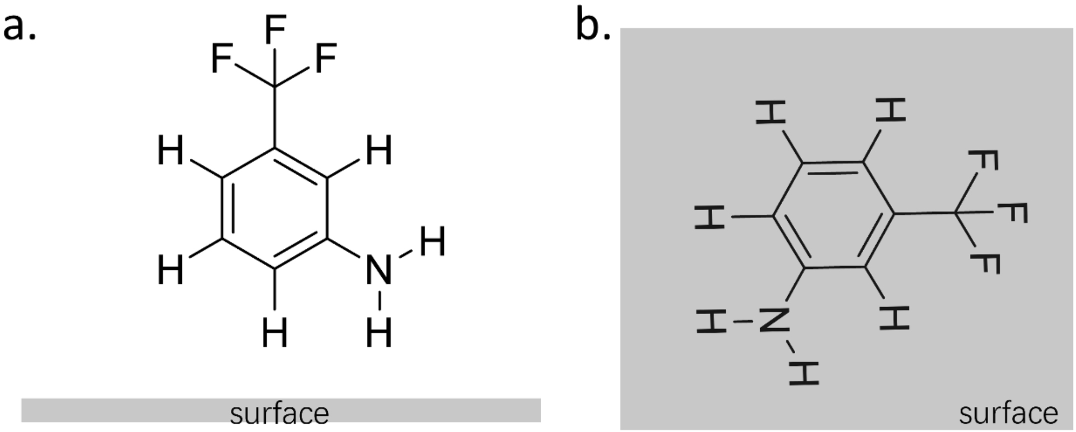

Figure 24 Schematic illustration of two orientations of 3-aminobenzotriflouride with respect to a planar metal surface. (a) An upright orientation (structure I). (b) A flat-lying orientation (structure II).

Figure 25a presents a photograph of the under-vacuum RAIRS system used for the experiments. The system contains 5 main units: (i) The IR source and interferometer; (ii) the ultra-high vacuum (UHV) chamber; (iii) two sets of mirrors to perform grazing incidence experiments; (iv) IR detectors; (v) a pumped gas-handling system that is separated from the UHV chamber by valves. Radiation from the IR spectrometer (VERTEX 80v, BRUKER) is passed through a wire grid polarizer to select p-polarization. The InSb detector displays high sensitivity in the 3000 cm^{-1} region and is used to obtain CH stretching spectra. The narrow-band HgCdTe (MCT) detector displays highest sensitivity in the mid-frequency region, and is used to obtain CH_3 deformation and CF_3 spectra. Two detectors are used to obtain optimal performance over the complete spectral range since the so the signal is very weak because the number of molecules on the surface is very small (about 10^{13}-10^{14} per cm^2). **Figure 25b** shows a Pt(111) sample in the middle of UHV chamber. The IR beam is directed onto the Pt(111) surface at grazing incidence to achieve optimal signal/noise ratio. The sample holder is made of a tantalum sheet, and the single crystal is spot-welded to the sample holder. Type K thermocouples are spot-welded on the back of the sample. The presented RAIRS spectra represent a ratio of 1400 sample scans to 1400 scans of the surface prior to adsorption (background). The baseline was corrected by a smooth cubic spline fitted to manually picked points (less than 5 points).

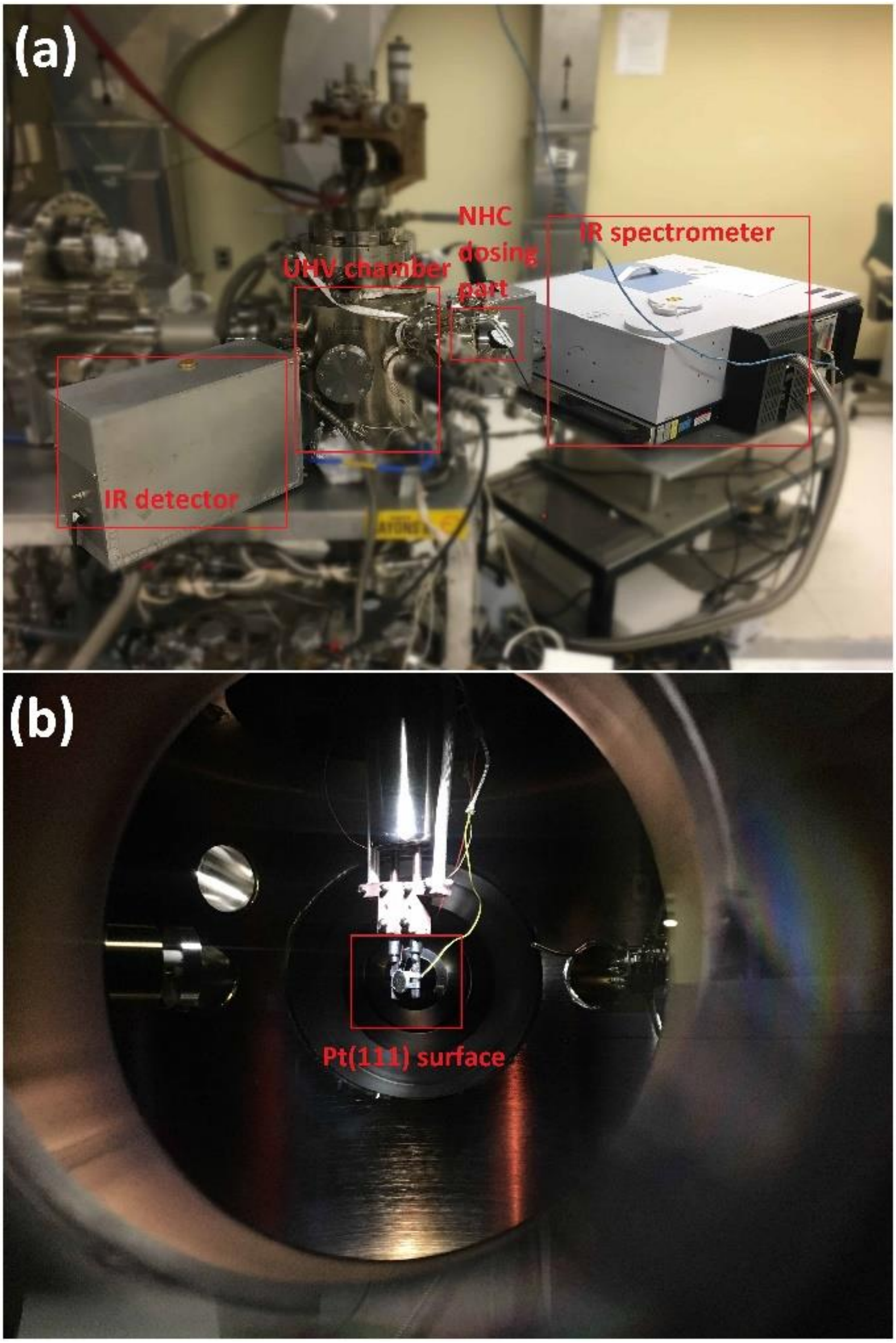

Figure 25 (a) Photograph of the experimental system. (b) Photograph of the Pt(111) sample mounted on the sample manipulator in the UHV chamber.

Chapter 2 NHC Functionalization of Pt(111) and Ru(0001) Surfaces

2.1 Introduction

Carbenes on metallic surfaces are fascinating species both from an applied and a fundamental perspective [1,78–82]. In organometallic complexes, N-heterocyclic carbenes (NHCs) [4,81,83–88] offer electronic control due to their σ-donor properties, robustness due to strong ligand-metal bonding, and steric control due to the modulable structure of the wingtips [81]. By extension, there is intense research interest on the use of NHCs to tune the properties of metal nanoparticles, clusters and extended surfaces. The great majority of the work on extended surfaces deals with coinage-metal substrates [2,3,78,79,89–96] while studies of Pt-group surfaces are much rarer[18,97–103]. The latter metals are chemically more reactive than coinage metals in part because they have incompletely filled d-bands. The modulation of catalytic properties is but one aspect of the use of NHC as surface ligands, other potential applications extend to the field of nanoelectronics [104]. Hence, there is critical need to define the interactions of NHCs with a wider range of surfaces.

The powerful ability of NHC ligands to tune surface properties of Pt-group metals is revealed in many exciting recent reports on catalytic activity and selectivity [105,106]. Following Chaudret and co-workers pioneering work on NHC-stabilized Ru nanoparticle (NP) catalysts [107], several groups investigated NHC-stabilized Pt [108], Ir [109], Ru [110–114], Pd [111] and Rh [115] NPs in relation to catalytic activity and selectivity. The NHC wingtip groups can have large effect on catalytic selectivity through restricting contact with the surface to specific molecular functions. For example, Glorius and co-workers used long-chain NHC-stabilized Ru NPs for the chemoselective hydrogenation of styrene, preventing reduction of the phenyl moiety [116]. NHCs can also be used to induce catalytic activity, as reported by Glorius *et al.* for Buchwald-Hartwig amination over Pd/Al_2O_3 [111]. Chaudret, Pieters and co-workers reported the remarkable performances of NHC stabilized Ru and Ir nanoparticles for hydrogen isotope exchange, C-H functionalization, reactions [117], and Coperet and co-workers [99] engineered enhanced electrochemical CO_2 reduction activity of Pd catalysts by using tripodal NHC surface chelation.

The modulation of catalytic properties is but one aspect of the use of NHC as surface ligands, other potential applications extend to the field of nanoelectronics [104]. Hence, there is critical need to define the interactions of NHCs with a wider range of surfaces. The formation of NHCs on Pt(111) and Ru(0001) were explored using the two precursor salts shown in **Figure 26**. The preliminary study on Pt(111) using **NHC-1·H_2CO_3** will be briefly summarized [18]. Then the formation of NHCs on Pt(111) and Ru(0001) using **NHC-2·H_2CO_3** will be described in detail. The precursor salts were provided by Crudden's group form Queen's University, Department of Chemistry.

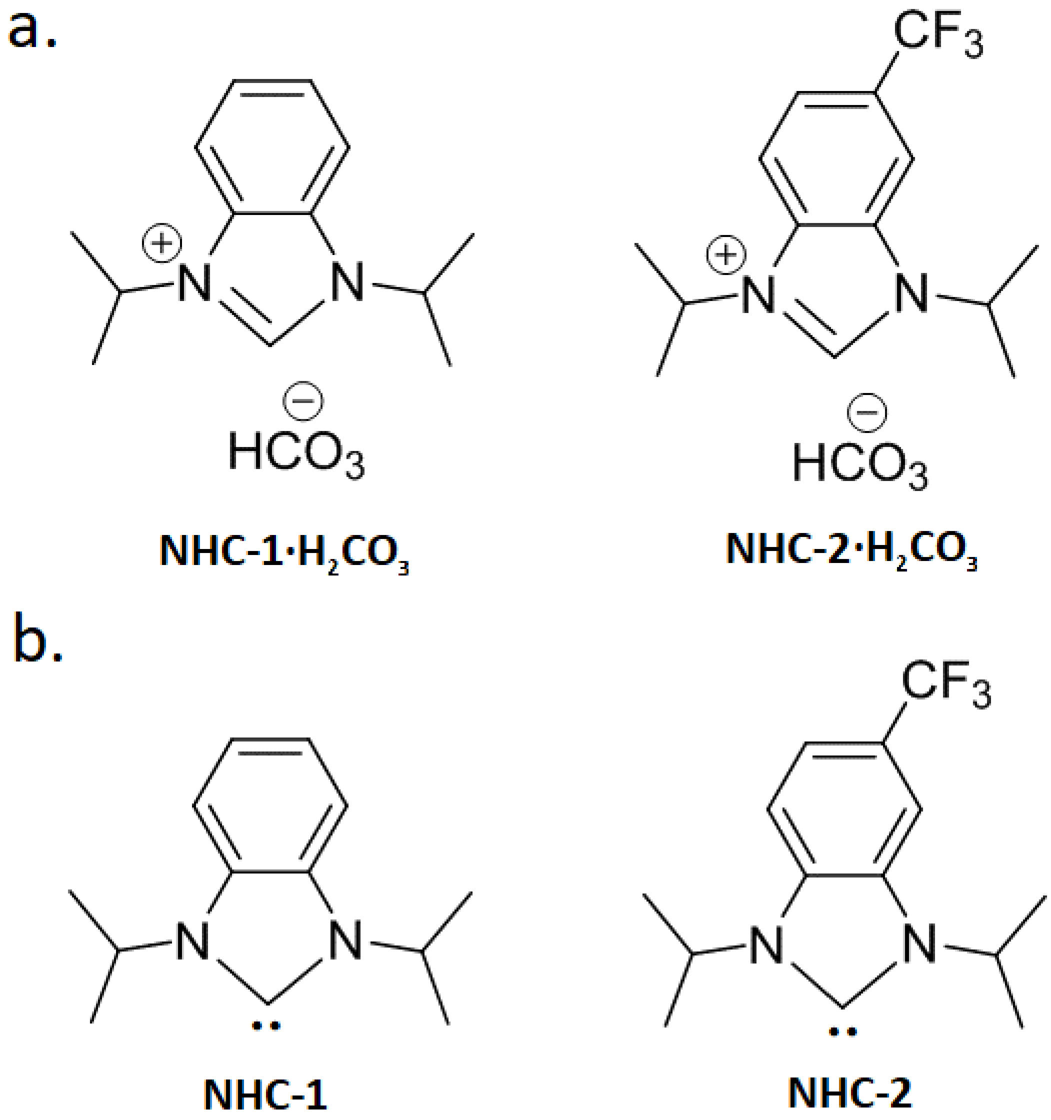

Figure 26 (a) The NHC precursor salts used in this study. (b) The corresponding NHCs.

2.2 Experimental Methods

The Pt(111) surface was cleaned by repeated cycles of Ar (~2×10^{-6} Torr) ion bombardment at 600 K for 20 min and O_2 (~2×10^{-7} Torr) treatment at 900 K for 20 min. After Ar^+ bombardment and O_2 cleaning, the Pt(111) surface was annealed to 1000 K. The Ru(0001) surface was prepared by Ar (~2×10^{-6} Torr) ion bombardment at 700 K for 20 min and O_2 (~2×10^{-7} Torr) treatment at 1000 K for 20 min followed by anneals to 1000 K under vacuum. The NHC precursor (**NHC-1·H_2CO_3** or **NHC-2·H_2CO_3**) was loaded into a glass tube separated from the UHV chamber by a gate valve. The loaded NHC precursor was outgassed for 12 h at room temperature in the gas-handling line before dosing into the UHV chamber. Using a heating tape wrapped around the glass tube, the NHC precursor was warmed to 70 °C to raise the vapor pressure to, about 10^{-2} Torr. Subsequently, the gate valve was gradually opened in order to dose NHC precursors into the UHV chamber, at a pressure of ~3×10^{-7} Torr. The temperature of the Pt(111) sample in the UHV chamber was varied by cooling down the sample holder using liquid nitrogen and heating using a temperature control power supply. RAIRS measurements were performed using p-polarized (parallel to the plane of incidence) radiation at grazing incidence. Mercury Cadmium Telluride (MCT) (2300-700 cm^{-1}) and Indium Antimonide (InSb) (3500-2300 cm^{-1}) detectors were used. According to the structure of the NHCs, the MCT detector can provide information of aromatic C-H bending modes, the C=N stretching mode and alkyl group deformation modes, as well as on CO stretching modes of the NHC precursor salt. For **NHC-2**, the MCT detector optimizes the signal in the C-F stretching region. The InSb detector optimizes signal in the C-H stretching and carbonate O-H stretching region.

2.3 Interaction of NHC-1·H_2CO_3 with Pt(111)

NHC-1·H_2CO_3 was dosed onto the Pt(111) surface at a relatively low temperature (230 K). RAIRS spectra obtained using the InSb detector are shown in **Figure 27**. The broad peak at 3355 cm^{-1} is attributed to the carbonate OH vibration of **NHC-1·H_2CO_3** which indicates physical adsorption of **NHC-1·H_2CO_3** at 230 K. Vibrations at 2975, 2933 and 2874 cm^{-1} are attributed to isopropyl CH stretching modes. The carbonate OH band is removed on heating to 300 K. Instead, an aromatic CH stretching band grows in 3064 cm^{-1} when the temperature is increased to 300 K. Based on RAIRS selection rule, only transition dipole moments with a component normal to the surface produce a RAIRS signal. These results show that **NHC-1** ligands are created on Pt(111) at 300 K, and that they are oriented perpendicular to the surface. Crudden and co-workers also found strong aromatic CH stretching intensity for **NHC-1** ligands on Au(111) at 300 K [89]. Interestingly, the isopropyl CH vibrations are removed at 475 K but the aromatic CH vibration at 3064 cm^{-1} still remains until 515 K. This observation suggests that the isopropyl wings are selectively decomposed on the reactive Pt(111) surface. This phenomenon is not found in NHCs-Au(111) systems, which may be because the Au(111) surface is less reactive than the Pt(111) surface. The **NHC-1** ligands can remain intact on Au(111).

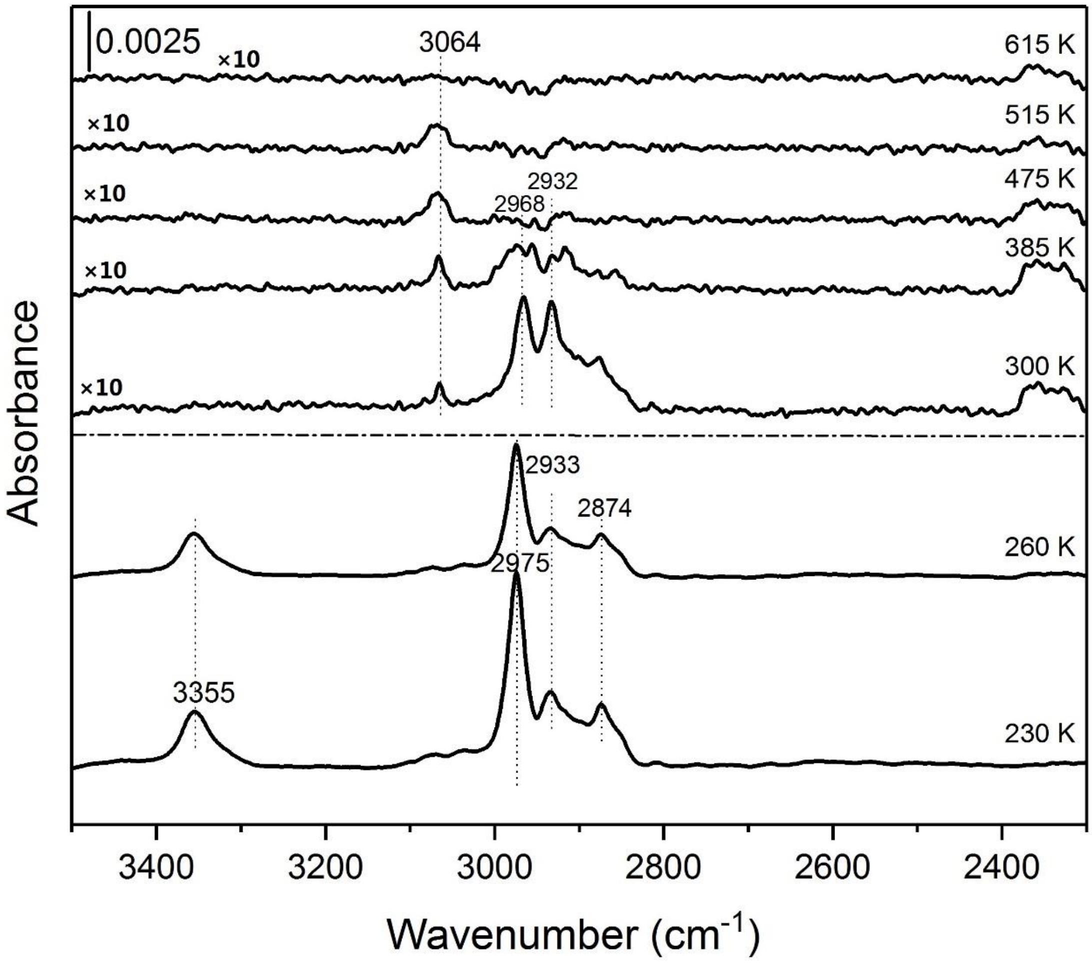

Figure 27 RAIRS spectra acquired using an InSb detector. The Pt(111) sample was exposed to **NHC-1·H_2CO_3** vapor (5.0×10^{-7} Torr, 100 s) at 230 K, and then annealed for 5 min at the indicated temperatures.

To further understand **NHC-1** formation on Pt(111) from **NHC-1·H_2CO_3**, RAIRS measurements were performed in the 1800-700 cm^{-1} range using the MCT detector (**Figure 28**). **NHC-1·H_2CO_3** was dosed onto Pt(111) at 250 K. The peak at 1676 cm^{-1} is attributed to a carbonate CO stretching vibration. It is removed on heating the sample to 280 K. The remaining peaks at 1464, 1367 and 1234 cm^{-1} are attributed to C-C, C-N stretching and C-H bending [15,77,118], indicating that adsorbed **NHC-1** is formed on Pt(111) at 280 K. The bads at 1464 and 1367 cm^{-1} could also be due to isopropyl deformation and bending modes.

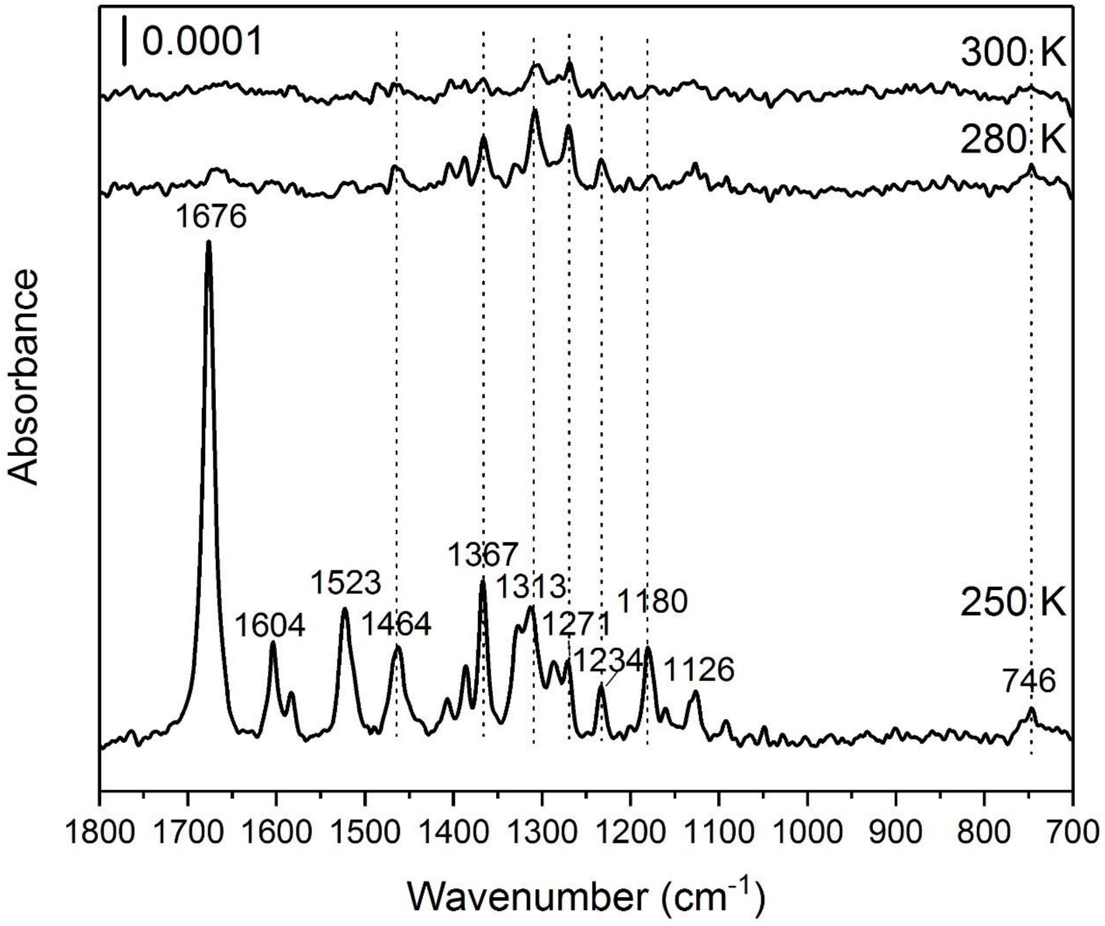

Figure 28 RAIRS spectra acquired using an MCT detector. The Pt(111) sample was exposed to **NHC-1·H_2CO_3** vapor (2.8×10^{-7} Torr, 100 s) at 250 K, and then annealed for 5 min at the indicated temperatures.

Additional experiments were performed by dosing **NHC-1·H_2CO_3** onto Pt(111) at 300 K. As shown in **Figure 29**, the resulting RAIRS spectra display the aromatic and isopropyl CH stretching bands but not the carbonate OH band at 300 K, indicating NHC functionalization of Pt(111) at room temperature. The isopropyl wings group begins to decompose at <435 K: the isopropyl CH stretching bands at 2967, 2931 and 2878 cm^{-1} are already very weak in the RAIRS spectra above 435 K. We cannot identify the exact bond breaking and reorganization that occurs in the isopropyl wingtip groups. However, the aromatic CH stretching band at 3063 cm^{-1} remains strong. Although N-substituent isopropyl wings undergo some bond breaking at ~435 K, the benzimidazolium skeleton is still intact at 515 K (**Scheme 1**).

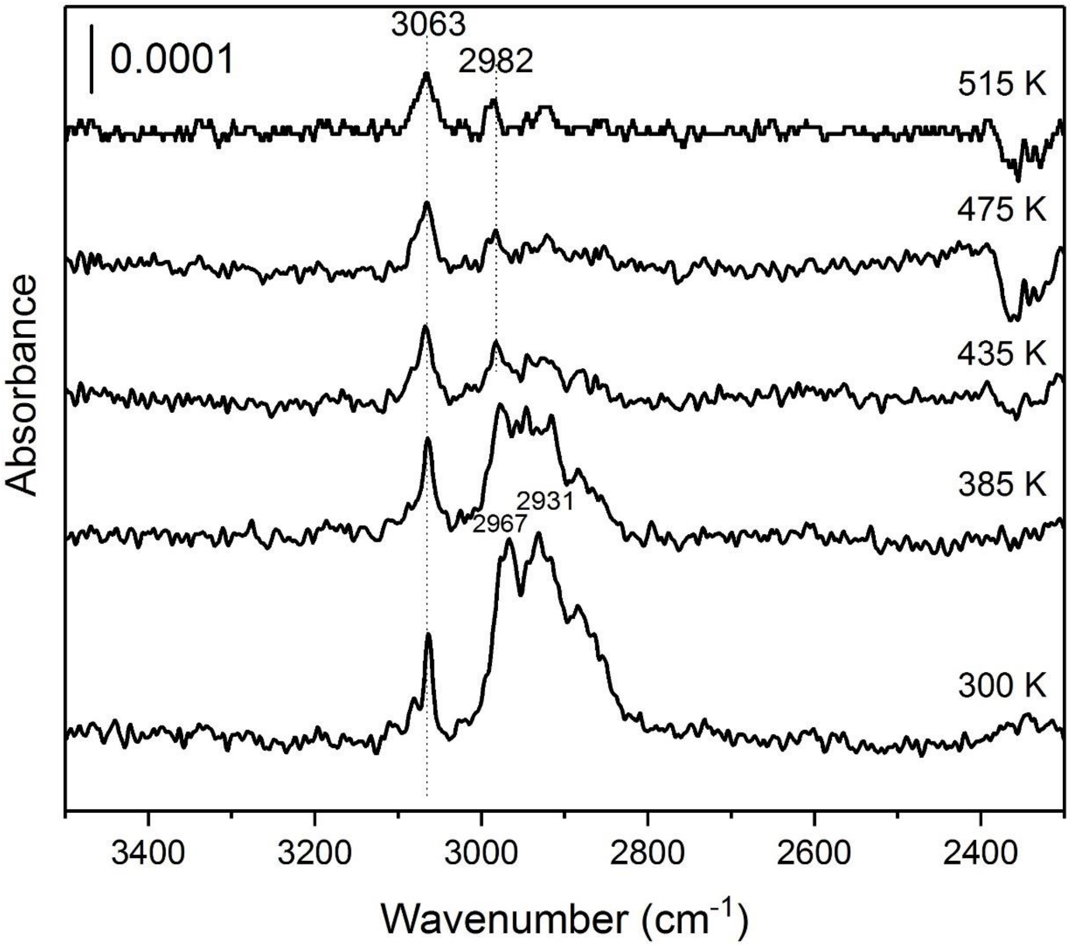

Figure 29 RAIRS spectra acquired after dosing **NHC-1·H_2CO_3** (5.0×10^{-7} Torr, 100 s) at 300 K to Pt(111), and then increasing temperature to the indicated temperatures.

Figure 30 shows RAIRS spectra acquired using the MCT detector for exposure to **NHC-1·H_2CO_3** at 300 K. NHC skeleton vibrations are detected at 1484 cm^{-1}, 1346 cm^{-1} and 1243 cm^{-1} are consistent with NHC functionalization on the surface without the formation of a layer of physically adsorbed precursor. [3] The absence of an out-of-plane aromatic C-H bending mode (in the 700-800 cm^{-1} region), indicates that the **NHC-1** ligands are not flat-lying but are upright on the Pt(111) surface (**Scheme 1**). One reason that NHC ligands are upright on Pt(111) is due to the steric hindrance of isopropyl wings. NHC with small N-substituents groups such as methyl or ethyl substituted NHCs display both flat and upright orientations on Au(111) and Cu(111) surfaces. In contrast, bulky substituents such as isopropyl groups lead to upright orientations on Au(111) and Cu(111) surfaces (**Figure 31**) [15]. The band at 1484 cm^{-1} decreases in intensity on heating to ~430 K consistent with bond breaking in the isopropyl groups.

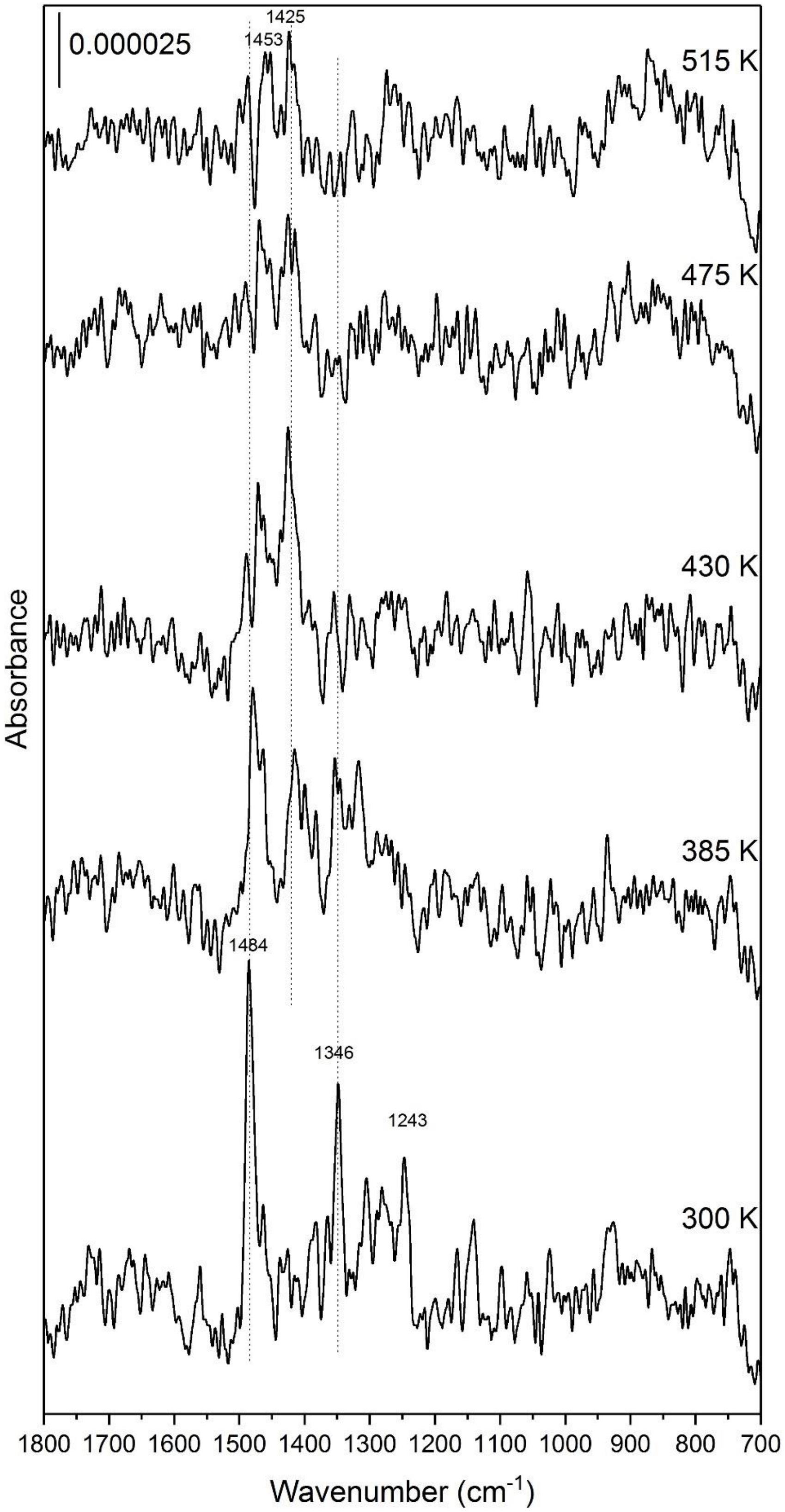

Figure 30 RAIRS spectra acquired after dosing **NHC-1·H_2CO_3** (3.0 × 10^{-7} Torr, 100 s) on Pt(111) at 300 K followed by anneals to the indicated temperatures under vacuum.

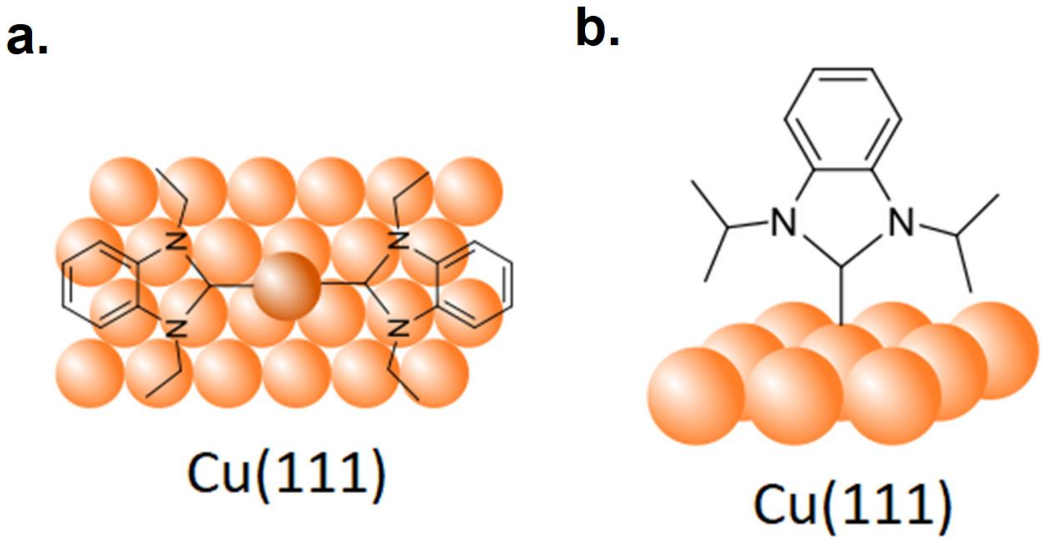

Figure 31 (a) Ethyl substituted NHC on Cu(111). An adatom driven structure is formed. (b) Isopropyl substituted NHC on Cu(111). Reproduced with permission from Ref. [15], copyright 2017 Wiley-VCH Verlag GmbH & Co. KGaA, Weinheim.

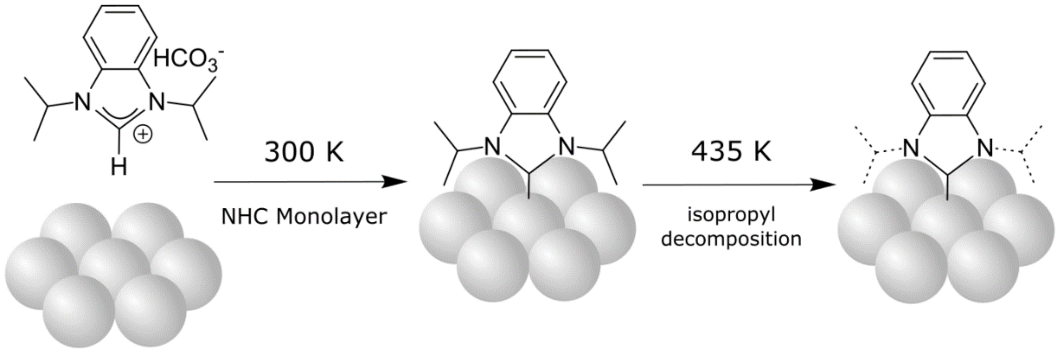

Scheme 1 Formation of surface **NHC-1** ligands on Pt(111) through dosing **NHC-1·H_2CO_3** at 300 K. Proposed isopropyl bond breaking at ~435 K. Reproduced with permission from Ref. [18], copyright 2018 The Royal Society of Chemistry.

2.4 NHC Formation from NHC-2·H_2CO_3 on Pt(111)

Due to the weak IR characteristic, in the 2000-700 cm^{-1} region (Fig. 28, Fig. 30), of **NHC-1** on Pt(111), a CF_3 substituted NHC precursor (**NHC-2·H_2CO_3**) (**Scheme 2**) is introduced in order to provide strong -CF_3 stretching bands to help us to obtain more detailed information about NHC formation on Pt-group metal surfaces. As shown in **Figure 32**, the trifluoromethyl group provides 3 characteristic bands: C-CF_3 symmetric stretching at 1329 cm^{-1} (υ_{sym}(C-CF_3)), CF_3-in-plane asymmetric stretching at 1184 cm^{-1} (in-plane υ_{asym}(CF_3)) and CF_3 out-of-plane asymmetric stretching at 1148 cm^{-1} (out-of-plane υ_{asym}(CF_3)) [119]. The υ_{sym}(C-CF_3) and in-plane υ_{asym}(CF_3) modes are RAIRS active if the NHC is oriented normal to the surface while only the out-of-plane υ_{asym}(CF_3) mode is active for flat-lying NHC. As shown in **Figure 32a**, all of the -CF_3 vibrations can be detected at 300 K. The υ_{sym}(C-CF_3) mode has the strongest intensity among these -CF_3 vibrations, while in-plane υ_{asym}(CF_3) and out-of-plane υ_{asym}(CF_3) vibrations have similar intensities. However, the out-of-plane υ_{asym}(CF_3) is almost completely removed on the increasing temperature of the sample to 400 K, while the υ_{sym}(C-CF_3) and in-plane υ_{asym}(CF_3) intensities remain strong. A carbonate band at 1755 cm^{-1} is detected below 400 K [120,121]. The spectra show that there is a roughly flat-lying molecular structure present at temperatures below 400 K. Specifically, the out-of-plane υ_{asym}(CF_3) mode at 1149 cm^{-1} is observed at 300-350 K. However, broad features in the 1600-1800 cm^{-1} region arising from the bicarbonate moiety of the precursor, are only removed on annealing from 300 to 400 K. Hence, it is not clear whether the out-of-plane υ_{asym}(CF_3) band arises from a flat-lying carbene state or some remaining adsorbed precursor or CO_2 adduct. As discussed below, data for carbene formation on Ru(0001) provide clarity on this issue.

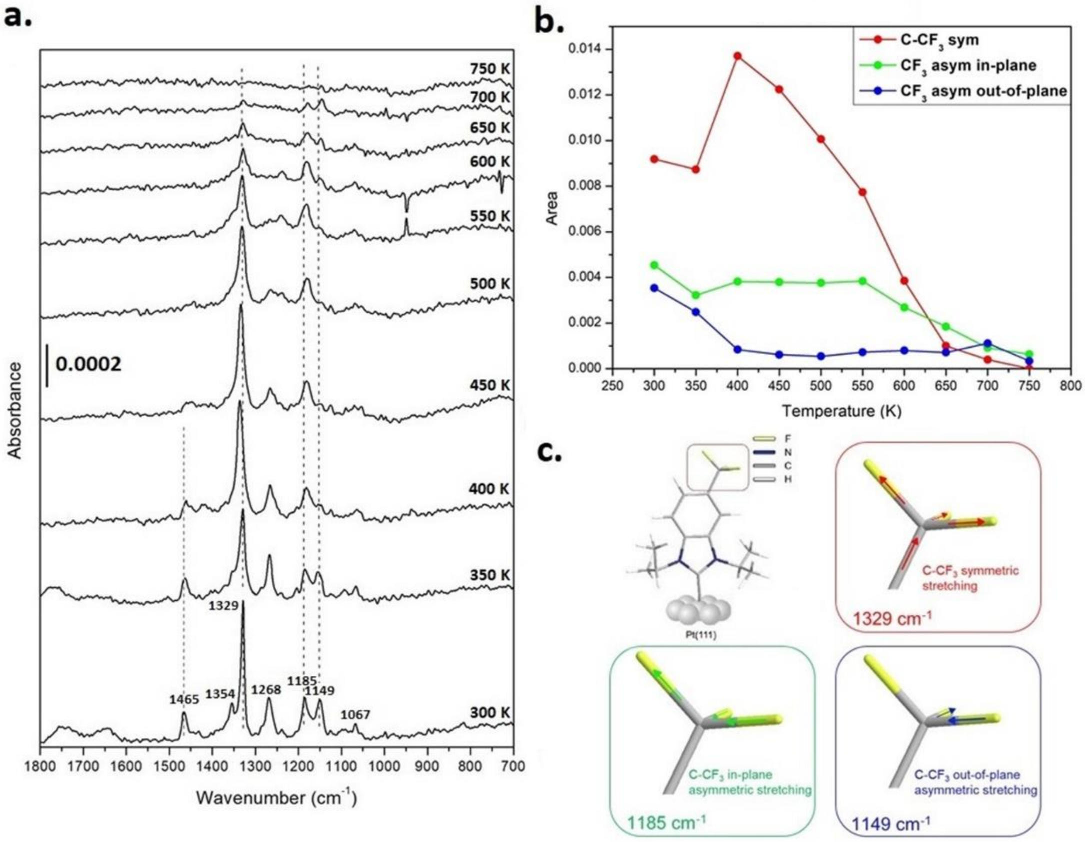

Figure 32 (a) RAIRS spectra of Pt(111) exposed to **NHC-2·H_2CO_3** vapor. The sample was held at 300 K during gas exposure and then annealed for 5 min at the indicated temperatures. (b) Temperature dependence of the integrated RAIRS intensities of the C-CF_3 symmetric stretching (red), the in-plane asymmetric CF_3 stretching (green) and the out-of-plane asymmetric CF_3 stretching vibration (blue). The plots present the peak areas of the three bands at the indicated temperatures. (c) Illustration of the three CF_3 vibrational modes used to determine the adsorption geometry of **NHC-2**. Red, green, blue borders enclose drawings of the C-CF_3 symmetric, CF_3 in-plane asymmetric and CF_3 out-of-plane asymmetric stretching vibrations, respectively.

In order to eliminate any contribution of the carbonate precursor to the spectra, experiments in which the precursor was dosed with the sample held at 400 K were performed. As shown in **Figure 33**, the spectra are dominated by the bands at 1334 and 1176 cm^{-1} characteristic of vertically oriented **NHC-2**. There is, however, a notable difference between the spectra in **Figure 32a** and **Figure 33a** in that a band at ~1465 cm^{-1} is clearly present in the 300-400 K range in **Figure 32a** but is absent in **Figure 33a**. This band is attributed to isopropyl vibrations [122]. Similarly, it can be seen from **Figure 32a** that there is a significant attenuation of the band at ~1465 cm^{-1} on annealing from 400 to 450 K, while the υ_{sym}(C-CF_3) and in-plane

$\upsilon_{\mathrm{asym}}(CF_3)$ bands characteristic of the benzimidazolium core remain strong. Hence, a strong attenuation of the isopropyl band is observed for both NHCs on Pt(111) (**Figure 29**). In both cases, the isopropyl CH bonds begin to break at ~435 K, while the aromatic CH stretching signal at 3063 cm^{-1} remains strong. This shows that the isopropyl wings undergo a transformation but the NHC core remains intact, as also indicated by the **NHC-1** C-H stretching data in **Figsure 27** and **29**. A related observation was reported by Steinruck, Libuda and co-workers [123,124]. They found that N-methyl, N-ethyl and N-propyl carbazoles undergo dealkylation on Pt(111) at ~390 K. The higher dealkylation temperature (~450 K) observed in the present study is attributed to the fact that the C-metal bond in the vertically oriented carbene distances the wingtip group from the surface.

Figure 33b shows the results of an experiment performed by dosing **NHC-2·H$_2$CO$_3$** onto ethylidyne (C-CH$_3$) functionalized Pt(111) so as to examine adsorption on an already crowded Pt(111) surface. Ethylidyne was prepared by exposing 3 L (3 × 10^{-8} Torr for 100 s) ethylene at 300 K, followed by annealing the sample to 350 K for 5 min to obtain ethylidyne ligands [125], then back to 300 K to obtain RAIRS spectra. Characteristic bands of ethylidyne, including C-C stretching at 1119 cm^{-1} and symmetric CH$_3$ stretching at 1339 cm^{-1} are clearly present at 300 K [126]. The observation of $\upsilon_{\mathrm{sym}}(C\text{-}CF_3)$ and in-plane $\upsilon_{\mathrm{asym}}(CF_3)$ bands at 1330 and 1180 cm^{-1} shows that ethylidyne does not block the formation of the vertically oriented surface carbenes. Furthermore, it does not block the strong attenuation of the isopropyl band (1468 cm^{-1}) intensity above 400 K.

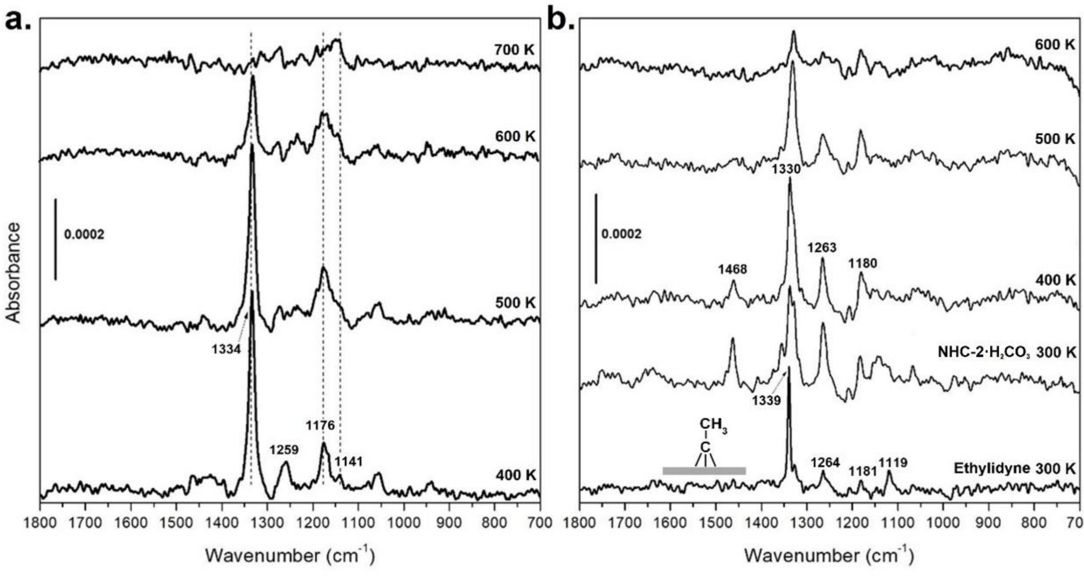

Figure 33 (a) RAIRS spectra taken following exposure of Pt(111) at 400 K to **NHC-2·H$_2$CO$_3$**. (b) Spectra taken following exposure of ethylidene functionalized Pt(111) to **NHC-2·H$_2$CO$_3$**.

2.5 NHC-2 Ligands on Ru(0001)

Data for **NHC-2** formation on Ru(0001) are presented in **Figure 34**. Strong υ_{sym}(C-CF$_3$) and in-plane υ_{asym}(CF$_3$) bands at 1330 cm^{-1} and 1185 cm^{-1} are observed at 300 K, respectively. The peaks which are characteristic of vertically oriented **NHC-2** are isolated in the spectra taken after annealing to 500 and 550 K. As observed for Pt(111), an isopropyl related band at 1465 cm^{-1} is removed on annealing to 450 K while bands characteristic of the NHC backbone remain intact. It is concluded that CN bond breaking occurs on Ru(0001) leading to dealkylation of the surface **NHC-2**.

The carbonate vibrations at 1623 cm^{-1} and 1593 cm^{-1} differ from the spectrum produced by **NHC-2·H$_2$CO$_3$** on Pt(111) at 300 K. These two peaks at 1623 cm^{-1} and 1593 cm^{-1} are tentatively attributed to asymmetric CO$_2$ stretching vibrations [127,128], suggesting that there may be a CO$_2$ adduct formed. In contrast to the observations on Pt(111), the out-of-plane υ_{asym}(CF$_3$) at 1147 cm^{-1} is still observed at 400 K, but the characteristic **NHC-2·H$_2$CO$_3$** vibrations are removed. The data strongly suggest that a flat-lying state of **NHC-2** existes on Ru(0001). The removal of the band at 1147 cm^{-1} on annealing from 400 to 500 K results in an increase in the integrated intensities of the υ_{sym}(C-CF$_3$) band (**Figure 34b**), consistent with the conversion of a flat-lying state to a vertical state (**Scheme 2**).

The flat-lying state detected on Ru(0001) at 400 K is attributed to a binding configuration dominated by the interaction of the chemisorbed benzyl-ring with the metal. This interpretation is based on results from a comparative study of benzene adsorption on Cu(111), Pt(111) and Ru(0001) by Jia and An [129]. Their calculated adsorption energies depend on the dispersion-corrected DFT functional used (optB88, optB88b or DFT-D3), yielding values in the ranges 0.75-1.1 eV for Cu(111), 1.75-2.2 eV for Pt(111) and 2.2-2.7 eV for Ru(0001). We propose that the much stronger interaction of the aromatic group with Ru(0001) traps a greater fraction, compared to Pt(111), of the benzimidazolium structure into a flat-lying state. Hence, although there is competitive formation of flat-lying states on Pt(111) and Ru(0001), the state is more easily detected on Ru(0001) where it is present to a higher coverage.

A number of features in the spectra for both Pt(111) and Ru(0001) are consistent with bond breaking events that produce adsorbed fragments containing CF bonds. A strong band at 1268 cm^{-1} and weaker features at slightly lower energies are seen for both **NHC-2** on Pt(111) and Ru(0001) systems. However, these bands are not seen in the **NHC-1** on Pt(111) system (**Figure 30**). Vibrational studies of hydrocarbons containing CF$_3$ groups, such as hexafluoroacetone on Pt(111) [130], show features in the 1260-1240 cm^{-1} region and vibrational bands in the 1240-1200 cm^{-1} range were reported for CF$_3$I treated Pt(111) and Ru(0001) surfaces [131,132]. Hence, while the use of a CF$_3$ substituent in the present study facilitates the acquisition of strong RAIRS signal it has the drawback of depositing species containing C-

F bonds on the surface, most likely through bond-breaking in the flat-lying states. As mentioned above, Crudden *et al*. reported decomposition from flat-lying NHC-adatom-NHC states on Cu(111) [15].

Information on the thermal stability of NHCs on Pt(111) and Ru(0001) may be gained from **Figure 32b** and **34b** in which the integrated intensities of the υ_{sym}(C-CF$_3$), in-plane υ_{asym}(CF$_3$) and out-of-plane υ_{asym}(CF$_3$) bands are plotted. The υ_{sym}(C-CF$_3$) intensity is used to monitor the thermal stability of the vertically oriented NHC surface ligands. The surface **NHC-2** is detected to 700 K on Pt(111) and to 600 K on Ru(0001). The temperature ranges over which there is a sharp drop in the υ_{sym}(C-CF$_3$) intensity are 600-650 K for Pt(111) and 550 to 600 K for Ru(0001). These temperature ranges are close to those reported for the removal **NHC-1** from Au(111), ~610 K, as determined by XPS, [91] thermal desorption [89] and TOF-SIMS [133] measurements.

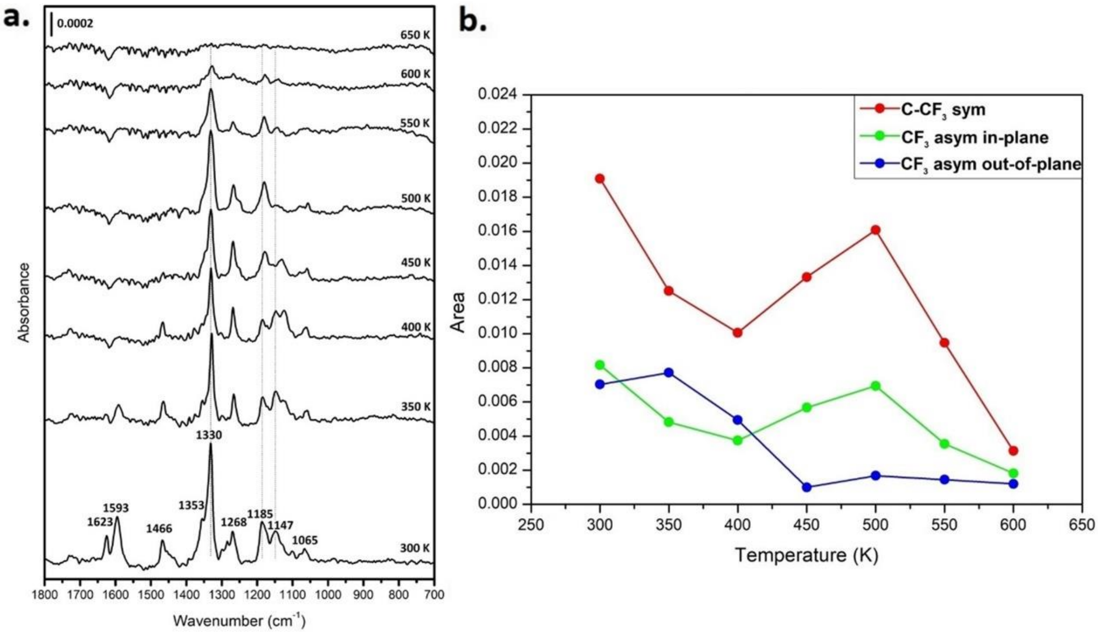

Figure 34 (a) RAIRS spectra of Ru(0001) exposed to **NHC-2** precursor vapor. (b) Temperature dependence of the integrated intensities of the C-CF$_3$ symmetric stretching (red), the in-plane asymmetric CF$_3$ stretching (green) and the CF$_3$ out-of-plane asymmetric stretching bands (blue). The plots present the peak areas at the indicated temperatures

Table 1 Assignment of vibrational frequencies (cm^{-1}) of adsorbed **NHC-2** by reference to the IR spectrum of α,α,α-trifluorotoluene [134] and 3-(trifluoromethyl)aniline[119].

Assignment	C_6H_5-CF_3 [119,134]	**NHC-2** on Pt(111)	**NHC-2** on Ru(0001)
υ_{sym} (C-CF_3)	1325	1329	1330
In-plane υ_{asym}(CF_3)	1175	1185	1185
Out-of-plane υ_{asym}(CF_3)	1128	1149	1147

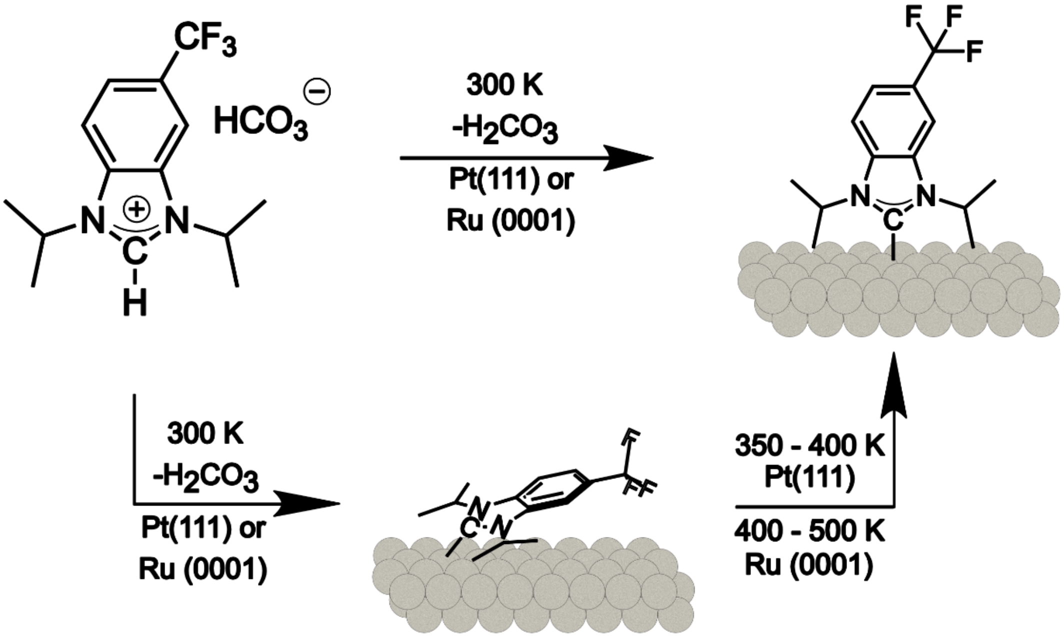

Scheme 2 Adsorption of **NHC-2·H_2CO_3** to form flat-lying and vertical states of **NHC-2** on Pt(111) and Ru(0001) surfaces.

Tang *et al.* [101], recently reported a comprehensive set of DFT calculations on the interaction of 1,3-dimethylbenzimidazolylidene with a wide set of substrates. They found adsorption energies on Au(111), Pt(111) and Ru(0001) of 2.76, 3.25 and 2.66 eV, respectively, and Au-C, Pt-C and Ru-C bond lengths of

2.10, 1.99 and 2.66 Å. In each case, on-top, σ-donor, adsorption was favored, forming a vertically oriented NHC on Au(111) and Pt(111) and a slightly tilted state on Ru(0001). Electron transfer to the metal was found to be greater for Pt(111) than for Ru(0001) or Au(111). Bonding to metal adatoms was also investigated. Stable shallow V-shaped NHC-adatom-NHC dimer configurations were predicted to form on Pt(111) and Ru(0001). The findings by Tang et al. for the NHC on Au(111) are in general agreement with DFT studies on the NHC/Au(111) interface by other groups [94,135,136] and also with the work of Fyta *et al.* [102] on Au(111) and Pt(111). Hence, we take the calculations by Tang *et al.* as an internally consistent set of data with which to compare our experimental data.

There is agreement between the experimental and theoretical work in that a vertically oriented NHC is formed on Pt(111) and Ru(0001). Furthermore, the apparent thermal stability of the NHC is higher on Pt(111) than on Ru(0001), while the apparent stability on Ru(0001) is similar to that on Au(111), in agreement with the calculations. The observation of roughly flat-lying states below ~450 K could indicate the presence of a shallow V-shaped configurations, displaying a RAIRS active out-of-plane $\upsilon_{asym}(CF_3)$ band at ~1147 cm^{-1}. While, STM measurements are required to investigate if such states are formed, we propose that flat-lying states on Pt(111) and Ru(0001) are formed simply by π-chemisorption of the benzimidazolium core on the coordinatively saturated (adatom-free) surface. The dealkylation process revealed by the experimental data is in line with the strong wingtip to metal interaction predicted for Pt(111) by Fyta *et al* [102].

Next, we discuss complications in relating the thermal stability of an NHC on Pt(111) or Ru(0001) to the C-metal bond strength. Two opposing effects are at play with respect to the thermal stability of NHCs on Pt and Ru. First, as shown above, the reactive metals induce bond-breaking even to the extent of removing the wingtip groups. In addition, the present results show that strong chemisorption interactions result in thermally stable flat-lying benzimidazolium states. These properties are in contrast to Au substrates where NHCs appear to remain intact until desorption at ~600 K. Dissociation from flat-lying states has been reported, however, for NHC on Cu(111) [15]. Second, bond-breaking on Pt(111) and Ru(0001) leads to the blocking of active dissociation sites (self-poisoning), thereby stabilizing remaining surface NHC against further decomposition. This effect, typical of reactive surfaces, [137,138] is perhaps directly manifested in the present study where RAIRS bands due to CF bond containing surface fragments disappear (~600 K) prior to the full removal of signal due to the surface carbene. CF bond containing surface fragments are known to be removed from Pt(111) and Ru(0001) surfaces through desorption above 600 K [132,139].

2.6 Summary and Conclusions

NHC-1 ligands are generated on Pt(111) at 300 K as evidenced by the appearance of the in-plane aromatic CH stretching band and the disappearance of the carbonate O-H vibration. The loss of the isopropyl wings occurs at ~435 K as evidenced by the disappearance of isopropyl CH bands at 2931 and 2878 cm^{-1} , as well as the removal of a band at 1465 cm^{-1}. However, the **NHC-1** skeleton still remains on Pt(111) until 515 K.

NHC-2 ligands on Pt(111) and Ru(0001) display strong CF_3 vibrations, including $\upsilon_{\mathrm{sym}}(C\text{-}CF_3)$, in-plane $\upsilon_{\mathrm{asym}}(CF_3)$ and out-of-plane $\upsilon_{\mathrm{asym}}(CF_3)$ stretching, that permit a determination of the adsorption orientation. Vertically oriented **NHC-2** are formed on the Pt(111) and Ru(0001) surface but there is also competitive adsorption into flat-lying states. Especically for **NHC-2** on Ru(0001), there is a strong signal due to flat-lying **NHC-2** below ~450 K. The flat-lying state of **NHC-2·H_2CO_3** is gradually converted to a vertical state on both surfaces with increasing temperature to ~500 K. The $\upsilon_{\mathrm{sym}}(C\text{-}CF_3)$ intensity is used to monitor the thermal stability of the vertically oriented NHC surface ligands. The surface **NHC-2** is detected to 700 K on Pt(111) and to 600 K on Ru(0001).

Chapter 3 Functionalization of Graphene on Pt(111) and Ru(0001)

3.1 Introduction

There are several demonstrated methods to achieve covalent modification of graphene, [37,63,140–148] such as cycloaddition reactions [145,149], nitrene addition[150,151], Diels-Alder cyclization [152], diazonium activation [63,153–155] and carbene grafting [156], all of which transform graphene carbon atoms from sp^2 to sp^3 hybridization at reaction sites [64,157]. Among these methods, the diazonium approach, in which aryl radicals form a C-C bond, (**Scheme 3a**) is the most efficient and widely used. Diazonium salts are generated from anilines and, in general, electrochemical activation is used to generate the aryl radicals which form a covalent bond to graphene. Given the success of the diazonium approach, the possibility of NHC modification of graphene (**Scheme 3b**) should also be explored as NHCs offer potential advantages. Compared with aryl radicals, imidazolium and benzimidazolium NHCs are expected to display different graphene modification properties due to their strong σ-donor properties [83]. The persistent carbene property intrinsic to NHCs may offer a method to achieve vapor-phase functionalization with minimal formation of adsorbed side products [158]. For the same reason, NHCs may offer greater control for homogeneous functionalization [158] in that they are less indiscriminately reactive than aryl radicals. In the present study, we use 1,3-diisopropyl-6-(trifluoromethyl)-1H-benzo[d]imidazol-3-ium hydrogen carbonate, **NHC-2·H_2CO_3**, as an NHC precursor (**Figure 26a**) to explore the functionalization of metal supported graphene under ultrahigh vacuum conditions.

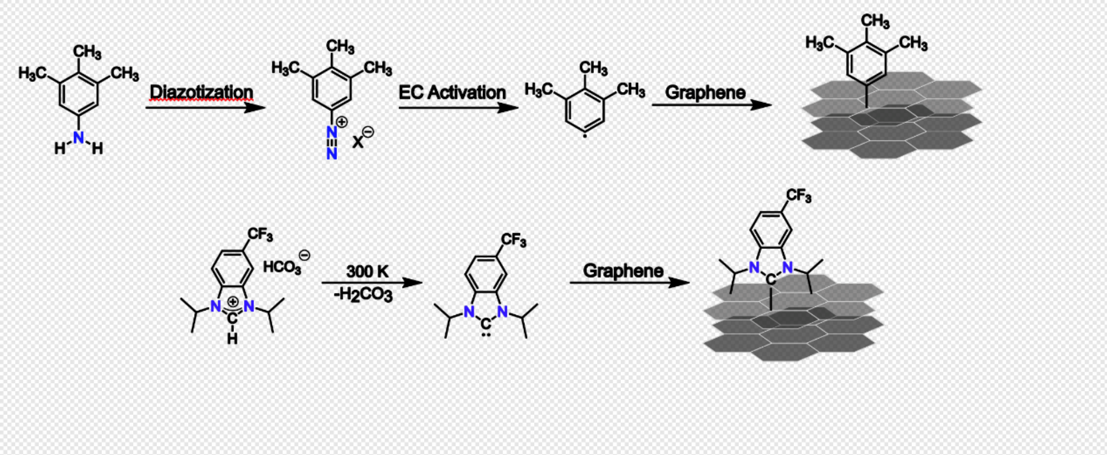

Scheme 3 Formation of C-C bonds to graphene. (a) Electrochemical (EC) grafting using diazonium salts. (b) Proposed vapor-phase NHC method.

3.2 Experimental Methods

The Pt(111) and Ru(0001) single crystals were mounted on a temperature controllable sample holder in a UHV chamber. The Pt(111) sample was cleaned by repeated cycles of 3×10^{-6} Torr Ar ion bombardment at 600 K for 20 min followed by an anneal to 900 K for 20 min under 3×10^{-7} Torr O_2. Similarly, the Ru(0001) substrate was cleaned by ion bombardment at 700 K followed by an anneal to 1000 K for 20 min under 3×10^{-7} Torr O_2. Prior to experiments, both substrates were annealed to 1000 K several times until the chamber pressure was below to 3×10^{-10} Torr. Graphene was formed on both surfaces by chemical vapor deposition (CVD) under 10^{-7} Torr ethylene (98.5 % purity). The preparation of a range of graphene coverages, from low to full monolayer coverage, on Pt(111) and Ru(0001) was guided by reported LEEM (low energy electron microscopy) studies of chemical vapor deposition (CVD) on these surfaces using ethylene as the carbon source. [42–44] Graphene was grown on Pt(111) and Ru(0001) through 10^{-7} Torr ethylene exposure with the samples held at 950 and 1000 K, respectively.

3.3 NHC-2 Ligands on Gr/Pt(111) and Gr/Ru(0001)

As detailed in Chapter 2, the interaction of **NHC-2** with Pt(111) and Ru(0001) results in two competing adsorption configurations on both surfaces. One is adsorption mode a vertically oriented surface carbene, characterized by the selective activity of the pair of $\upsilon_{\mathrm{sym}}(C\text{-}CF_3)$ and in-plane $\upsilon_{\mathrm{asym}}(CF_3)$ modes (**Figure 37a** and **c**). The second structure is interpreted in terms of the aromatic moiety of **NHC-2** forming a π-chemisorbed flat-lying state, in line with the strong chemisorption of aromatics on platinum and ruthenium. This structure is characterized by a selectively active out-of-plane $\upsilon_{\mathrm{asym}}(CF_3)$ vibration (**Figure 37b** and **d**). At low temperatures (300-400 K), signal from all three CF_3-related bands is seen indicating the presence of both vertical and flat-lying, or tilted, structures, while at higher temperatures only the vertically oriented NHC is observed. Two prominent bands at ~1329 and ~1184 cm^{-1} show that the vertically oriented NHC is isolated on Pt(111) in the 500-600 K temperature range (**Figure 35a**). A similar set of data (**Figure 36a**) is seen for precursor exposed Ru(0001) where the vertically oriented NHC is isolated at 500 K. In the present study of Gr/metal interfaces, the very strong $\upsilon_{\mathrm{sym}}(C\text{-}CF_3)$ band at ~1329 cm^{-1} allows us to detect NHC formation on the free metal surface following either incomplete graphene layer deposition or oxidation damage to the layer.

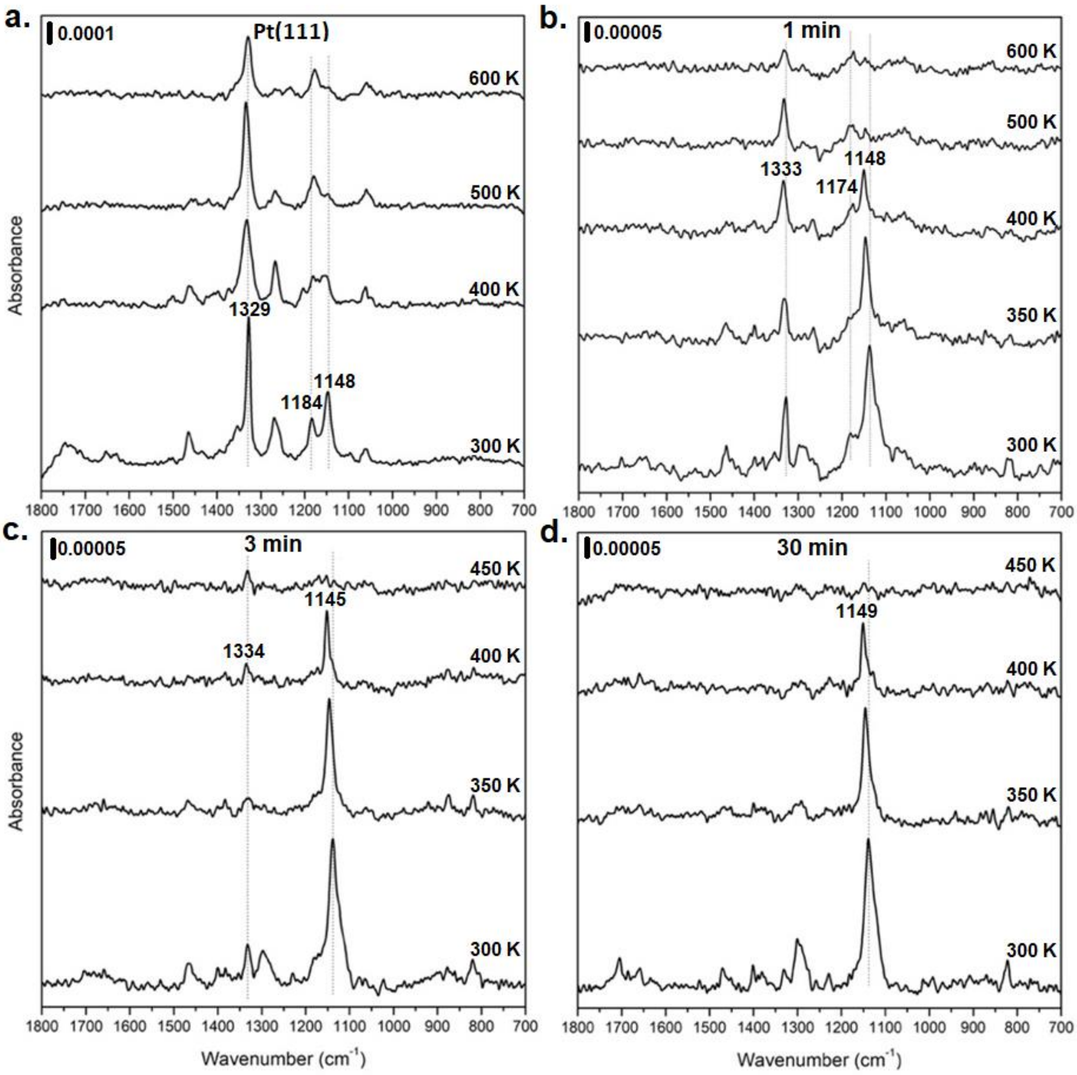

Figure 35 RAIRS spectra of **NHC-2** precursor treated (a) pristine Pt(111) and (b-d) Gr/Pt(111). Graphene was prepared by ethylene CVD for (b) 1 min, (c) 3 min and (d) 30 min at 950 K and 10^{-7} Torr.

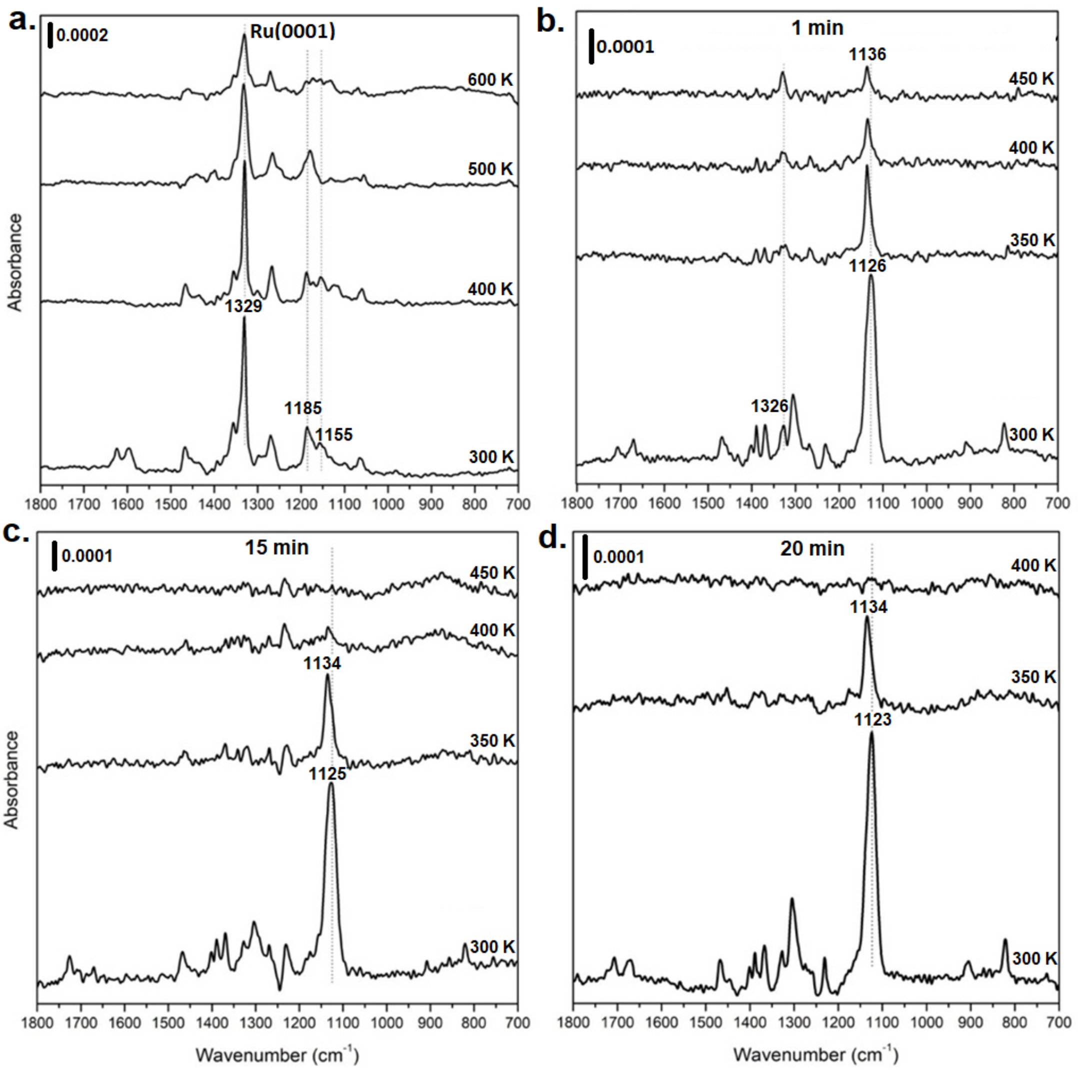

Figure 36 (a) RAIRS spectra of **NHC-2** precursor treated clean Ru(0001) and (b-d) Gr/Ru(0001). Graphene was prepared by CVD at 1000 K in 10^{-7} Torr ethylene for (b) 1 min, (c) 15 min and (d) 20 min.

Next, we show that only the out-of-plane $\upsilon_{asym}(CF_3)$ vibration is detected following exposure of the graphene covered metal surfaces to **NHC-2** precursor. **Figure 35b-d** display data for precursor exposed Gr/Pt(111). The interface prepared by the shortest CVD duration shows a medium intensity $\upsilon_{sym}(C\text{-}CF_3)$ band at 1328 cm^{-1}, revealing the presence of free Pt(111) sites (**Figure 35b**). The signal from the free surface is very weak for interfaces prepared by 3 min CVD (**Figure 35c**) and completely absent for interfaces prepared by 30 min (**Figure 35d**) deposition. By reference to LEEM studies by Harrison *et al.* [43] and Bao *et al.* [42], the latter interface is taken as a system approaching full coverage of graphene. The out-of-plane $\upsilon_{asym}(CF_3)$ band at 1148 cm^{-1} is clearly the dominant feature in **Figure 35b-d**. The completely selective RAIRS activity of this mode relative to the υ_{sym}(C-CF$_3$) and in-plane υ_{asym}(CF$_3$) modes, shows that the benzimidazolium core is close to parallel to the Gr/Pt(111) interface.

Figure 36b-d display data for precursor exposed Gr/Ru(0001). The υ_{sym}(C-CF$_3$) band due to adsorption on the free metal is very weak even for a CVD duration of only 1 min. As observed for Gr/Pt(111), the strong out-of-plane υ_{asym}(CF$_3$) band is also the dominant feature resulting from the interaction of **NHC-2** precursor with Gr/Ru(0001). However, a comparison of spectra acquired on annealing to 350 K shows that the band is red-shifted by ~14 cm^{-1} relative to the frequency observed for Gr/Pt(111). There is a second major difference with respect to the Gr/Pt(111) data in that the out-of-plane υ_{asym}(CF$_3$) signal is detected to 400 K on Gr/Pt(111) and to 350 K on Gr/Ru(0001). Thus, the NHC forms a slightly stronger bond to the Gr/Pt(111) surface.

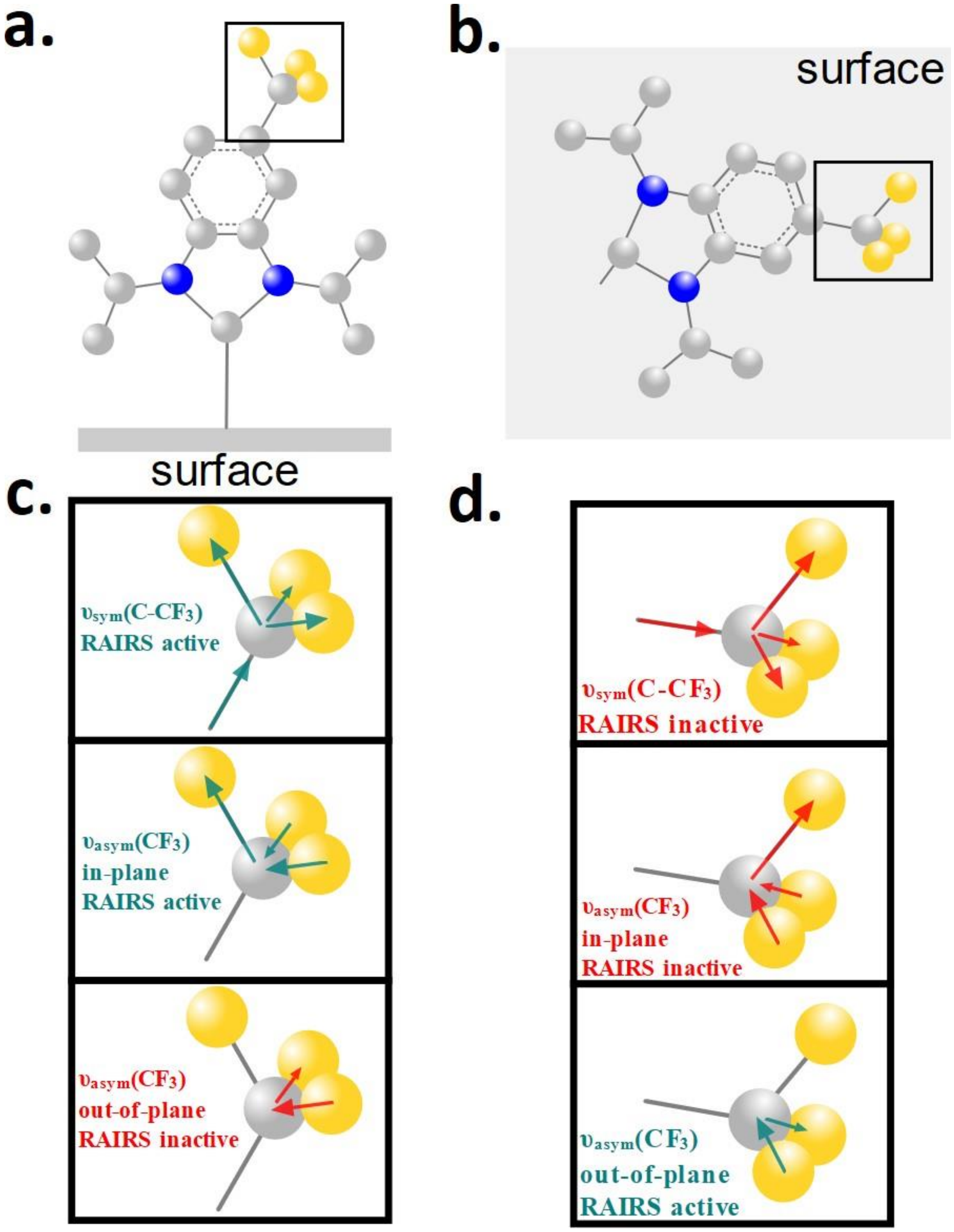

Figure 37 (a) An upright standing (vertical) **NHC-2** on the surface. (b) A flat-lying **NHC-2** on the surface. (c) Schematic illustration of the υ_{sym}(C-CF$_3$), in-plane υ_{asym}(CF$_3$) and out-of-plane υ_{asym}(CF$_3$) modes of the CF$_3$ group in the orientation shown in a black rectangle in (a). (d) Schematic illustration of the υ_{sym}(C-CF$_3$), in-plane υ_{asym}(CF$_3$) and out-of-plane υ_{asym}(CF$_3$) modes of the CF$_3$ group in the orientation shown in a black rectangle in (b). Green arrows signify RAIRS-active modes and red arrows signify RAIRS-inactive modes.

In addition to ethylene, 1-pentene was also used to deposit Gr on the Pt(111) surface (**Figure 38**) by exposure under 10^{-7} Torr at 950 K for 20 min. The RAIRS spectra of grafted **NHC-2** on the 1-pentene prepared graphene layer are similar to those for Gr created by ethylene at 950 K for 20 min. RAIRS spectra in **Figure 38** only display the out-of-plane $\upsilon_{\mathrm{asym}}(\mathrm{CF_3})$ stretching at 350 K, indicating Gr fully covers Pt(111) following 1-pentene CVD. The aromatic CH bending mode at 820 $\mathrm{cm^{-1}}$ is detected at 350 K but there are no evidences of carbonate vibrations from the **NHC-2·H₂CO₃** on full coverage Gr/Pt(111) after 350 K [77]. These results Indicate covalent bonding of **NHC-2** to Gr/Pt(111) and that the grafted **NHC-2** is roughly parallel to the Gr/Pt(111) surface (**Figure 37b**). As a result, the $\upsilon_{\mathrm{sym}}(\mathrm{C\text{-}CF_3})$ and in-plane $\upsilon_{\mathrm{asym}}(\mathrm{CF_3})$ vibrations are roughly parallel to the surface, while the out-of-plane $\upsilon_{\mathrm{asym}}(\mathrm{CF_3})$ vibration produces a strong transition dipole moment perpendicular to the surface.

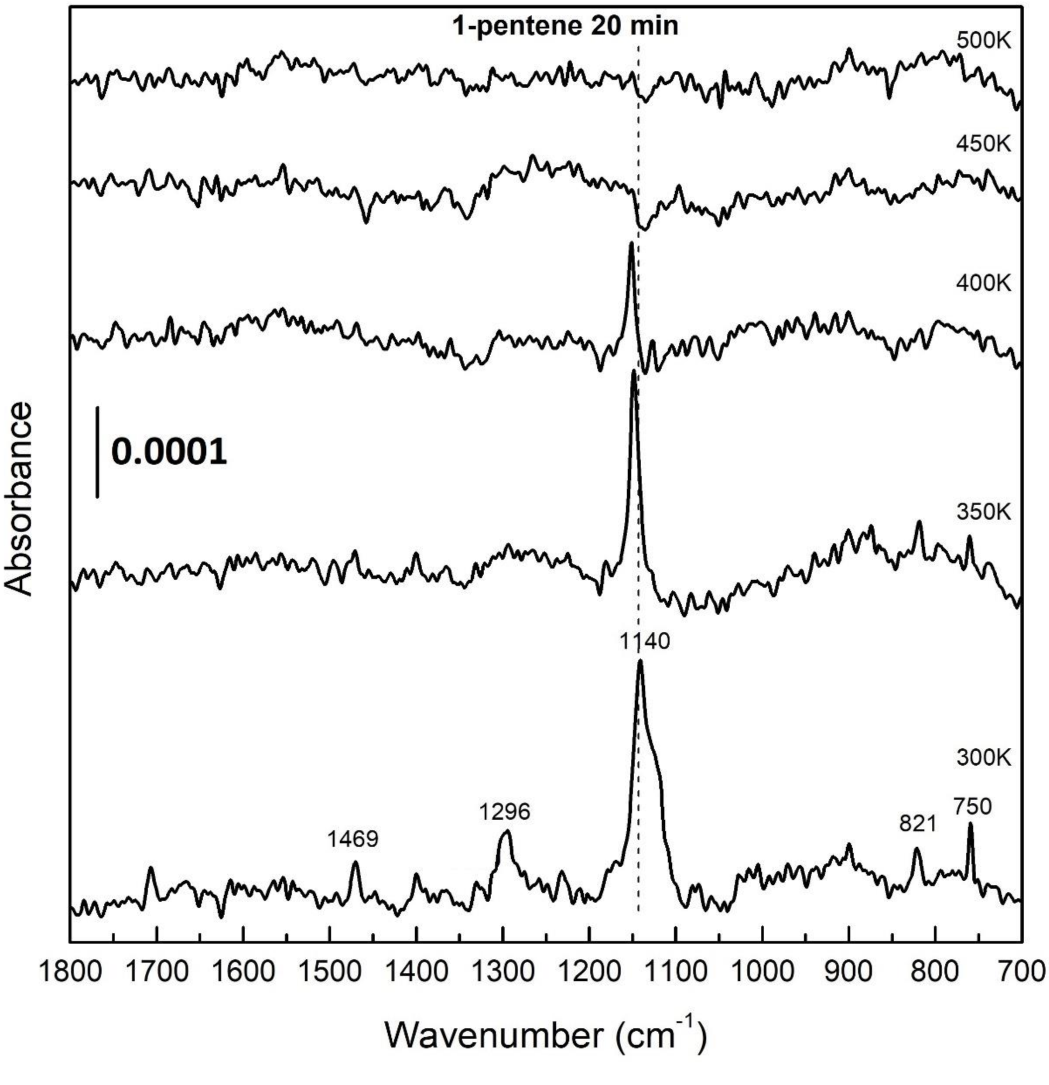

Figure 38 RAIRS spectra of **NHC-2** on full coverage Gr/Pt(111) prepared under 10^{-7} Torr 1-pentene at 950 K for 20 min.

Using the data presented in **Figure 35** and **36**, we next consider whether exposure of supported graphene to the NHC precursor leads to the formation of a covalently grafted NHC or simply to a physically adsorbed structure. The observation that the benzimidazolium core is close to parallel to the surface plane on Gr/Pt(111) and Gr/Ru(0001) is most readily interpreted in terms of a physically adsorbed state stabilized by π-π stacking interaction [159,160]. Here, it is reasonable to assume that the graphene layer prevents a π-chemisorption interaction with the surface. However, four observations point to the formation of a covalently bonded NHC-graphene structure: (i) Due to the bulky isopropyl wingtip groups, it is highly unlikely that a physisorbed state would possess the structural homogeneity required to produce the observed completely selective RAIRS activity of the out-of-plane $\upsilon_{asym}(CF_3)$ mode. A physisorbed state would also display some activity for the very strong $\upsilon_{sym}(C\text{-}CF_3)$ and relatively strong in-plane $\upsilon_{asym}(CF_3)$ bands. (ii) As discussed below, the interaction of the precursor with the studied systems is sensitive to the graphene preparation methods, to the metal substrate used, and to oxygen intercalation. Both frequency shifts and differences in thermal stability are observed. These phenomena are signatures of chemisorption. (iii) As discussed next, the observed thermal stability on Gr/Pt(111) is similar to that for aryl groups grafted to graphite [161] or graphene [158] using the diazonium method. (iv) The reported adsorption energy for benzene on Gr/Ru(0001) is higher by ~4 kJ/mol than the value for Gr/Pt(111) [162,163]. In contrast, the NHC displays higher thermal stability on Gr/Pt(111). This observation indicates that NHC/Gr adsorption is not simply due to a π-π interaction. On the basis of these points, we conclude that exposure to the precursor leads to the formation of a covalently bonded NHC on Gr/Pt(111) and Gr/Ru(0001).

We next consider the thermal stability of the covalently grafted carbene. For Gr/Pt(111) prepared by ethylene CVD at 950 K, the out-of-plane $\upsilon_{asym}(CF_3)$ band disappears (**Figure 35b-d**) between 400 and 450 K. For Gr/Ru(0001), the band disappears on annealing from 350 to 400 K (**Figure 36c** and **d**). The moderate degree of thermal stability on Gr/Pt(111) is similar to that reported by De Feyter and co-workers [161] for diazonium generated aryl groups on highly oriented pyrolytic graphite (HOPG). They determined, using a combination of chemisorption-specific STM and Raman spectroscopy measurements, that the onset for cleavage of the covalent bond to the aryl groups occurs at temperatures no higher than 433 K and is mostly complete by 473 K. Similarly, Hirsch *et al* [158]. observed the removal of aryl groups from graphene at ~473 K and even lower temperatures. Hence, we conclude that NHC grafting leads to weak C-C bond formation as also observed using the diazonium method. We hypothesize that a combination of weak covalent C-C bonding and strong van der Waals interaction results in a roughly parallel orientation of the **NHC-2** structure with respect to the surface, resulting in selective RAIRS activity of the out-of-plane $\upsilon_{asym}(CF_3)$ band.

Next, we relate the slightly higher thermal stability of the NHC on Gr/Pt(111) to modification of the electronic properties of the graphene layers by the substrates. The quasi-freestanding Gr/Pt(111) layer is strongly p-doped whereas the Gr/Ru(0001) layer is strongly n-doped. [164] The higher thermal stability on Gr/Pt(111) is then attributed to the nucleophilic, sigma-donor, character of the benzimidazolium carbene. This interpretation finds support in the converse behavior seen for nitrene grafting on Gr/Cu(111) and Gr/Ni(111) reported by Yan *et al.* [150], The authors pointed out that the nitrene is highly electron deficient species and it preferentially binds to the more strongly n-doped Gr/Ni(111) system. The curvature, and hence strain, intrinsic to wrinkles increases the reactivity of graphene [165]. Gr/Pt(111) presents wrinkles [42] and this may be an additional contributing factor to the higher thermal stability of the NHC.

The spectra in **Figure 39** are used to consider steps in the transformation of **NHC-2** precursor to grafted NHC on the Gr/metal interfaces as compared to the process on pristine metal surfaces. Adsorption of the precursor on the clean metals at 300 K (**Figure 39a**) results in rich spectra that simultaneously display the υ_{sym}(C-CF_3), in-plane υ_{asym}(CF_3) and out-of-plane υ_{asym}(CF_3) bands. These bands are still present at 350 K and are attributed to a mixture of vertical and flat-lying states. As described above, the flat-lying state involves strong π-chemisorption of the aromatic moiety on the metal surface and the vertical state forms a carbenic C-metal bond. The corresponding spectra seen for the Gr/metal interfaces are much simpler in that they show a greatly dominant out-of-plane υ_{asym}(CF_3) band even at 300 K. In addition, there is structure in the 1500-1200 cm^{-1} region that is very similar to that NHC precursor exposed on Pt(111) at 250-280 K (**Figure 27**). The latter structure was assigned to a flat-lying adsorbed species formed after loss of the carbonate group. Following this interpretation, the spectra for Gr/Pt(111) and Gr/Ru(0001) in **Figure 39** show that the counterion is already removed at 300 K and that only the grafted NHC species remains at 350 K. These results show that a graphene layer does not passivate the system against precursor salt decomposition but rather it catalyzes the conversion. This result is fully consistent with a recent report by Eigler *et al.* [166], showing the non-covalent functionalization of graphene on silicon using compounds containing benzimidazolium moieties. They found that electron transfer from graphene reduced the N-heterocyclic salts resulting in the loss of the counterion.

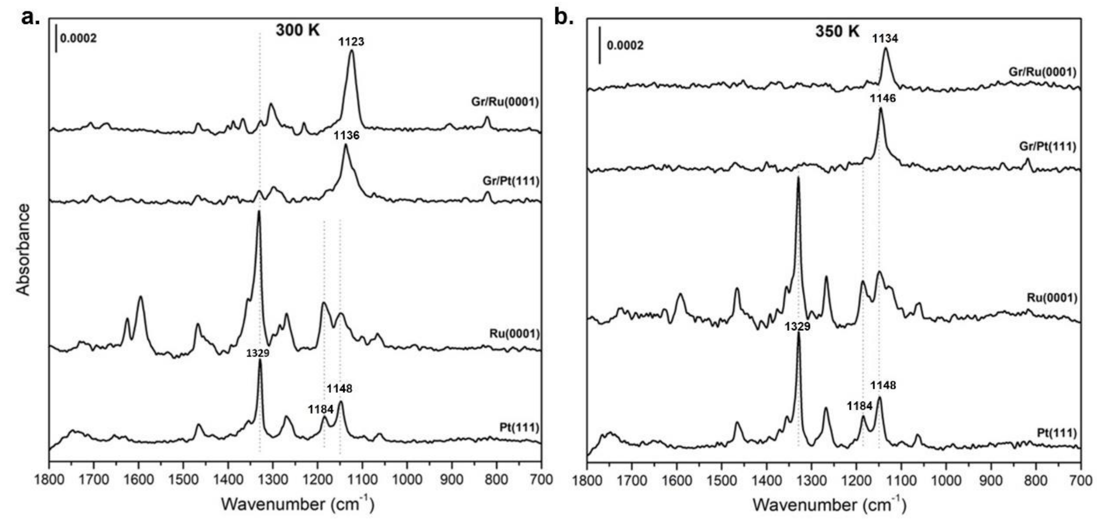

Figure 39 Comparison of RAIRS spectra of **NHC-2** precursor exposed pristine metal and supported graphene surfaces.

The influence of defects on the thermal stability of grafted NHC was explored by three methods. First, 1-pentene was used as a CVD carbon source to prepare low-defect graphene on Pt(111) [167,168]. The resulting system yielded essentially the same spectra (**Figure 38**) as those for full coverage graphene prepared at high temperatures using ethylene (**Figure 39**). Second, Gr/Pt(111) was prepared by annealing in a background of 1 x 10^{-7} Torr ethylene from 300 K to 800-950 K. In the latter method, ethylidyne is first formed, followed by dehydrogenation to carbidic carbon in the 450-700 K range, and eventually graphene formation above 800 K [19]. In these experiments, the NHC, as detected by the out-of-plane $\upsilon_{asym}(CF_3)$ band, is removed between 450 and 500 K (**Figure 40**). The higher stability, relative to Gr/Pt(111) prepared by high temperature CVD, is attributed to grafting to edge sites of carbon clusters or nanoislands [169]. Third, as described below, the influence of defects was explored by deliberately damaging the Gr/Pt(111) layer by oxidation.

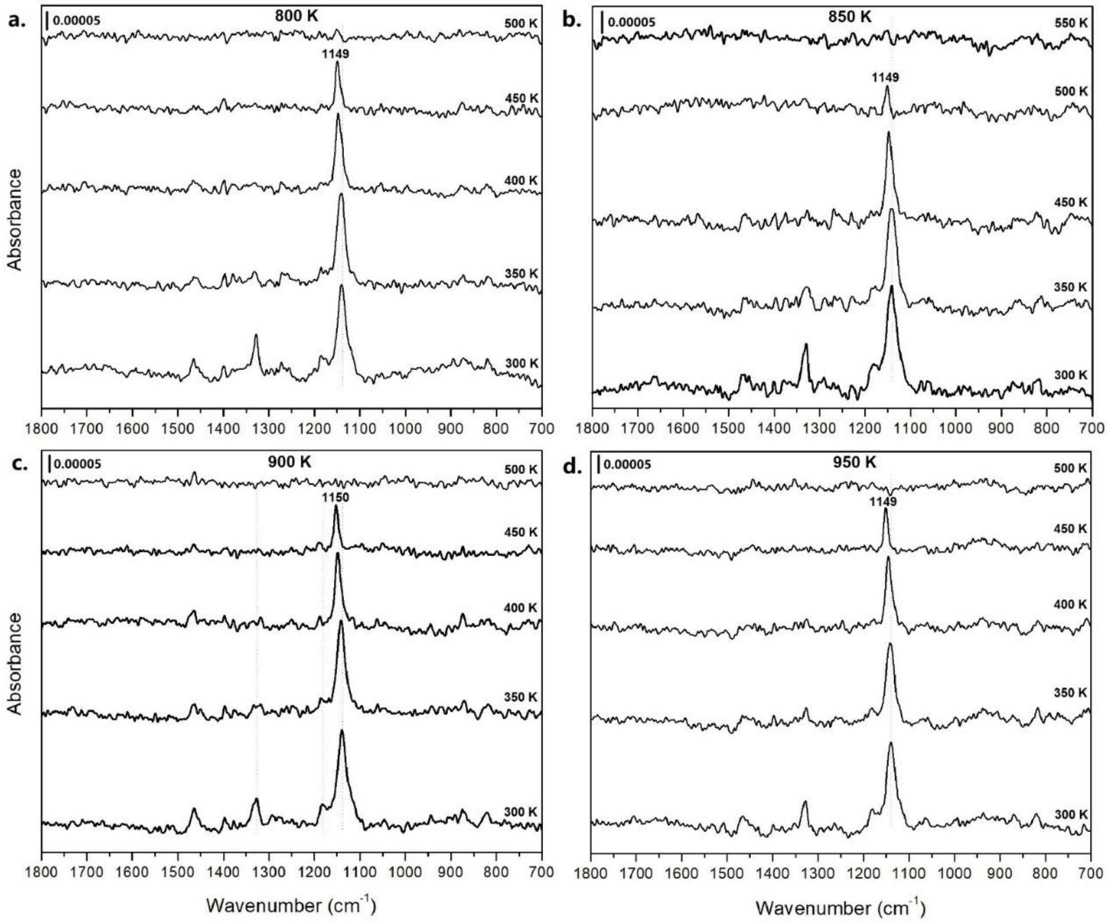

Figure 40 RAIRS spectra of the interaction of **NHC-2** precursor with Pt(111) surfaces that were modified by annealing in 10^{-7} Torr ethylene to the temperatures shown at the top of the panels.

In order to understand the different activities between flat Gr, Gr edges and Gr wrinkles, Bao and co-workers reported the oxidation process for different O_2 exposure times (653 K, 5 × 10^{-7} Torr) [42]. As shown in **Figure 41**, oxidation etching sites preferentially occurs at edge and wrinkle sites after 100 s O_2 exposure, indicating that these sites are more active than sites on flat Gr. Dispersive interactions account for bonding between Gr and Pt(111) resulting in a normally planar layer at a distance of ~3 Å from the surface (**Figure 42 and Figure 5**) [169] However, sp^2-hybridized Gr is distorted to sp^3-hybridized Gr at edges and wrinkles [169,170] and activity is enhanced at these sites. We cannot exclude the possibility that **NHC-2** ligands preferentially form covalent bonds at wrinkle and edge sites.

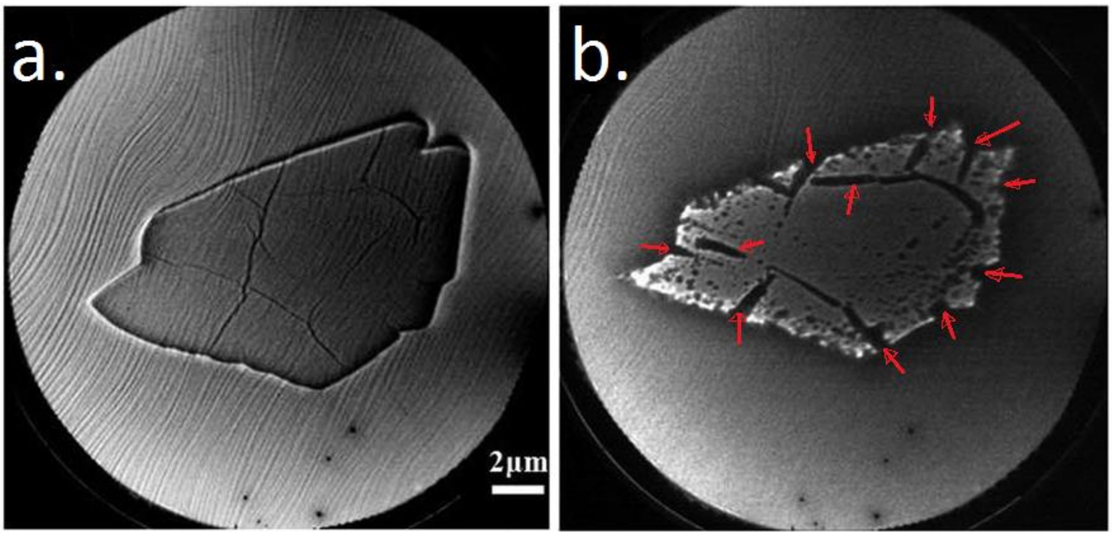

Figure 41 (a) LEEM image of a Gr island, including Gr edges, Gr wrinkles and flat Gr; (b) LEEM image of Gr oxidation at 653 K, under 5 × 10^{-7} Torr O_2 exposure for 100 s. Permission from Ref. [42], copyright 2013 American Chemical Society.

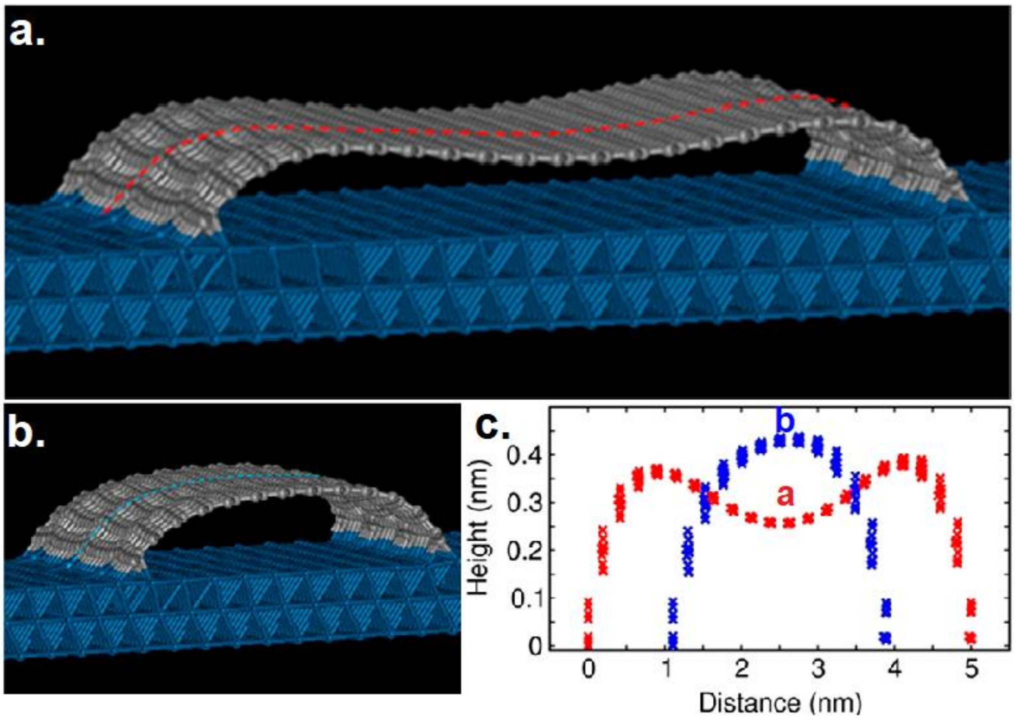

Figure 42 (a, b) DFT-optimized structure of graphene islands on Pt(111), C atoms at Gr edges form covalent bonds with Pt(111), Pt-C bond lengths are about 1 Å. (c) Red: height profile across the island shown in (a); blue, height profile across the island shown in (b). Permission from Ref. [169], copyright 2017 American Chemical Society.

As shown in **Figure 43**, different ethylene (10^{-7} Torr) exposure times and temperatures (950 K and 1000 K) were explored to create Gr on Pt(111). Subsequent to graphene deposition, the Gr/Pt(111) samples were cooled down to 300 K (**Figure 43a**) or 400 K (**Figure 43b**) before dosing **NHC-2** and acquiring RAIRS spectra. No carbonate features were observed on exposure to the **NHC-2** precursor at 400 K. Partial coverage Gr on Pt(111) is created at 950 K under ethylene exposure for 1 min and 3 min as shown by the υ_{sym}(C-CF$_3$) and in-plane υ_{asym}(CF$_3$) vibrations characteristic of NHC-2 adsorption on the pristine surface. In contrast, ethylene exposure at 950 K for 20 min or 1000 K for 5 min is enough to create full coverage Gr/Pt(111), as shown by the absence of the υ_{sym}(C-CF$_3$) and in-plane υ_{asym}(CF$_3$) bands.

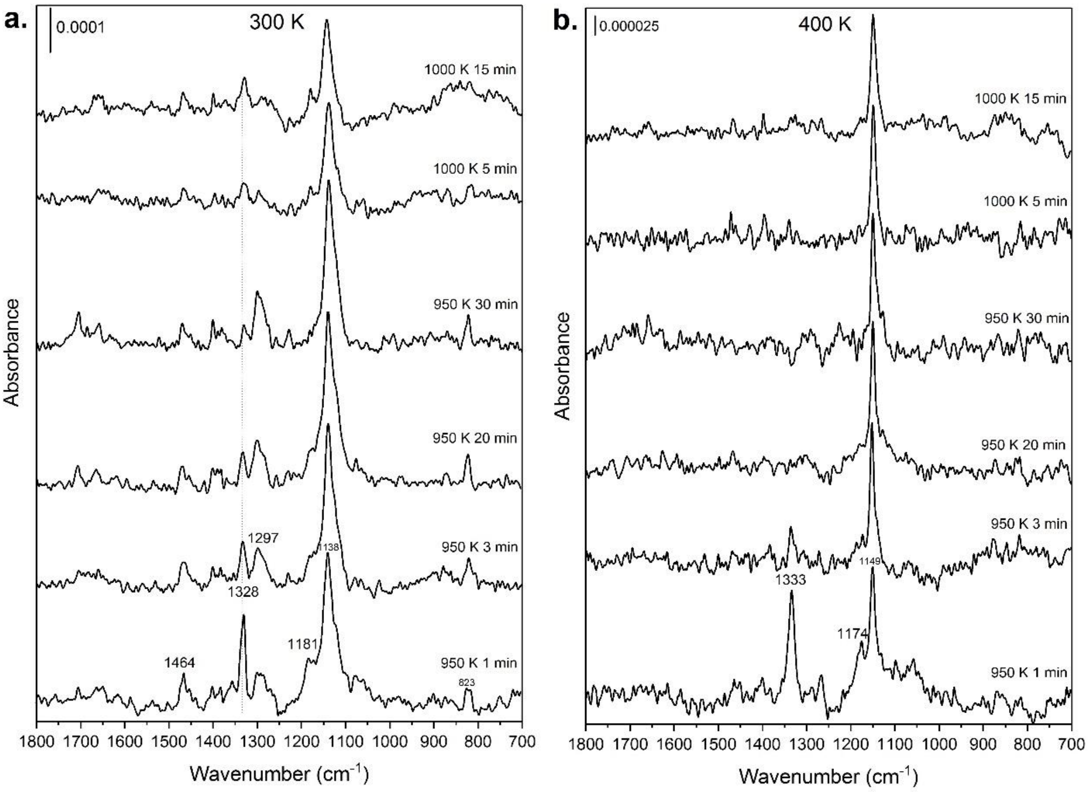

Figure 43 RAIRS spectra for **NHC-2** adsorption on graphene layers prepared by ethylene CVD for the indicated times and temperatures under 10^{-7} Torr. The RAIRS spectra were acquired after **NHC-2** exposure at (a) 300 K and (b) 400 K.

As described in Chapter 1 in relation to **Figures 6-8**, the Moiré supercell for Gr/Ru(0001) is composed of 25 × 25 Gr unit cells on 23 × 23 metal unit cells [171–173]. Within the supercell, the distance between Gr and Ru varies between 2.2 to 3.7 Å [171,174] giving rise to *top*, *fcc* and *hcp* sites [174–176] due to the different stacking modes of Gr on Ru(0001). In the STM image shown in **Figure 44**, the brightest region is due to *top* sites, the intermediate bright region is due to *fcc* sites and the darkest region is due to *hcp* sites.

Graphene at the *top* site is relatively far away from Ru, and the carbon atoms have no chemical interaction with the metal. In contrast, Gr at *fcc* and *hcp* sites is relatively close to Ru and forms a weak covalent bond to the surface [174]. Dohnálek and co-workers found that atomic oxygen binds preferentially on *fcc* and *hcp* sites rather than on *top* sites. This observation illustrates that perturbed Gr at *hcp* and *fcc* sites is more reactive than quasi-free graphene *top* sites [176].

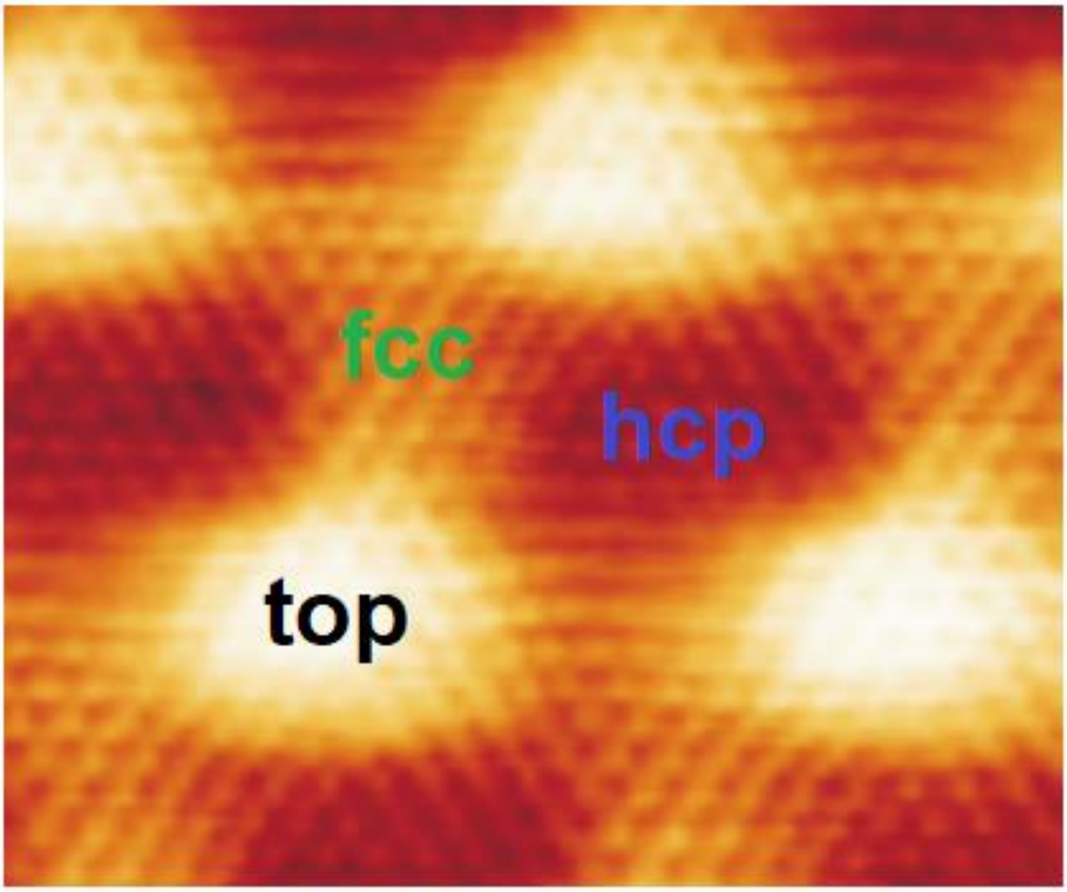

Figure 44 STM image of the Moiré pattern structure. There are three regions of Gr moiré pattern. The brightest region is named *top* site, the lighter region is named *fcc* site and the darkest region is named *hcp* site. Permission from Ref. [177] Copyright 2007 American Physical Society.

3.4 NHC-2 on Gr/O/Ru(0001)

A series of experiments were performed on the Gr/Ru(0001) system in order to probe the sensitivity **NHC-2** precursor adsorption to perturbation of the graphene layer by intercalation [40,43,164,178–185] to form Gr/O/Ru(0001) and by oxidation damage to form graphene-free regions. Intercalation experiments in ultrahigh vacuum studies of Gr/Ru(0001) are typically carried out between 450 and 600 K whereas oxidation etching experiments requires temperatures above 600 K. The work of a number of groups shows that approximately 100-400 L O_2 exposure at 550-600 K leads to full intercalation [40,184–186]. Ulstrup *et al.* [180] found that O_2 intercalates below Gr/Ru(0001) at 420 K but that high exposures (~5 x 10^6 L) at 450 K are required to achieve full intercalation resulting in a completely decoupled Gr layer. (1L is defined as 1 x 10^{-6} Torr·sec). Work by Kahng *et al.* [182] shows that exposure to 1 x 10^{-7} Torr O_2 at 650 K leads to both intercalation and etching, revealing coexisting Gr/Ru(0001) Moiré, intercalated Gr/O/Ru(0001) and O_{ads}/Ru(0001) regions in STM images.

Figure 45 shows RAIRS spectra recorded after a range of O_2 treatments of Gr/Ru(0001). Oxygen induced changes are referenced to NHC/Gr/Ru(0001) spectra where the out-of-plane $\upsilon_{asym}(CF_3)$ band appears at 1123 to 1134 cm^{-1} up to ~400 K(**Figure 36d**). High exposures to oxygen at 400 K leads to a shift in the out-of-plane $\upsilon_{asym}(CF_3)$ band to 1138-1145 cm^{-1} and an increase in the thermal stability, with signal still observed at 450 K. A similar result is seen for lower oxygen exposures at 450 K and 525 K, with out-of-plane $\upsilon_{asym}(CF_3)$ frequencies in the 1133 to 1139 cm^{-1} range and signal still detected at 500 K. Very high oxygen exposure at 450 K shifts the band to 1148 cm^{-1} and also results in the emergence of a weak $\upsilon_{sym}(C\text{-}CF_3)$ band at 1330 cm^{-1} due to adsorption on graphene-free sites, indicating minor oxidation damage to the graphene layer. Major damage occurs under oxidation at 600 K, as revealed by the detection of the intense $\upsilon_{sym}(C\text{-}CF_3)$ and in-plane $\upsilon_{asym}(CF_3)$ bands at 1339 and 1185 cm^{-1} due to adsorption on graphene-free regions. In addition, the out-of-plane $\upsilon_{asym}(CF_3)$ band (at ~1147 cm^{-1}) is relatively strong at 500 K, showing that NHC grafted to the remaining holey graphene has high thermal stability.

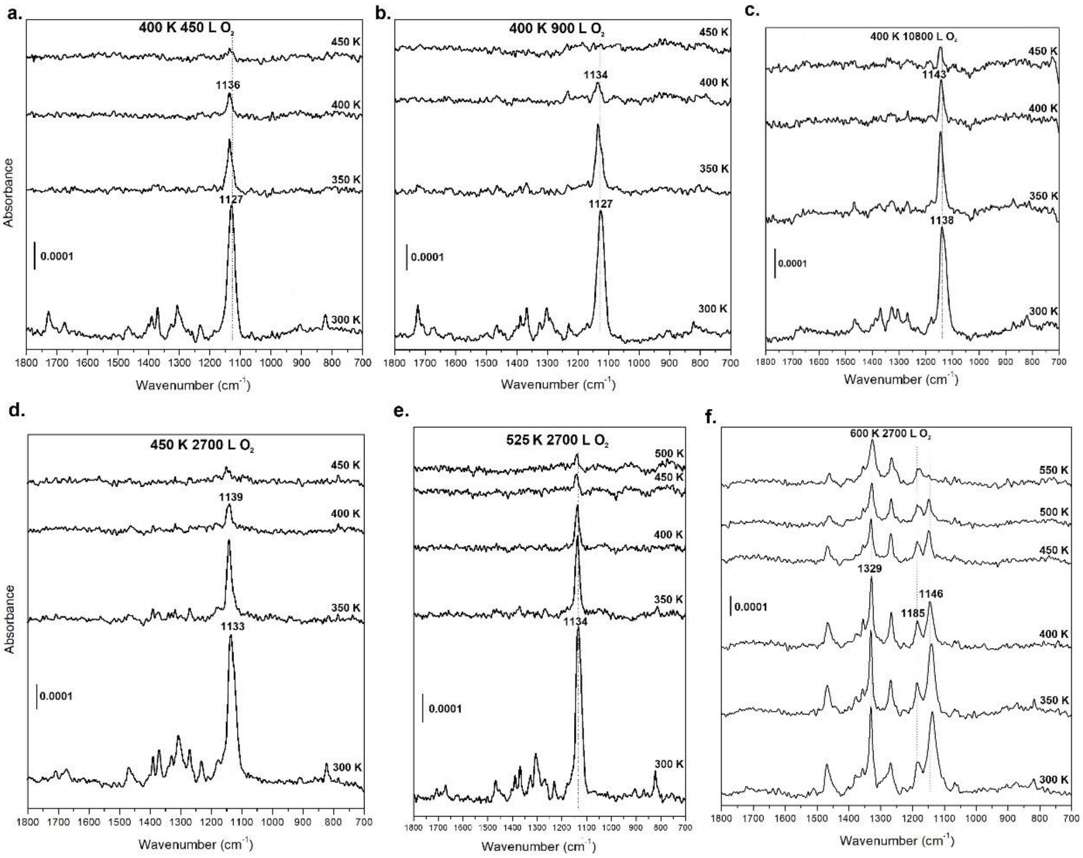

Figure 45 (a-c) RAIRS spectra probing the interaction of **NHC-2** precursor with O_2 treated Gr/Ru(0001) surfaces. The oxygen exposure conditions were (a) 5 min, 1.5 × 10^{-6} Torr, 400 K; (b) 10 min, 1.5 × 10^{-6} Torr, 400 K; (c) 60 min, 3 × 10^{-6} Torr, 400 K; (d) 30 min, 1.5 × 10^{-6} Torr, 450 K; (e) 30 min, 1.5 × 10^{-6} Torr, 525 K; (f) 30 min, 1.5 × 10^{-6} Torr, 600 K.

The interaction of the NHC with Gr/O/Ru(0001) differs from that with Gr/Ru(0001) in two significant respects. First, the out-of-plane $\upsilon_{asym}(CF_3)$ band in the Gr/O/Ru(0001) spectra is shifted to higher frequencies. Second, the band is readily detected at higher temperatures. Thus, in terms of the adsorption and thermal evolution of the NHC precursor, oxygen intercalation transforms the n-doped Gr/Ru(0001) layer to a system displaying properties similar to Gr/Pt(111). This observation is consistent with the observation that oxygen intercalation decouples Gr from Ru(0001) [40,164,178,185–187] bringing it closer to the Gr/Pt(111) quasi-freestanding description. As for Gr/Pt(111), the decoupled Gr/O/Ru(0001) layer is strongly p-doped and presents wrinkles [40].

Table 2 Assignment of vibrational frequencies (cm^{-1}) of adsorbed **NHC-2**.

Assignment	**NHC-2** on Pt(111)	**NHC-2** on Ru(0001)	**NHC-2** on Gr/Pt(111)[a]	**NHC-2** on Gr/Ru(0001)[b]	**NHC-2** on Gr/O/Ru(0001)[c]
υ_{sym}(C-CF$_3$)	1329	1329			1330
in-plane υ_{asym}(CF$_3$)	1184	1185			1188
out-of-plane υ_{asym}(CF$_3$)	1148	1155	1149	1134	1148

[a] out-of-plane υ_{asym}(CF$_3$) of **NHC-2** on full coverage Gr/Pt(111) at 400 K; [b] out-of-plane υ_{asym}(CF$_3$) of **NHC-2** on full coverage Gr/Ru(0001) at 350 K; [c] CF$_3$-related frequencies of **NHC-2** on full coverage (~5 x 10^6 L, 450 K O$_2$ exposure) Gr/O/Ru(0001) at 400 K.

3.5 Summary and Conclusions

We have demonstrated that it is possible to covalently modify graphene monolayers on Pt(111) and Ru(0001) using an N-heterocyclic carbene. The grafted NHC groups display thermal stability similar to that reported for aryl groups on graphite and graphene, showing that a weak C-C bond is formed. The overall interaction with the surface includes a strong van der Waals component which bends the **NHC-2** moiety so that is roughly parallel to the graphene layer. The interaction of the NHC with Gr/Pt(111) is stronger than with Gr/Ru(0001). This difference mainly is attributed to the p-doped and n-doped character of the respective systems coupled with the electron-donor character of the NHC. The stronger interaction with Gr/Pt(111) is also, in part, due to strain intrinsic to the highly curved wrinkle structures characteristic CVD graphene on Pt(111). Intercalation of oxygen between graphene and Ru(0001) leads to NHC bonding similar to that for Gr/Pt(111) consistent with the removal of the strong Gr/Ru interaction to form a quasi-freestanding p-doped and wrinkled layer. N-heterocyclic carbenes form a very diverse family of compounds and thus offer multiple avenues to functionalize and modify graphene for specific applications. From a characterization perspective, NHCs as probed by vibrational spectroscopy are clearly very sensitive probes of graphene. The present study shows that both theoretical and scanning local probe studies of NHCs on graphene are warranted.

Chapter 4 Surface Modification of 2D-Mo_2C

4.1 Introduction

As described in General Introduction, ultrathin molybdenum carbide crystals can be grown on copper substrates using a chemical vapor deposition (CVD) method. The method, first reported by Ren *et al.*, depends on the diffusion of molybdenum atoms through molten copper and reaction with a carbon source such as methane. This high temperature method produces 2D Mo_2C crystallites on solid copper. We refer to the materials as 2D-Mo_2C/Cu. Very little is known about the surface chemistry of these materials. This Chapter describes experiments aimed at the surface analysis of 2D-Mo_2C/Cu and also functionalization and surface reactivity studies.

4.2 As-Received 2D-Mo_2C/Cu Samples

The 2D-Mo_2C/Cu samples used in our study were provided by Ren's group from the Shenyang National Laboratory for Material Science, Institute of Metal Research, Chinese Academy of Sciences. A photograph of a typical sample (**Figure 46a)** shows that the Cu substrate is largely covered with 2D-Mo_2C. **Figure 46b** presents an optical microscopy image published by Ren *et al.* [71]. The sample displays different regular crystallite shapes, including triangular, rectangular, hexagonal and octagonal forms. The corresponding atomic force microscopy (AFM) images (for example, **Figure 46c**) from Ren's group [71] shows that the thickness of the metal carbide is in the 6-11 nm range. As a result of three factors, the as-received samples are likely to be more complex than simply 2D-Mo_2C/Cu. First, the CVD preparation method can result in the formation of a graphene layer, since the carbide is synthesized at the melting point of copper (~1090 ℃) under a methane environment, as illustrated in **Figure 46d**. [192]. The formation of a graphene layer is not necessarily a negative phenomenon as it transforms the carbide into a hybrid material that might have desired properties such as high chemical stability. Second, exposure to air leads to oxidation and molybdenum carbides are known to readily form oxycarbides. This is also not necessarily a negative phenomenon since oxycarbides are active phases of metal carbide catalysts. Third, exposure to the ambient always leads to hydrocarbon contamination of surfaces. This is a negative phenomenon in our studies in that it hides the surface without conferring any useful new properties. Hence, the first step in our study was to explore methods to clean, prepare and characterize the samples prior to chemisorption studies.

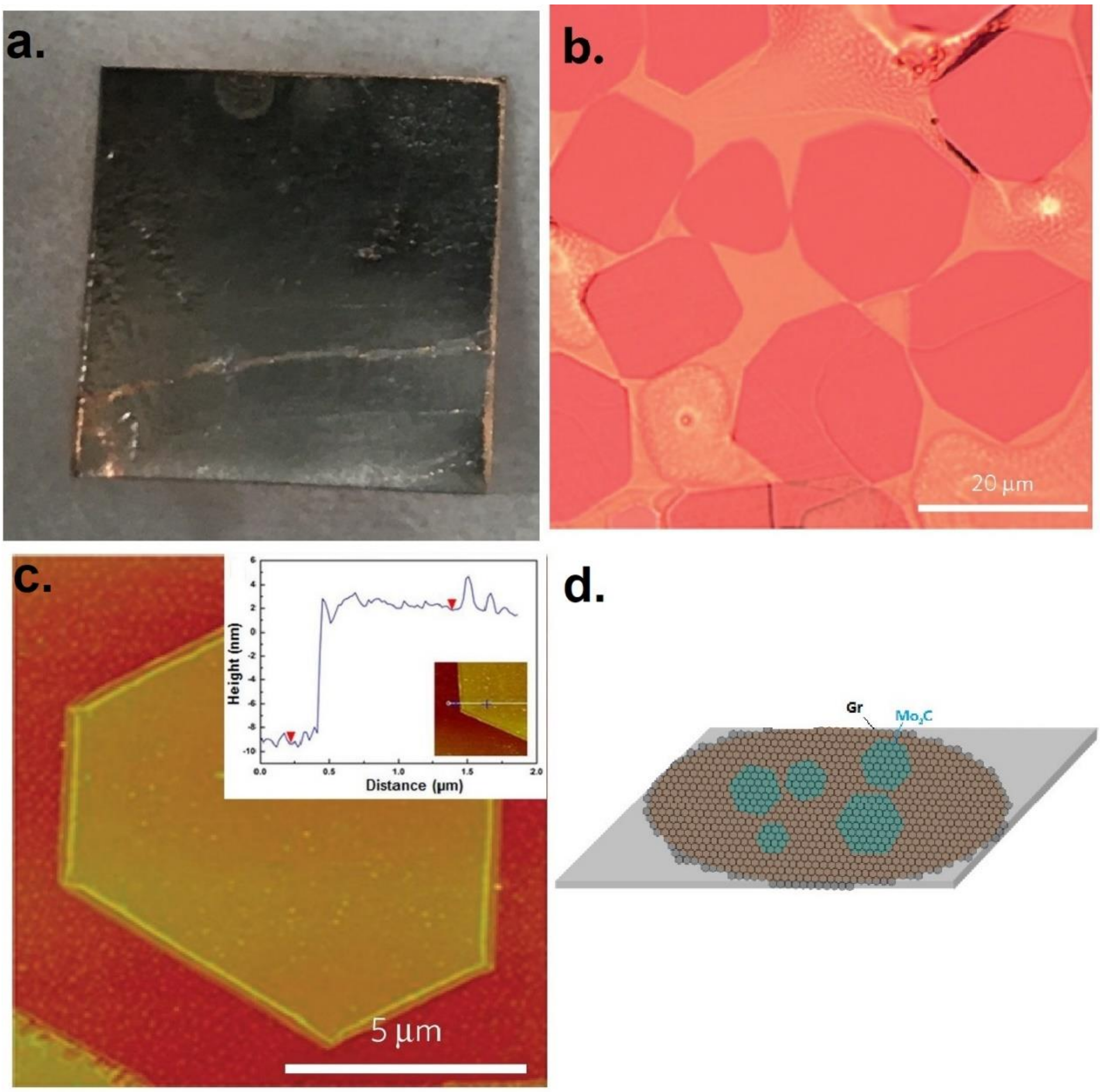

Figure 46 (a) Photograph of a 2D-Mo$_2$C/Cu sample. (b) Typical optical microscopy image of a 2D-Mo$_2$C/Cu sample. Reproduced with permission from Ref. [71], copyright 2015 Macmillan Publishers Limited. (c) AFM image of a hexagonal crystal of 2D-Mo$_2$C on copper. The measured thickness of the crystal is about 8.2 nm [71]. Reproduced with permission from Ref. [71], copyright 2015 Macmillan Publishers Limited. (d) Illustration of the creation of a graphene layer over 2D-Mo$_2$C/Cu during CVD synthesis [188].

The cleaning and preparation of 2D-Mo$_2$C samples poses a considerable challenge because the samples contain so little Mo$_2$C material. Gentle cleaning is required so as not to remove the metal carbide. Thus argon ion sputtering such as used to clean the Pt(111) and Ru(0001) should not be the method of first choice. Furthermore, sputtering causes defect formation and can change the composition of carbides though preferential removal of one the elements. These changes can be repaired in bulk molybdenum carbide samples by heating to very high temperatures. However, annealing to very high temperatures might transform the two-dimensional crystals into 3D particles thereby losing the key characteristic of 2D-Mo_2C/Cu. Nevertheless, since the 2D-Mo_2C/Cu samples were synthesized at the melting point of copper under a CH_4 environment there is a possibility that Mo_2C remains in a 2D state in our experiments even at very high temperatures. Hence, we explored annealing treatments. As an alternative to sputter cleaning, we explored treatment of the samples using a flux of atomic hydrogen generated by a hydrogen cracker. The compositional changes induced by various pretreatments of the sample were monitored by X-ray photoelectron spectroscopy (XPS) measurements.

4.3 Pretreatment of the 2D-Mo_2C/Cu Sample

4.3.1 Annealing in UHV

Normally, annealing is used to remove oxide contamination from carbides under UHV conditions [189]. The oxygen is removed through desorption of CO or CO_2. **Figure 47** shows XPS spectra acquired after relatively low temperature annealing (up to 700 K). The oxygen atomic percentage (O at%) among O, C, Cu and Mo atoms is decreased by only ~20 % on annealing to 700 K.

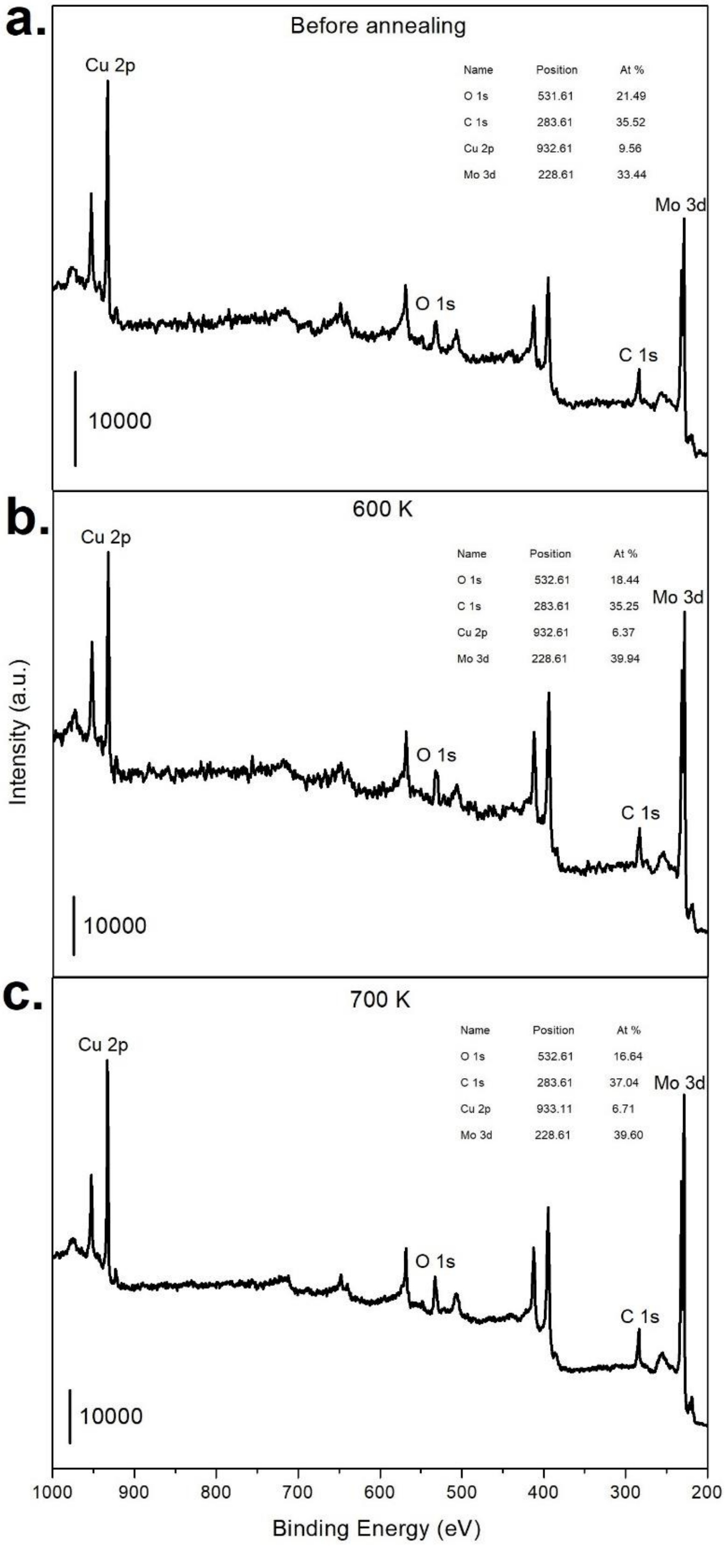

Name	Position	At %
O 1s	531.61	21.49
C 1s	283.61	35.52
Cu 2p	932.61	9.56
Mo 3d	228.61	33.44

Name	Position	At %
O 1s	532.61	18.44
C 1s	283.61	35.25
Cu 2p	932.61	6.37
Mo 3d	228.61	39.94

Name	Position	At %
O 1s	532.61	16.64
C 1s	283.61	37.04
Cu 2p	933.11	6.71
Mo 3d	228.61	39.60

Figure 47 Survey scan XPS spectra for relatively low temperature annealing of 2D-Mo_2C/Cu samples. (a) Spectrum of a high coverage area 2D-Mo_2C/Cu sample prior to anneal. (b) 600 K, 1h annealing. (c) 700 K, 1h annealing.

High temperature annealing was then explored. Short anneal times were used to minimize shape-change of the 2D system (**Figure 48**). However, while the oxygen content is reduced by the annealing procedures, significant changes also occur in the Cu, Mo and C atomic percentages. These changes show that simply annealing the sample is not a controlled method to clean it non-destructively.

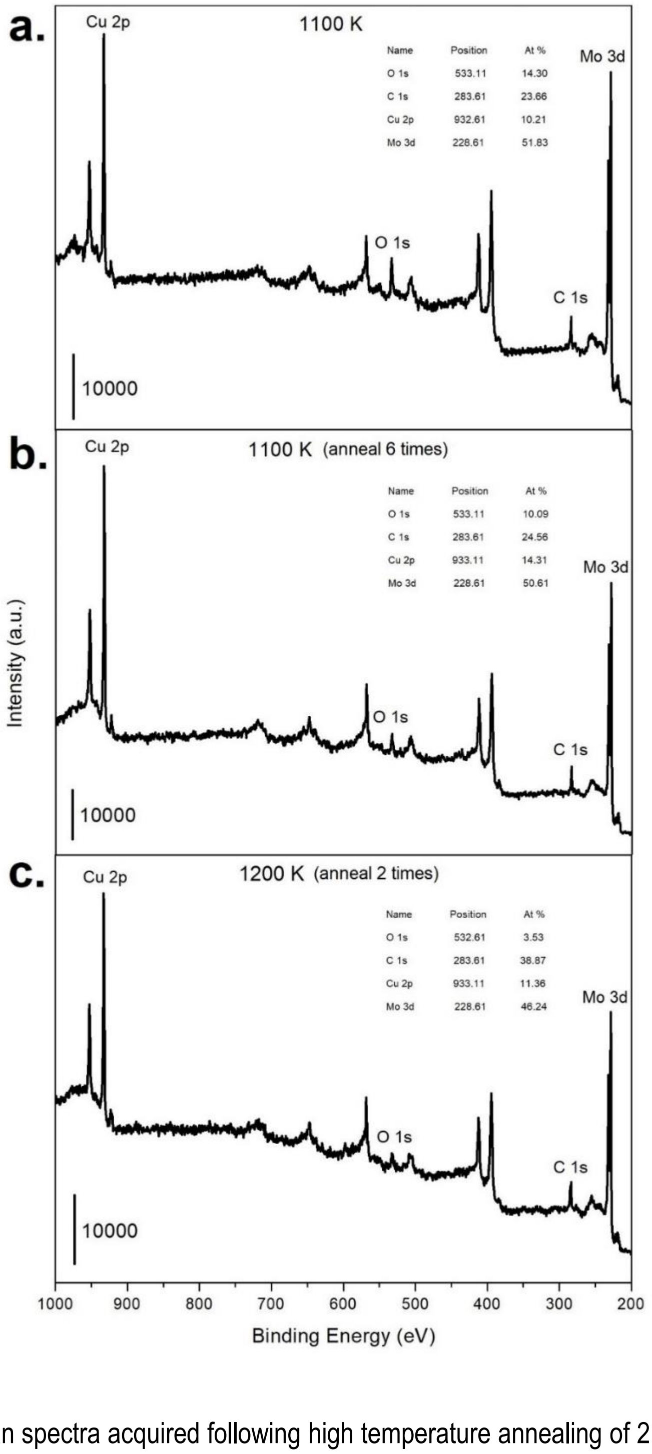

Name	Position	At %
O 1s	533.11	14.30
C 1s	283.61	23.66
Cu 2p	932.61	10.21
Mo 3d	228.61	51.83

Name	Position	At %
O 1s	533.11	10.09
C 1s	283.61	24.56
Cu 2p	933.11	14.31
Mo 3d	228.61	50.61

Name	Position	At %
O 1s	532.61	3.53
C 1s	283.61	38.87
Cu 2p	933.11	11.36
Mo 3d	228.61	46.24

Figure 48 Survey scan spectra acquired following high temperature annealing of 2D-Mo_2C/Cu. (a) 1100 K, 10 s annealing. (b) 1100 K, 10 s annealing repeated 6 times. (c) 1200 K, 10 s annealing repeated 2 times.

4.3.2 Treatment of 2D-Mo_2C/Cu with Atomic Hydrogen

As an alternative to sputter cleaning we explored treatment of the samples using a flux of atomic hydrogen generated by a hydrogen cracker. As described next, compositional changes induced by exposure to atomic hydrogen were monitored by XPS measurements.

Figure 49 shows XPS survey scan spectra acquired following atomic hydrogen cleaning performed at 200 K, 300 K, 400 K, and 500 K, respectively. There are no major difference following treatments at 200 K and 300 K. However, when the temperature was further increased to 400 K and 500 K, the atomic percentage of C decreased significantly. Furthermore, the C 1s binding energy is shifted from ~285.1 eV to ~283.6 eV. These results indicates that atomic hydrogen cleaning can effectively remove surface carbon contamination. However, atomic hydrogen cleaning seems to have little effect on reducing the oxygen atomic %. There is no significant change in the O atom content from 200 K to 500 K.

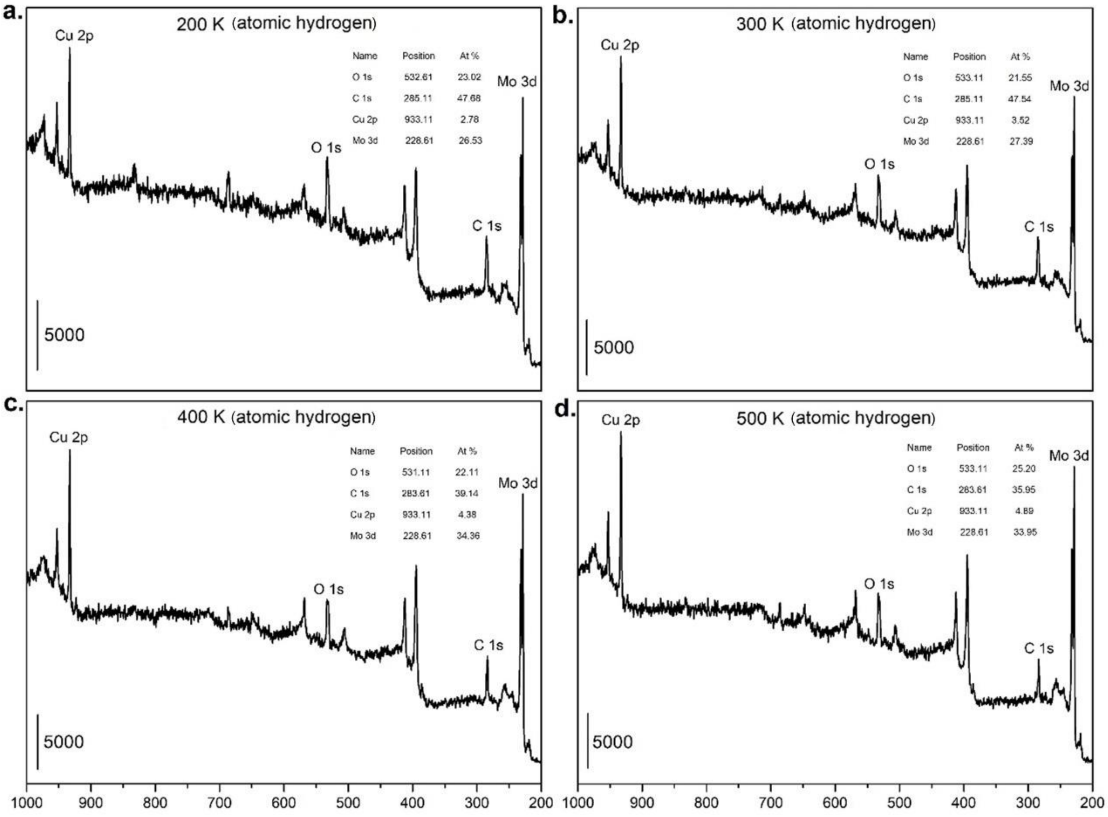

Figure 49 XPS survey scan spectra acquired following atomic hydrogen treatment of a high coverage 2D-Mo_2C/Cu sample. (a) Atomic hydrogen cleaning for 2 h at 200 K. (b) Atomic hydrogen cleaning for 2 h at 300 K. (c) Atomic hydrogen cleaning for 3.5 h at 400 K. (d) Atomic hydrogen cleaning for 4 h at 500 K.

The results of an experiment combining H treatment and high temperature annealing are displayed in **Figure 50** for an area displaying a high coverage of the carbide. The 2D-Mo_2C/Cu sample was first held at 573 K for 2 h under ultrahigh vacuum and then cooled to 300 K before taking an XPS measurement at an analysis angle of approximately 45° between the XPS analyzer lens and the 2D-Mo_2C surface. As expected, the survey scan spectrum of the degassed sample (**Figure 50a**) shows Mo (3d) and Mo(3p) doublets and the Mo (3s) peak at ~228.6 eV, ~394.7 eV and 505.9 eV, respectively. The Cu (2p) doublet is at ~933.1 eV and the Cu LMM Auger peaks are in the 550-750 eV region. In addition to the C(1s) peak at ~284.1 eV there is an O(1s) peak at ~532.6 eV. **Figure 50b** shows the spectrum of the same sample acquired following treatment with atomic hydrogen at 600 K for 4 h in a H_2 (~10^{-8} Torr) background and subsequent annealing to 1100-1150 K. The high temperature annealing greatly reduces the O content, and atomic hydrogen is efficient to remove carbon contamination. Overall, the ratio of Mo to C is changed from 1.10 to 1.65 by the combined treatment. However, there is an increase in the atomic percentage of Cu indicating that some 2D to 3D transformation occurs in the carbide layer.

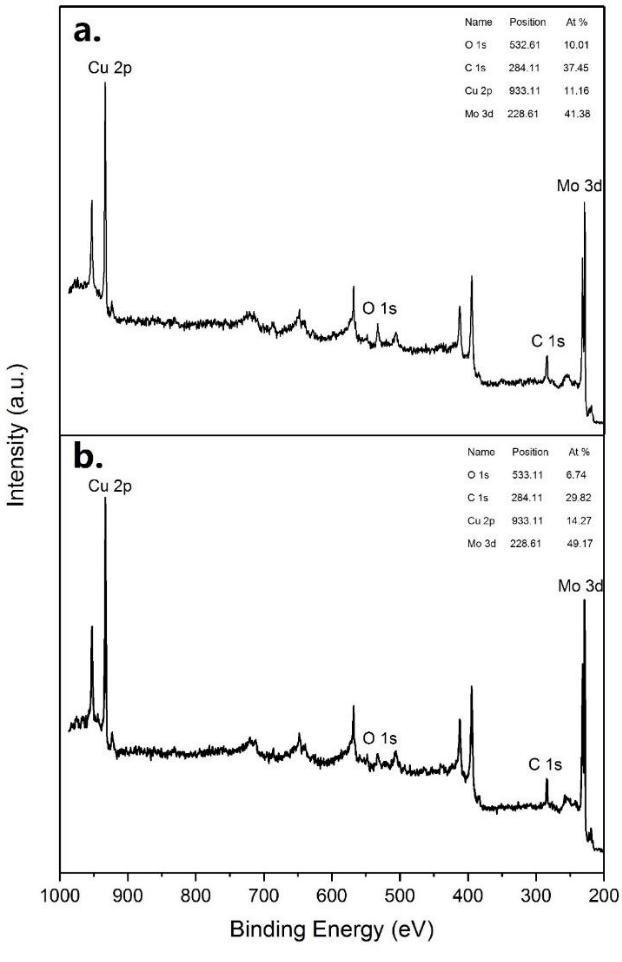

Name	Position	At %
O 1s	532.61	10.01
C 1s	284.11	37.45
Cu 2p	933.11	11.16
Mo 3d	228.61	41.38

Name	Position	At %
O 1s	533.11	6.74
C 1s	284.11	29.82
Cu 2p	933.11	14.27
Mo 3d	228.61	49.17

Figure 50 (a) XPS spectrum of high coverage 2D-Mo_2C/Cu prior to exposure to atomic hydrogen. (b) XPS spectrum of the same sample after atomic hydrogen treatment (600 K, 10^{-8} Torr H_2 background, 4 h).

High resolution C is spectra taken before and after atomic hydrogen treatment are shown in **Figure 51**. These peaks are used to fit the spectra. The lowest binding energy peak at 283.7 eV is attributed to Mo-C of 2D-Mo_2C. The C 1s peak at 284.9 eV is attributed to Gr or carbon contamination. The highest binding energy peak is attributed to carbon bonded to oxygen [190]. The peak area of the peak at 283.7 eV is increased and the areas of the peaks at 284.9 eV and 287.5 eV are decreased indicating that carbon contamination is successfully removed by atomic hydrogen.

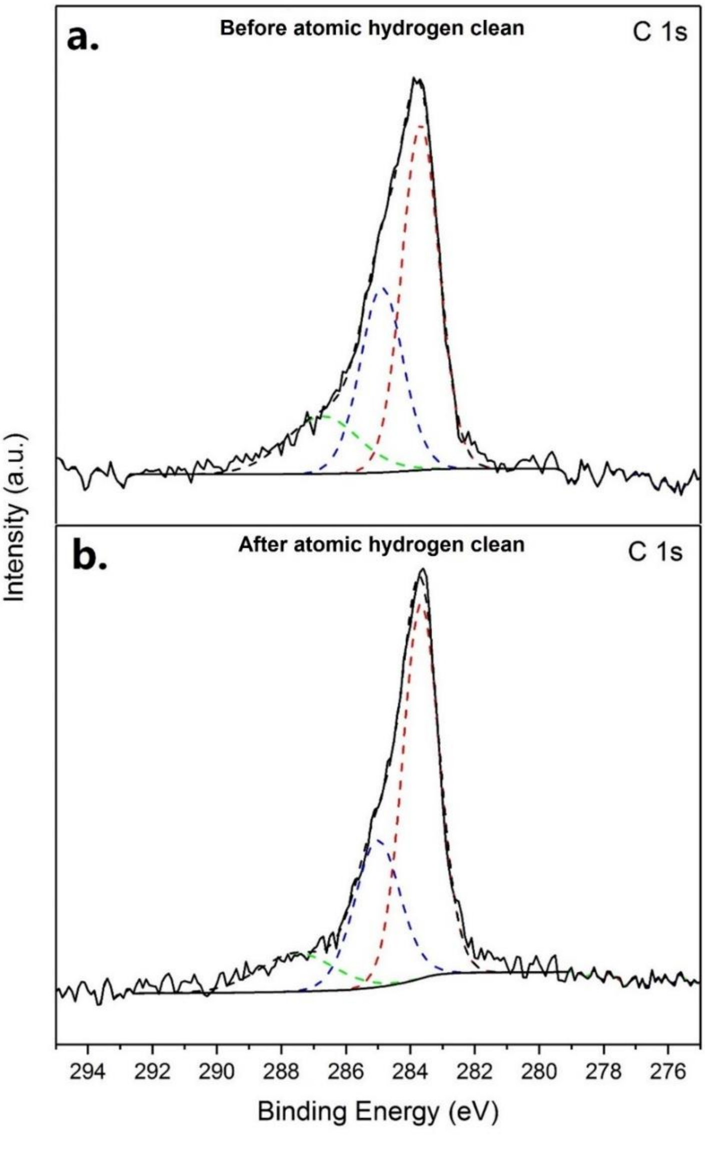

Figure 51 (a) C 1s spectrum of high coverage of 2D-Mo_2C/Cu at 300 K before atomic hydrogen treatment. (b) C 1s spectrum of high coverage 2D-Mo_2C/Cu after atomic hydrogen treatment (600 K, 10^{-8} Torr H_2, 4 h).

4.3.3 Treatment of 2D-Mo_2C/Cu by O/Ar Ion Sputtering

The XPS spectra in **Figure 51** show that a significant level of non-carbide carbon, indicated by the signal at ~285.0 eV, is still present after atomic hydrogen treatment. To remove the stubborn excess carbon, O/Ar ion sputtering was introduced in the experiment by using Ar containing 1-2 % O_2. **Figure 52** shows C 1s data for Ar/O sputtering of high coverage 2D-Mo_2C/Cu at 600 K in a background pressure of 2-3 × 10^{-6} Torr. The sample used in these experiments was first cleaned by atomic hydrogen treatment to give the spectrum shown in **Figure 51b**. As the O/Ar ion sputtering time increases from 0 min to 120 min, the relative area of C-Mo peak at 283.7 eV is increased from 49.5% to 73.7%, while the relative area of relative C-C peak at 285.0 eV is decreased from 40.7 % to 11.7 %. The result illustrates that O/Ar ion sputtering is very effective method to remove excess carbon. Mo 3d spectra before and after 120 min O/Ar ion sputtering are shown in **Figure 53**. The intensity of the Mo 3d peaks is stronger after O/Ar ion sputtering, but the binding energies and linewidths remain unchanged (**Figure 53**). The result indicates that O/Ar ion sputtering at 600 K does not damage or oxidize 2D-Mo_2C but that excess carbon is removed.

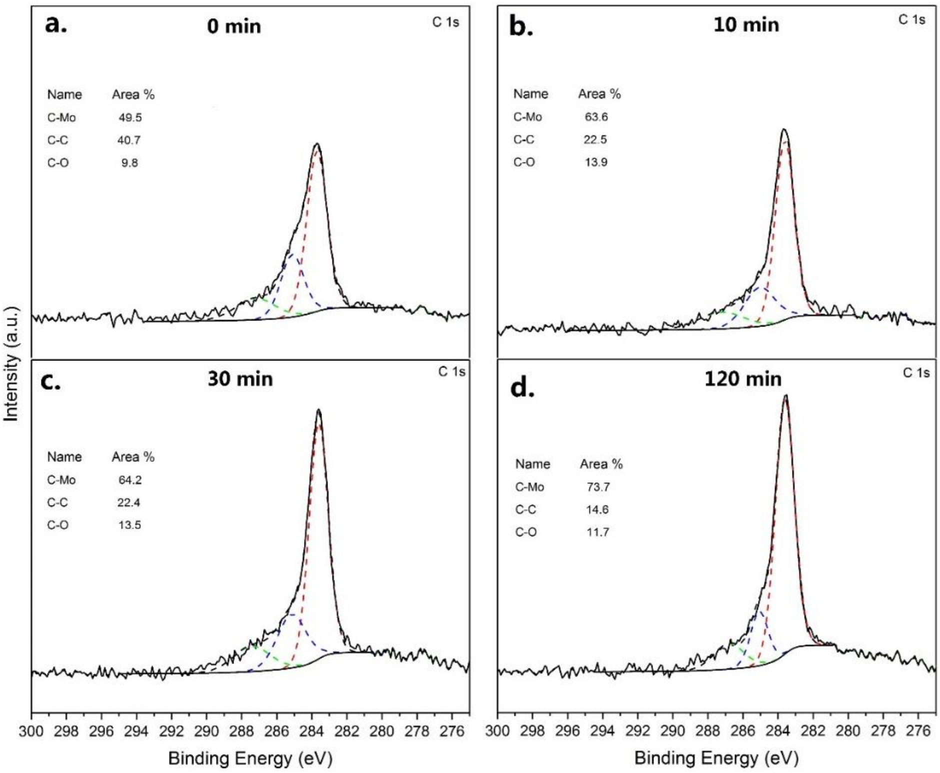

Figure 52 C 1s spectra and the C-Mo, C-C and C-O peak area percentages after different O/Ar ion sputtering times. (a) 2D-Mo_2C/Cu after atomic hydrogen cleaning (600 K, 10^{-8} Torr H_2, 4 h). (b-d) The same 2D-Mo_2C/Cu sample after O/Ar ion sputtering (600 K, 2-3 × 10^{-6} Torr 1-2 % O_2/Ar) for 10 min, 30 min and 120 min, respectively.

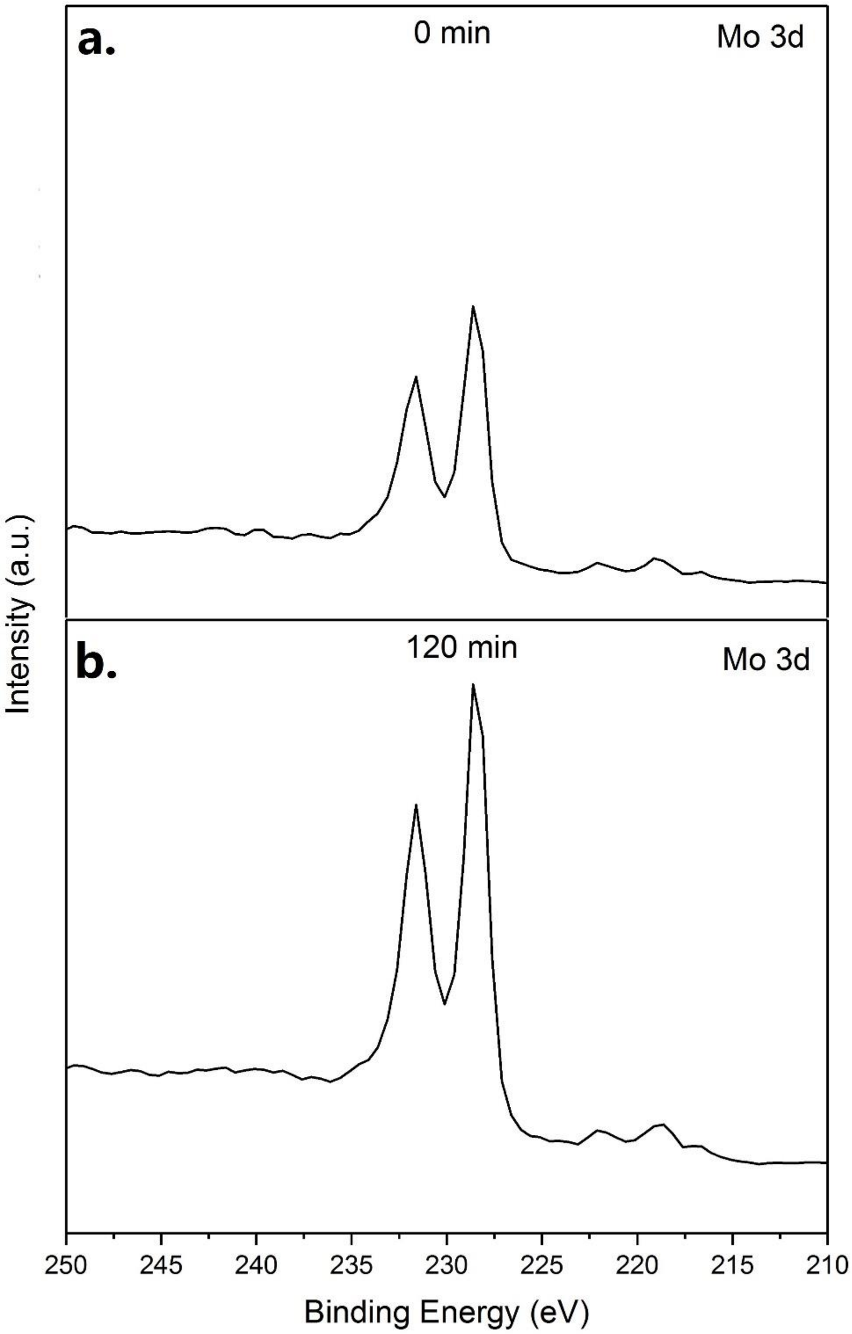

Figure 53 Mo 3d spectra before and after O/Ar ion sputtering. (a) 2D-Mo_2C/Cu after atomic hydrogen cleaning (600 K, 10^{-8} Torr H_2, 4 h). (b) Subsequent O/Ar ion sputtering (600 K, 2-3 × 10^{-6} Torr 1-2 % O_2/Ar) of the 2D-Mo_2C/Cu sample for 120 min.

4.4 Investigation of NHC Formation on 2D-Mo_2C/Cu Surfaces

As reported in Chapters 2 and 3, **NHC-2** (**Figure 26b**) forms chemisorption bonds with Pt(111) and Ru(0001) surfaces and with graphene on both surfaces. The 2D-Mo_2C/Cu samples used in this part of the study present a complex substrate in that adsorption on Cu, Mo_2C and potentially graphene needs to be simultaneously considered. Crudden and co-workers reported a study of diisopropylbenzimidazolium NHC chemisorption on Cu(111) [15]. They found that the surface NHC formed at 300 K was oriented perpendicularly to the surface and that it desorbed cleanly at 570 K. In the present study, we compared samples displaying high and low surface coverages of 2D-Mo_2C, as determined from Mo:Cu atomic percentages taken from full scan XPS spectra measurements. The high coverage samples are assumed to minimize the contribution of NHC adsorption on Cu.

4.4.1 Investigation of NHC-2 Formation on High Coverage 2D-Mo_2C Samples that were Pretreated with Atomic Hydrogen

A sample with a high surface coverage of Mo_2C was chosen for study first. **Figure 54** shows C(1s) spectra for the interaction of **NHC-2** with a sample that was cleaned using atomic hydrogen for 4 h at 600 K, then annealed to 1100 K. Peak fitting of the C(1s) signal shows peaks at 283.7 eV (red), 284.9 eV (blue) and 287.5 eV (green). The peak at 283.7 eV is attributed to the 2D-carbide although the C(1s) binding energy for bulk Mo_2C is typically at ~283.0 eV. The peak at 284.9 eV is characteristic of sp^2 carbon as in C-C bonds of graphene or graphite. The experiment does not reveal whether the graphene (or graphitic carbon) is on Mo_2C or Cu or both. The peak at 287.5 eV is characteristic of C-O or C=O bonds. This sample was found to be inactive towards **NHC-2** chemisorption. Exposure to **NHC-2** (5×10^{-7} Torr, 5 min) at 280 or 300 K led to no change in the C(1s) spectra (**Figure 54b** and **c**). However, exposure at 260 K led to physical adsorption of the **NHC-2** precursor as indicated (**Figure 54d**) by a characteristic CF_3 C(1s) peak at 293.5 eV and a strong C(1s) peak at 286.1 eV arising from the remaining 13 C atoms of **NHC-2**. The fact that chemisorption on the Cu substrate is not observed is attributed to the high coverage of Mo_2C and possibly also to passivation of copper by graphene or graphitic carbon.

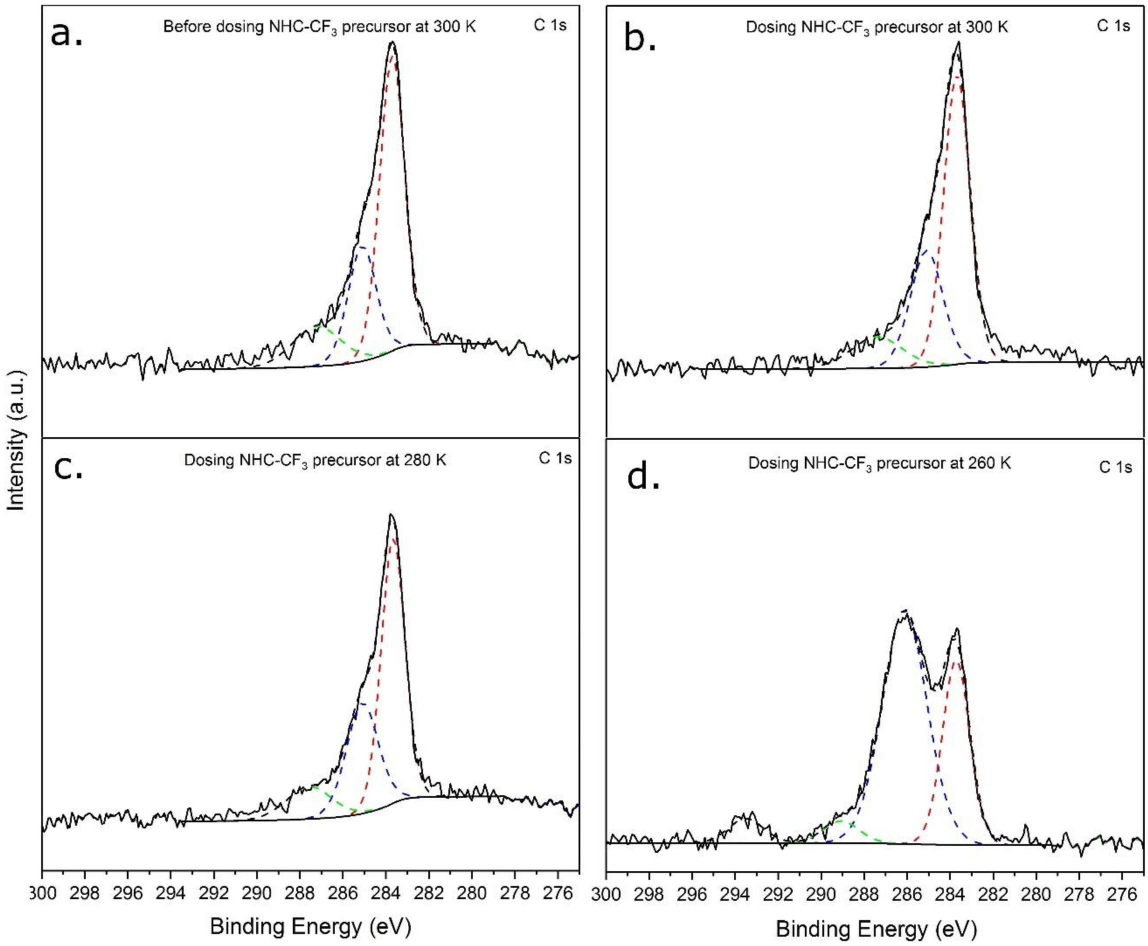

Figure 54 C 1s XPS spectra for the interaction of the **NHC-2** precursor with a high coverage 2D-Mo$_2$C sample. (a) C 1s spectrum of the 2D-Mo$_2$C/Cu sample before exposure to the **NHC-2** precursor. (b, c, d) C 1s spectra after exposure to **NHC-2** precursor with the sample at 300, 280 and 260 K, respectively.

Experiments were performed where the **NHC-2** precursor (5 × 10^{-7} Torr, 5 min) was dosed at 260 K, followed by anneal to higher temperatures. **Figure 55a** shows the XPS spectra of the 2D-Mo$_2$C sample before **NHC-2** precursor dosing at 260 K. The sample was first cleaned at 600 K under atomic hydrogen followed by an anneal to 1100 K. C 1s and F 1s XPS spectra are shown in **Figure 55b** and **c**. The F 1s peak marked by blue dash (688.9 eV) belongs to C-F from the **NHC-2** precursor or adsorbed **NHC-2** and the peak marked by red dash (685.8 eV) belongs to Mo-F from decomposed **NHC-2**. The characteristic C-F peaks (293.6 eV C1s and 688.9 eV, F 1s) can be detected until 450 K, indicating that **NHC-2** is able to create a covalent bond with 2D-Mo$_2$C. As shown in chapters 2 and 3, **NHC-2** forms a covalent bond on Gr/Pt(111) and Gr/Ru(0001) following exposure at 300 K. However, signal for **NHC-2** on 2D-Mo$_2$C is only seen when exposure is carried out at 260 K and the sample is then heated. This observation is not understood. It should be kept in mind that the sample shows a strong C-C C 1s peak at 285.1 eV. It is then possible that the **NHC-2** precursor only contacts excess carbon at the surface, but not the 2D-Mo_2C surface. Due to the strong bonding ability of **NHC-2** ligands, a covalent bond still can be created between **NHC-2** and surface carbon. The carbon-covered 2D-Mo_2C surface may be graphene or a graphite layer, as described in related papers [190,191].

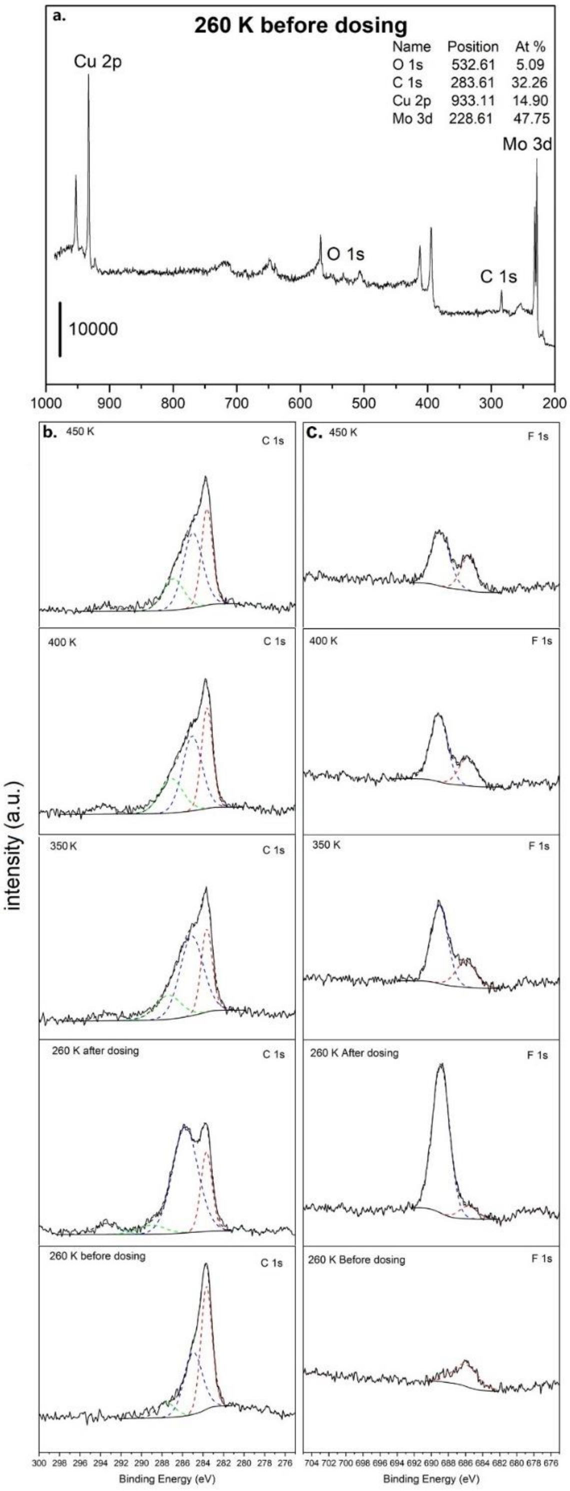

Figure 55 (a) Survey scan spectrum of a high coverage area of 2D-Mo_2C/Cu before **NHC-2** precursor dosing at 260 K. (b) C 1s and (c) F 1s spectra before and after dosing the **NHC-2** precursor. (b) C 1s XPS spectra before and after **NHC-2** precursor dosing at 260 K, followed by temperature increases to 350 K, 400 K and 450 K. (c) F 1s spectra before and after **NHC-2** precursor dosing at 260 K, followed by temperature increase to 350 K, 400 K and 450 K.

4.4.2 NHC-2 Precursor on 2D-Mo_2C/Cu Prepared by O/Ar Ion Sputtering

The experiments described above, **NHC-2** does not form a chemical bond to 2D-Mo_2C/Cu samples that have only being cleaned by exposure to atomic hydrogen at 600 K. This is interpreted as being due to the presence of a graphene or graphitic layer on the surface of the sample. Experiments were then performed on samples treated at 600 K by sputtering using Ar containing a 1-2% O_2 impurity, followed by annealing to 1100 K to remove O contamination. The objective was to combine argon ion sputtering with chemical reaction by oxygen to remove carbon as either CO or CO_2. The O/Ar treatment was performed at 600 K so as to ensure rapid desorption of CO or CO_2.

Figure 56a shows XPS spectra of 2D-Mo_2C before **NHC-2** precursor dosing at 300 K. Whereas **NHC-2** cannot combine with carbon covered 2D-Mo_2C surface after atomic hydrogen cleaning at 300 K (**Figure 54b**), characteristic C-F peaks are seen when the **NHC-2** precursor is dosed onto 2D-Mo_2C at 300 K after O/Ar ion sputtering. In addition, the C-C peak displays a clear shift to 285.7 eV and the peak intensity is significantly increased after **NHC-2** precursor dosing at 300 K. The strong C-C peak is attributed to the **NHC-2** skeleton. These results indicate that **NHC-2** forms a covalent bond with 2D-Mo_2C at 300 K. We propose that some surface graphene/graphitic carbon is removed by O/Ar ion sputtering (**Figure 52**) enabling **NHC-2** ligands to combine with Mo-terminated 2D-Mo_2C. Therefore, **NHC-2** interacts more strongly with the O/Ar treated 2D-Mo_2C sample. The carbene is more thermally stable than on the carbon covered surface. Characteristic C-F peaks are still detected at 550 K, which is 100 K higher than for **NHC-2** on the carbon covered surface **Figure 55**. On the other hand, the stability of **NHC-2** on 2D-Mo_2C seems weaker than on Pt-group metal surfaces like Pt(111) and Ru(0001). The **NHC-2** ligand on Pt(111) can be detected at 700 K and the **NHC-2** ligand on Ru(0001) can be detected at 600 K (**Figure 32** and **Figure 34**). This could be for 2 reasons. One is that a graphene/graphitic layer is present, as indicated by **Figure 52d**, with the result that stability is similar to that observed for Gr/Pt. Carbon forming C-C bonds still accounts for 14.6 % of the C is signal after 120 min O/Ar ion sputtering in **Figure 52d**. The other is that the Mo sites are highly reactive and the **NHC-2** decomposes.

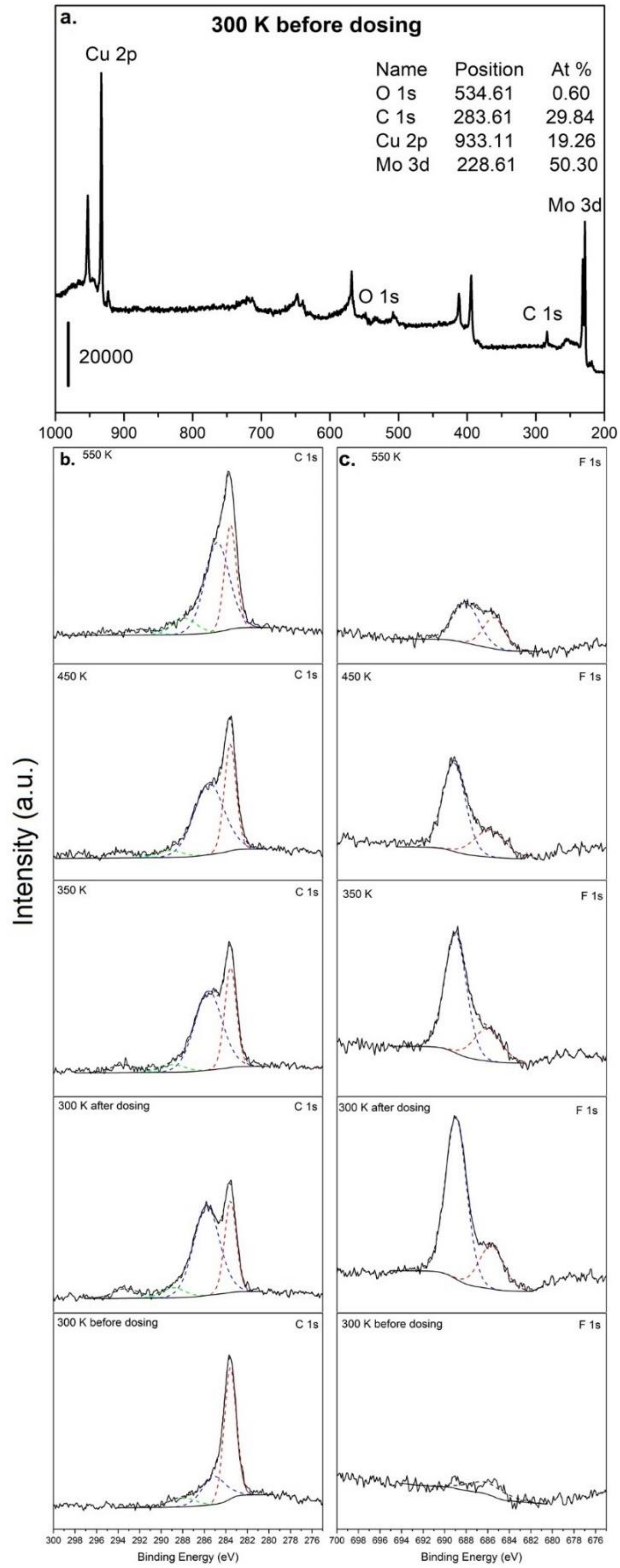

Figure 56 (a) XPS spectrum of a high coverage area of 2D-Mo_2C/Cu before **NHC-2** precursor dosing at 300 K. (b) C 1s spectra before and after exposure to the precursor at 300 K, followed by 5 min anneals to 350 K, 450 K and 550 K. (c) Corresponding F 1s spectra.

XPS spectra alone are difficult to interpret in terms of specific molecular adsorption structures on a sample as complex as 2D-Mo_2C/Cu. Hence, RAIRS was used in an attempt to obtain molecularly specific information. RAIRS data are compared in **Figure 57** for the interaction of the NHC precursor with a sample that was is cleaned by atomic hydrogen treatment at 600 K for 4 h, followed by 1100 K annealing (**Figure 57a**) and a sample that was prepared by O/Ar ion sputtering at 600 K for 2 h, followed by 1100 K annealing (**Figure 57b**). The spectra acquired on dosing the samples at 250 K show a strong peak at 1685 cm^{-1} arising from the carbonate group of the precursor. The spectra acquired on annealing the samples to 300 K are similar to those measured for Gr/Pt(111) and Gr/Ru(0001) at 300 K. The latter spectra were attributed to a flat-lying NHC following removal of the carbonate group. The out-of-plane aromatic CH bending vibration is seen at 819 cm^{-1}.

In both cases, two out-of-plane $\upsilon_{asym}(CF_3)$ stretching bands are observed, one at 1119 cm^{-1} and one at 1139 cm^{-1}. The band at 1139 cm^{-1}, on the O/Ar treated surface, is observed to 450 K, indicative of the presence of a flat-lying NHC, as observed for Ru(0001) and to a lesser extent for Pt(111). Very weak bands are also seen at 1339 and 1185 cm^{-1}, consistent with the presence of a small surface coverage of upright NHC groups on the O/Ar treated sample. In addition, there is a weak peak at 1268 cm^{-1} that is attributed to CF_3 containing decomposition products as observed for Pt(111) and Ru(0001). A decomposition process is supported by the XPS spectra of O/Ar treated samples, as in **Figure 57c**, showing a characteristic Mo-F F(1s) peak at 685.7 eV, following exposure to the **NHC-2** precursor. In contrast, XPS (**Figure 55c)** and RAIRS spectra (**Figure 58a**) show that the characteristic Mo-F peak at 685.8 eV does not increase much after dosing the **NHC-2** precursor on the sample treated with atomic hydrogen. Decomposition does not occur on the latter surface at 350 K (**Figure 58a**). This result also shows that even after atomic hydrogen treatment, 2D-Mo_2C is still covered by a carbon layer, so that **NHC-2** cannot be decomposed on Mo sites. However, the RAIRS peak intensities are much weaker than observe for Pt(111) and Ru(0001). The weak intensities may be due to few adsorption sites for NHC formation on the 2D-Mo_2C/Cu surface or it may be due to extensive molecular decomposition at Mo sites. The latter is the more plausible interpretation as molybdenum is a highly reactive metal.

Figure 58 shows RAIRS spectra acquired following **NHC-2** precursor adsorption on 2D-Mo_2C at 300 K after O/Ar ion sputtering. At 300 K, the out-of-plane $\upsilon_{asym}(CF_3)$ band is detected at 1139 cm^{-1} along with a shoulder at 1120 cm^{-1} and the CH aromatic bending mode at 820 cm^{-1}. The band at 1139 cm^{-1} is observed up to 500 K indicating that a small coverage of **NHC-2** ligands are stable on 2D-Mo_2C surface.

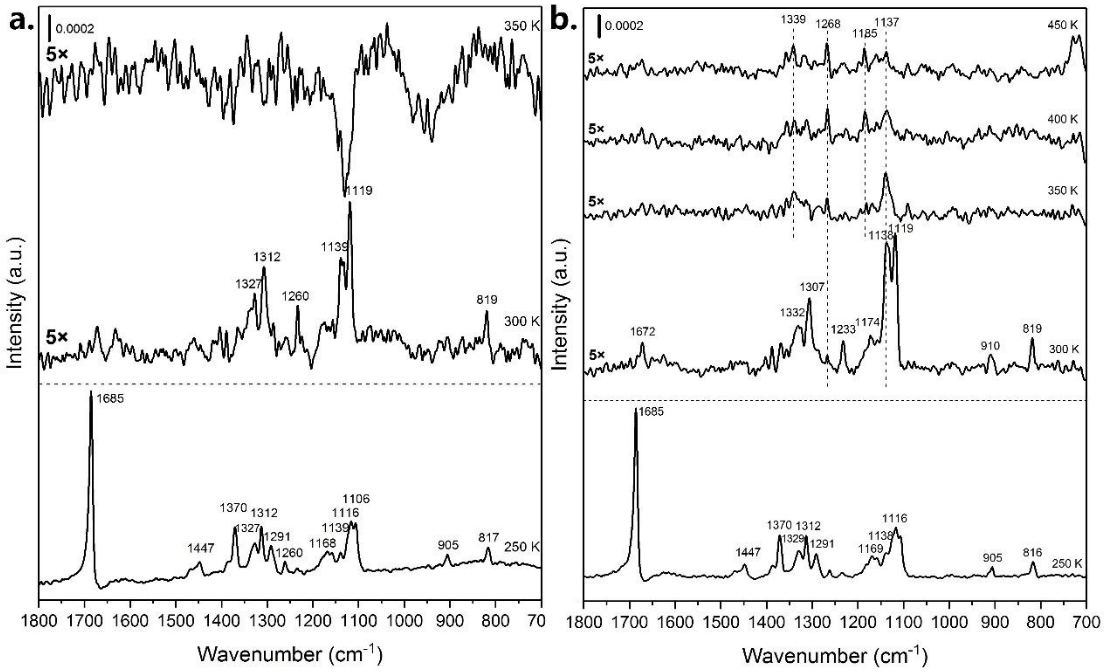

Figure 57 RAIRS spectra for **NHC-2** precursor adsorption on 2D-Mo_2C/Cu. (a) Adsorption at 250 K on a sample prepared by atomic hydrogen treatment, followed by 5 min anneals to the indicated temperatures. (b) Adsorption at 250 K on a sample prepared by Ar/O treatment, followed by 5 min anneals to the indicated temperatures.

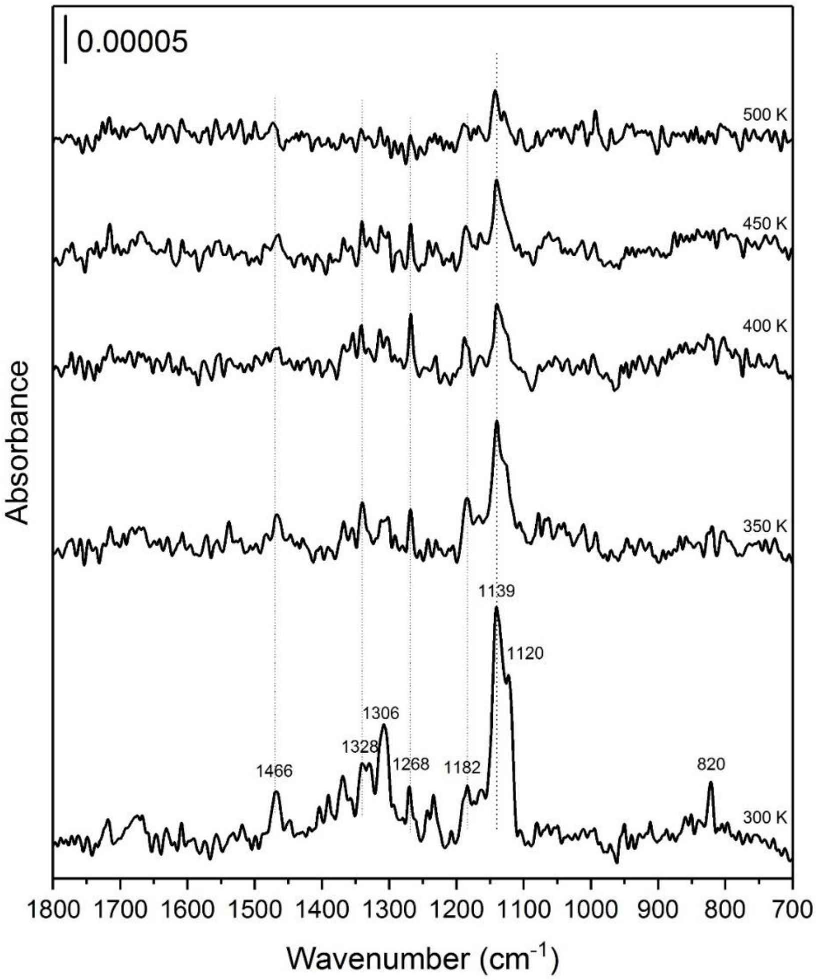

Figure 58 RAIRS spectra for **NHC-2** precursor adsorption on 2D-Mo_2C after O/Ar ion sputtering. The precursor was dosed at 300 K, followed by 5 min anneals to the indicated temperatures. The RAIRS background temperature was 250 K.

In conclusion, the NHC precursor interacts weakly with carbon covered samples prepared by atomic hydrogen treatment. Hence, NHC formation is not favoured on these surfaces. In contrast, surfaces prepared by O/Ar treatment may be too reactive, resulting in molecular decomposition. In light of these results, we then explored another method to functionalize the 2D-Mo_2C/Cu samples. As described next, the method relies on the selective scission of carbonyl bonds to form surface alkylidenes on Mo_2C.

4.5 Adsorption of CF_3-Benzaldehyde on 2D-Mo_2C/Cu

McBreen and co-workers published the first report of alkylidene functionalization of bulk α-Mo_2C sample (hexagonal phase Mo_2C) through selective carbonyl bond scission in chemisorbed ketones and aldehydes. In addition to spectroscopic measurements, the presence of surface alkylidenes was proven using olefin metathesis reaction tests.[192] For example, cyclopentylidene was formed through the dissociative chemisorption of cyclopentanone at ~300 K (**Scheme 4**) [193,194]. Cross-metathesis using propene resulted in the formation of CH_2 and $CHCH_3$ surface carbenes. The formation of cyclopentylidene from cyclopentanone is a deoxygenation step, and Mo_2C is known to be an excellent deoxygenation catalyst [193,194]. The oxygen atom bonds to Mo on the surface of the carbide, although the actual adsorption site is not known. The cyclopentylidene-Mo sites can also serve as initiating sites for ring-opening metathesis polymerization [80,193]. Hence, it is interesting to explore the possibility of functionalizing 2D-Mo_2C though the formation of surface alkylidenes that may subsequently serve as olefin metathesis initiating sites.

The formation of surface alkylidenes on Mo_2C is due to the high oxophilicity of Mo. Due to the 2D structure and Cu substrate of the α-Mo_2C material we use, the oxophilicity of Mo-terminated 2D-Mo_2C might be different than for bulk α-Mo_2C. Furthermore, the deoxygenation mechanism on 2D-Mo_2C might be different from that of bulk Mo_2C. For example, it might be less selective leading to excessive decomposition rather than selective alkylidene formation. Alternatively, the deoxygenation approach might prove to be a method to form more stable surface groups than in the NHC approach. Whereas NHCs form a single bond to metals, alkylidenes form a double bond and hence might be expected to be more stable thermally.

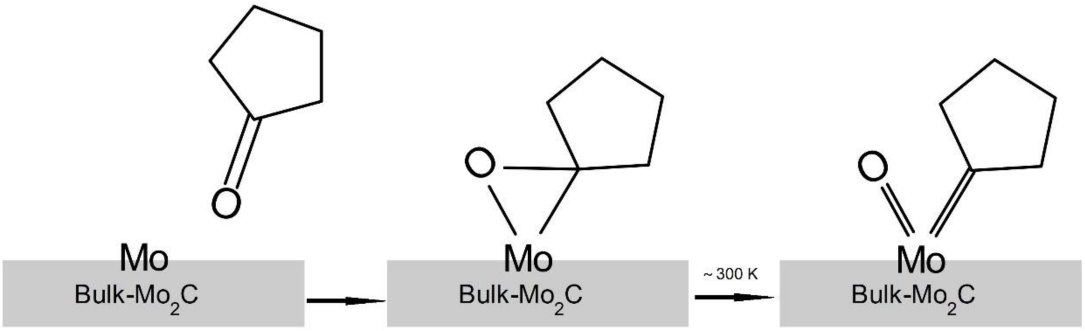

Scheme 4 Schematic illustration of deoxygenation of cyclopentanone through chemisorption on an α-Mo_2C surface. In the proposed mechanism, cyclopentanone first forms an oxometallacycle and then transforms to an oxo-Mo-cyclopentylidene complex at ~300 K. Reproduced with permission from Ref. [193], copyright 2006 Elsevier B.V.

4.5.1 CF_3-Benzaldehyde Adsorption on 2D-Mo_2C/Cu: XPS Studies

The 2D-Mo_2C/Cu sample was cleaned by O-Ar sputtering with annealing to 1100 K. From the XPS spectra shown in **Figure 59**, it can be seen that most but not all of the surface carbon can be removed by O-Ar sputtering, as shown by the C-C C 1s peak (blue dash) in **Figure 59a**. On 4-CF_3-benzaldehyde exposure at 300 K, the C-C peak (blue dash) at 285.2 eV and the C-O peak (green dash) at 287.1 eV are clearly increased. The C-F peak (light blue dash) is observed at 292.7 eV. F 1s spectra are shown in **Figure 59b**. Characteristic peaks for C-F bonds are seen in both C 1s and F 1s spectra at 350 K. This result and the fact that the C-O peak at 287.1 eV decreases in intensity, suggests that 4-CF_3-benzaldehyde undergoes deoxygenation by 350 K. On a further increase of the temperature to 400 K, a C-F C 1s peak still present but is greatly attenuated. Plots of F 1s peak areas as a function of anneal temperature are shown in **Figure 60**. The area of the C-F peak at 688.3 eV continuously decreases as the temperature increased to 400 K. At the same time, as the temperature increases, the Mo-F peak does not increase. This result indicates that 4-CF_3-styrylidene ligands desorb in the 300-400 K range. In summary, the results are consistent with a combination of decomposition, desorption and deoxygenation in the 300-400 K temperature range.

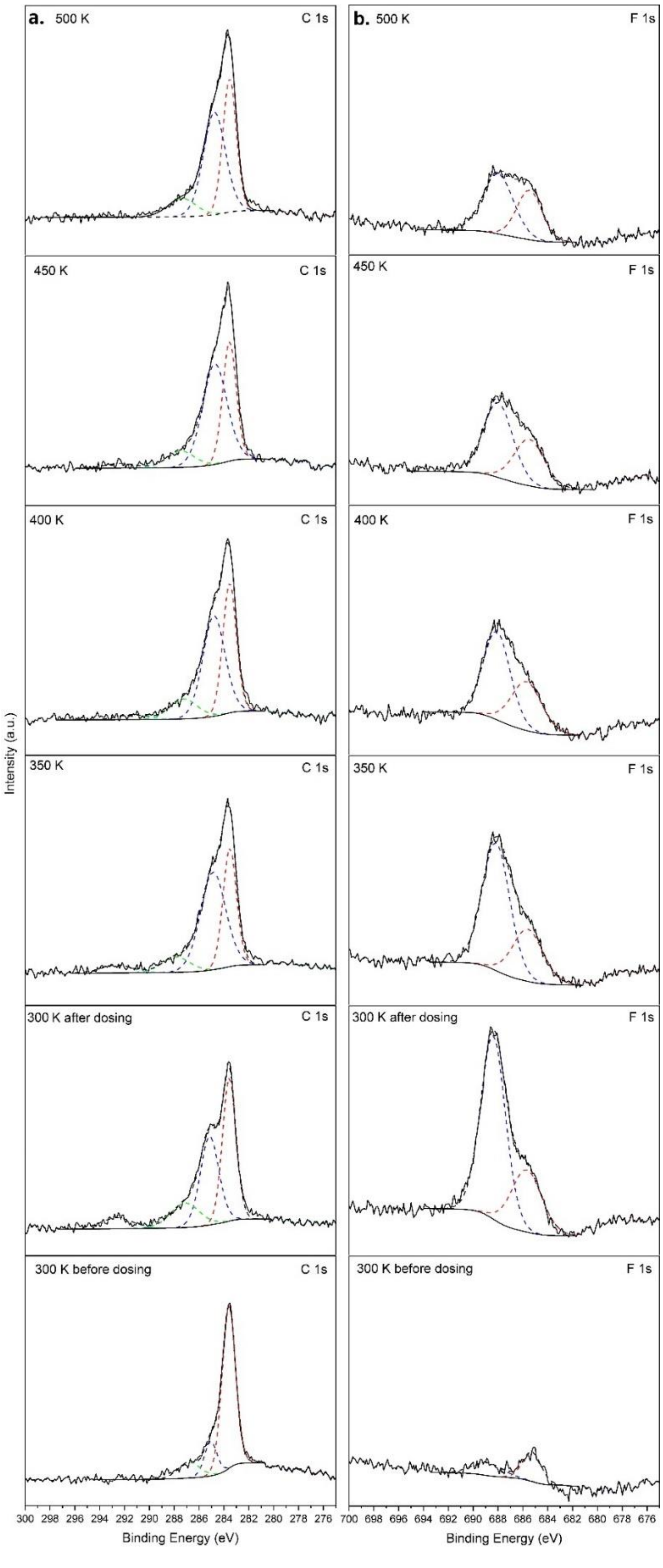

Figure 59 C 1s and F 1s spectra of 4-CF$_3$-benzaldehyde dosed 2D-Mo$_2$C/Cu. (a) C 1s spectra are fitted by 4 peaks: Mo-C (red dash), C-C (blue dash), C-O (green dash) and C-F (light blue dash). (b) F 1s spectra are fitted by 2 peaks: C-F (blue dash) and Mo-F (red dash).

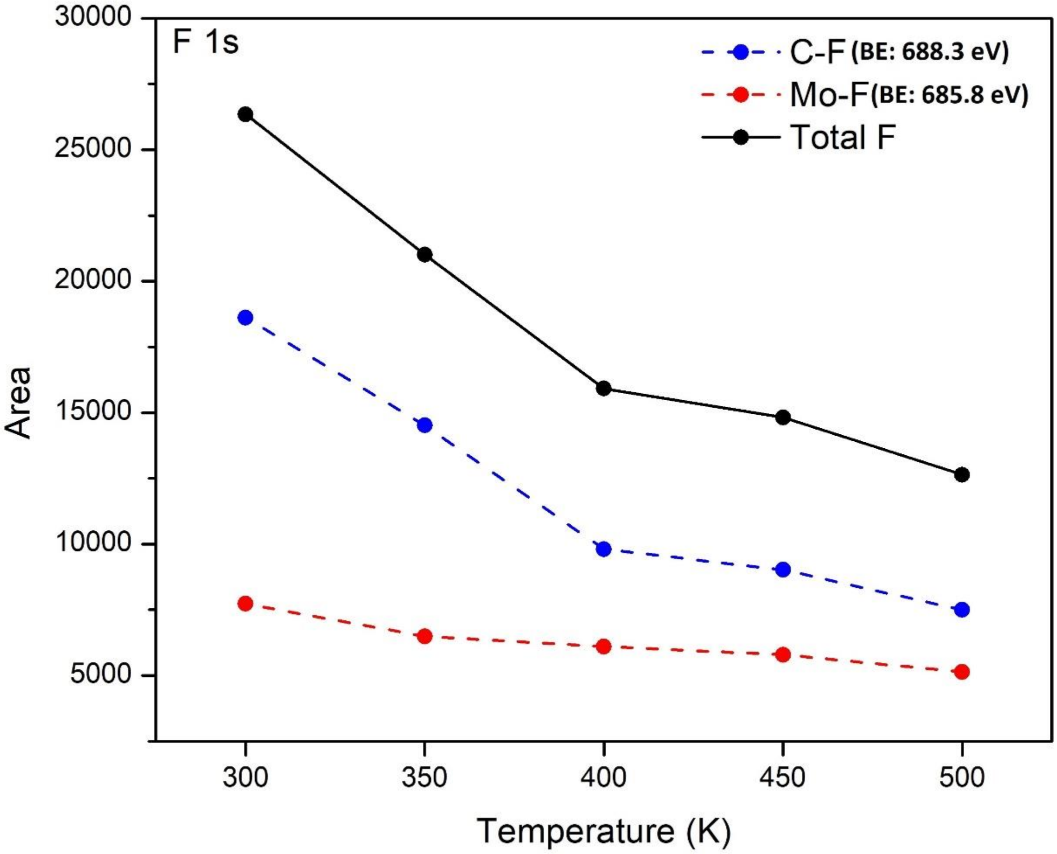

Figure 60 Peak areas of C-F and Mo-F peaks based on the F 1s spectra in **Figure 59**.

The XPS data provides evidence that 4-CF_3-benzaldehyde undergoes a deoxygenation step on 2D-Mo_2C/Cu. **Figure 61** shows O 1s spectra taken before and after dosing 4-CF_3-benzaldehyde onto the 2D-Mo_2C/Cu sample at 300 K. The intensity of the peak at 531.3 eV (red dash) is strongly increased but the C-O peak at 534.0 eV (blue dash) does not change in intensity. As shown in **Figure 62**, the total O signal remains constant over the 300-500 K range. The Mo=O and C-O peak areas are stable from 300 K to 350 K, but the Mo=O peak area is gradually decreased at higher temperatures. Interestingly, the C-O peak area increases and the increase in C-O peak area is the same as the decrease in Mo=O peak area. The result clearly indicates that oxygen bonded to Mo is transferred to form C-O bonds on 2D-Mo_2C as the temperature increases (**Figure 62**). However, there is no evidence of such a transfer on bulk Mo_2C [192–194]. The surface oxygen remains bonded to Mo on Mo-terminated bulk Mo_2C due to the strong oxophility of bulk Mo_2C. In contrast, O atoms have strong mobility on the 2D-Mo_2C surface and O atoms can shift from Mo sites to C sites on the 2D-Mo_2C surface at higher temperature (**Figure 62**).

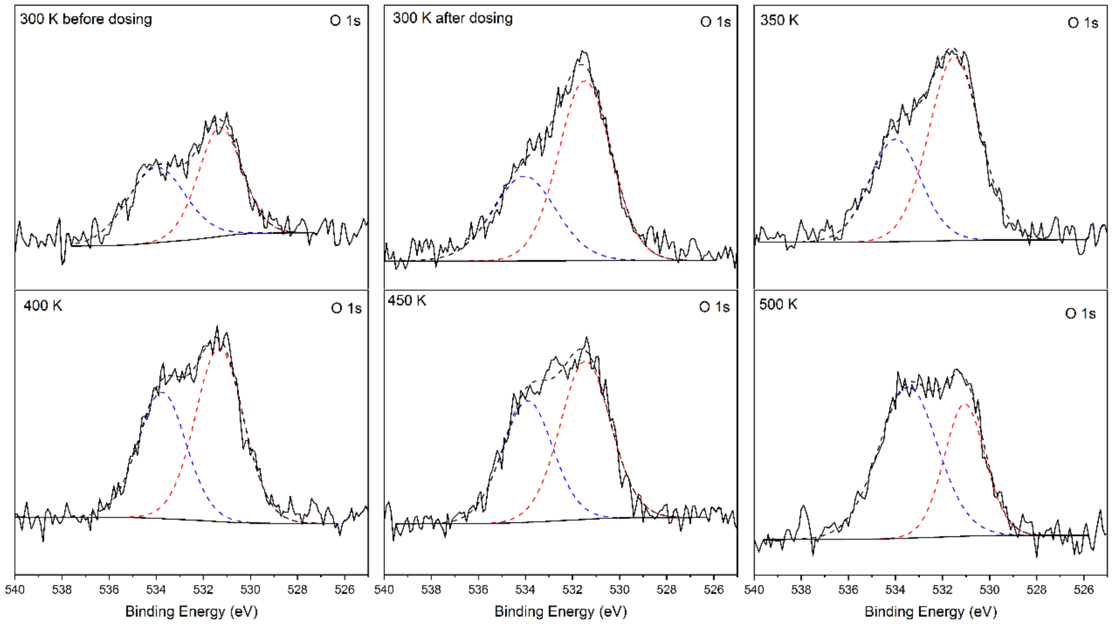

Figure 61 O 1s spectra acquired before and after exposure of 2D-Mo_2C/Cu at 300 K to 4-CF_3-benzaldehyde followed by increasing the temperature to 500 K. The dash red line peak at 531.3 eV is attributed to Mo=O. The dash blue line peak at 534.0 eV is attributed to C-O bonding.

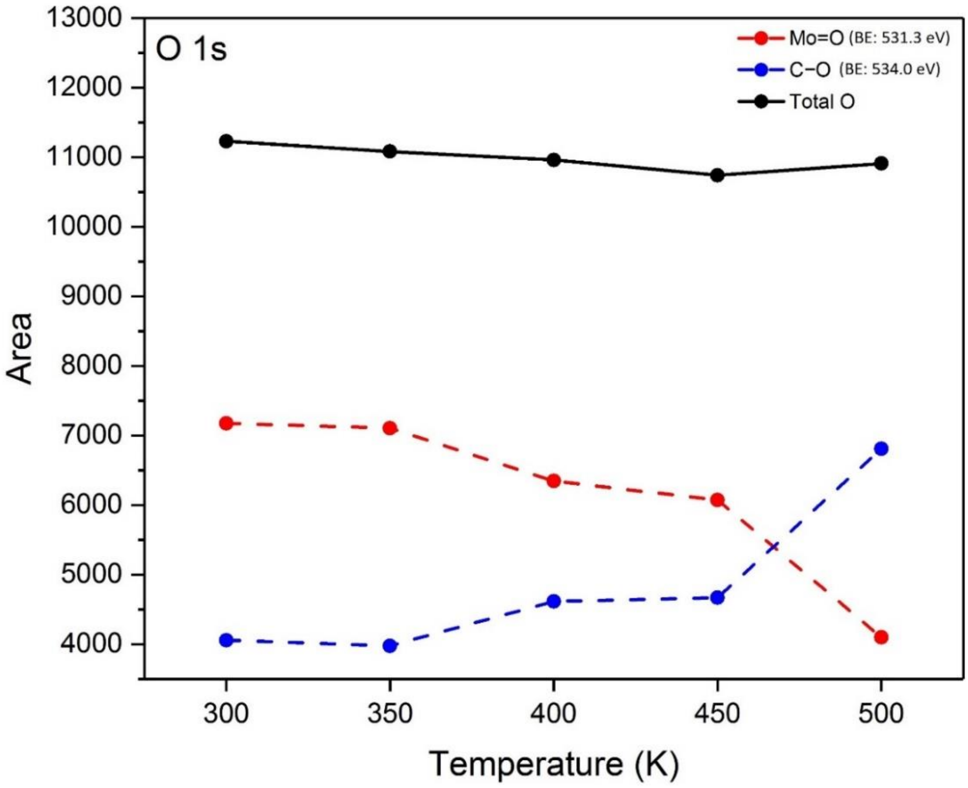

Figure 62 Areas of C-O and Mo=O peaks in the O 1s spectra shown in **Figure 61**.

4.5.2 RAIRS Measurements on the Adsorption of Benzaldehyde on 2D-Mo_2C/Cu

Both 3-CF_3-benzaldehyde and 4-CF_3-benzaldehyde were used as adsorbates in order to explore the molecular orientation of the chemisorbed surface species by examining the orientation of the C-CF_3 groups relative to the surface. **Figure 63** presents RAIRS spectra of 4-CF_3-benzaldehyde (**Figure 63a**) and 3-CF_3-benzaldehyde (**Figure 63b**) on 2D-Mo_2C/Cu. The same gas exposure conditions were used (30 L, 3×10^{-7} Torr, 100 s, 200 K) for the measurements. The background RAIRS spectrum was recorded at 200 K. Three vibrations are observed when both molecules are dosed on 2D-Mo_2C/Cu surface at 200 K. The peak positions and relative intensities are similar for both molecules. Adsorbed 4-CF_3-benzaldehyde displays a weak υ_{sym}(C-CF_3) band at 1334 cm^{-1}, a strong υ_{asym}(CF_3) band at 1160 cm^{-1} and an aromatic CH bending band at 841 cm^{-1}. The corresponding peaks for 3-CF_3-benzaldehyde are at 1334, 1154 and 812 cm^{-1}. The observation of a strong out-of-plane υ_{asym}(CF_3) band and a CH aromatic bending band, as well as the observation of a weak C-CF_3 band, shows that 4-CF_3-benzaldehyde and 3-CF_3-benzaldehyde molecules are flat lying on the 2D-Mo_2C surface at 200 K (**Scheme 5**). These observations and the intense absorption bands suggest that the molecules form a condensed layer on 2D-Mo_2C/Cu at 200 K. When the sample temperature was increased to 250 K, much weaker signals and significantly different spectra were observed, consistent with desorption of the condensed adsorbate to leave behind sub-monolayer chemisorbed states.

The CH aromatic out of plane bending mode is not observed at 250 K, indicating that the benzene ring is not parallel to the surface in the chemisorbed states. With reference to the spectra of **NHC-2** on Pt(111), Ru(0001), Gr/Pt(111) and Gr/Ru(0001) the bands observed for the chemisorbed layer are assigned to the υ_{sym}(C-CF_3) vibration (1334 cm^{-1}), in-plane υ_{asym}(CF_3) vibration (1178 cm^{-1}) and the out-of-plane υ_{asym}(CF_3) (1147 cm^{-1}). The υ_{sym}(C-CF_3) produces the strongest band in the case of 4-CF_3-benzaldehyde while it is relatively less strong for 3-CF_3-benzaldehyde. These observations are interpreted in terms of the alkylidene (styrylidene) structures shown in **Scheme 5**. The orientation of the C-CF_3 bond in 4-CF_3-styrylidene on 2D-Mo_2C/Cu leads to a relatively stronger υ_{sym}(C-CF_3) band. The feature at 1334 cm^{-1} is greatly attenuated on heating to 400 K, indicating that the alkylidene undergoes thermal decomposition.

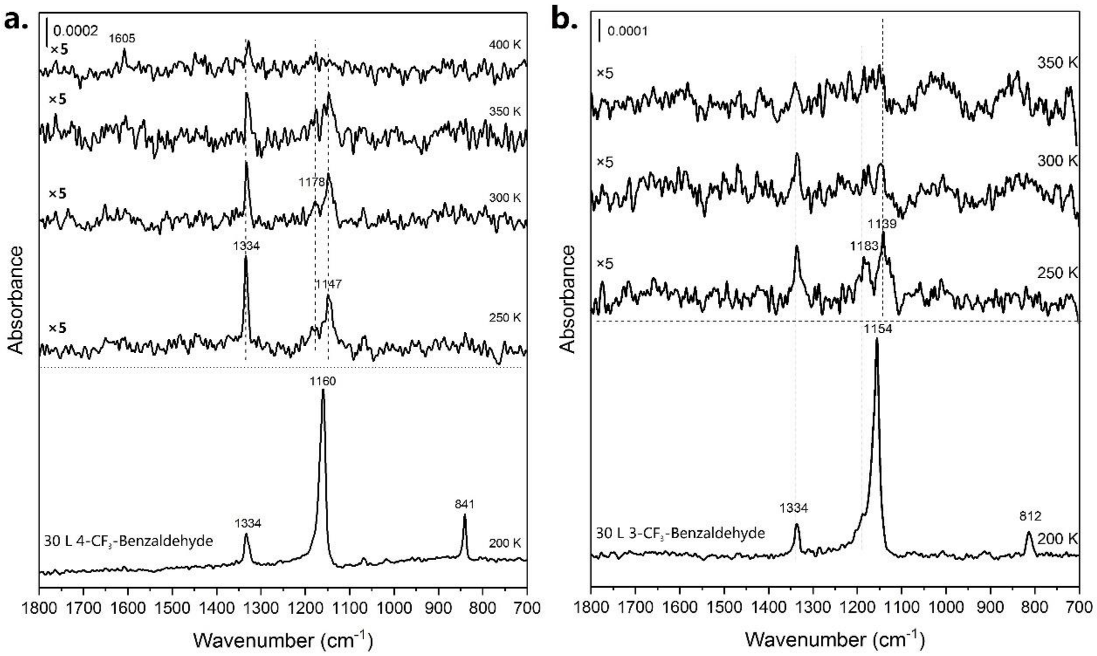

Figure 63 RAIRS spectra for 4-CF_3-benzaldehyde and 3-CF_3-benzaldehyde adsorption on 2D-Mo_2C/Cu. (a) 30 L 4-CF_3-benzaldehyde (3×10^{-7} Torr, 100 s) exposure with the sample at 200 K, followed by annealing to the indicated temperatures for 5 min. (b) 30 L 3-CF_3-benzaldehyde (3×10^{-7} Torr, 100 s) exposure with the sample at 200 K, followed by annealing to the indicated temperatures for 5 min.

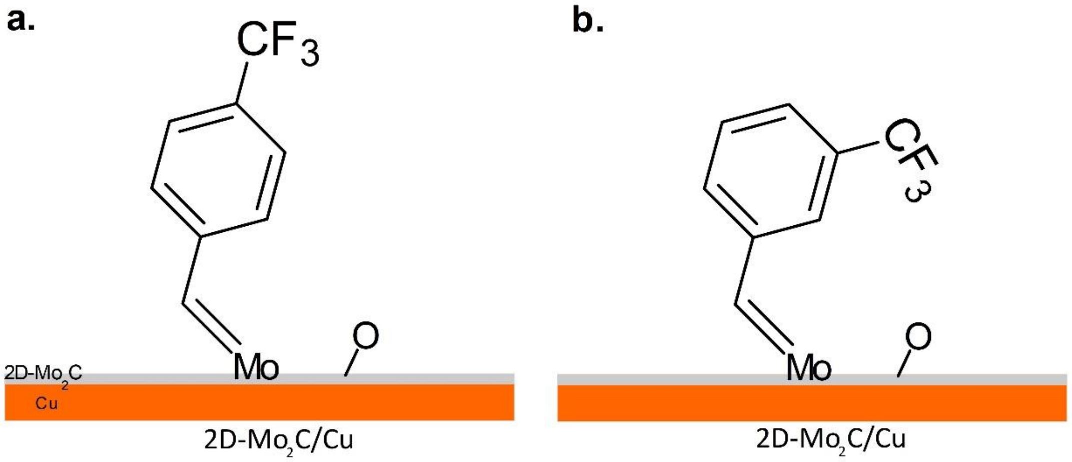

Scheme 5 Schematic structures of (a) 4-CF_3-styrylidene and (b) 3-CF_3-styrylidene ligands on 2D-Mo_2C/Cu.

The possible formation of styrylidene surface ligands was further explored by using high exposures (300 L) to 4-CF$_3$-benzaldehyde and 3-CF$_3$-benzaldehyde (300 L) at 250 K (**Figure 64**). The CH aromatic bending vibration is not observed at 250 K, consistent with the formation of upright 4-CF$_3$-styrylidene and 3-CF$_3$-styrylidene ligands on the 2D-Mo$_2$C/Cu surface. For 4-CF$_3$-benzaldehyde, a very strong υ_{sym}(C-CF$_3$) band is observed at 1333 cm^{-1} as well as weak in-plane υ_{asym}(CF$_3$) and out-of-plane υ_{asym}(CF$_3$) bands at 1183 cm^{-1} and 1140 cm^{-1}, respectively. In contrast, the strongest band for 4-CF$_3$-styrylidene is at 1149 cm^{-1} while the band at 1334 cm^{-1} is very weak. If these observations are interpreted according to the structures proposed in **Scheme 5**, then the band at 1149 cm^{-1} is due to the in-plane asymmetric CF$_3$ stretching vibration.

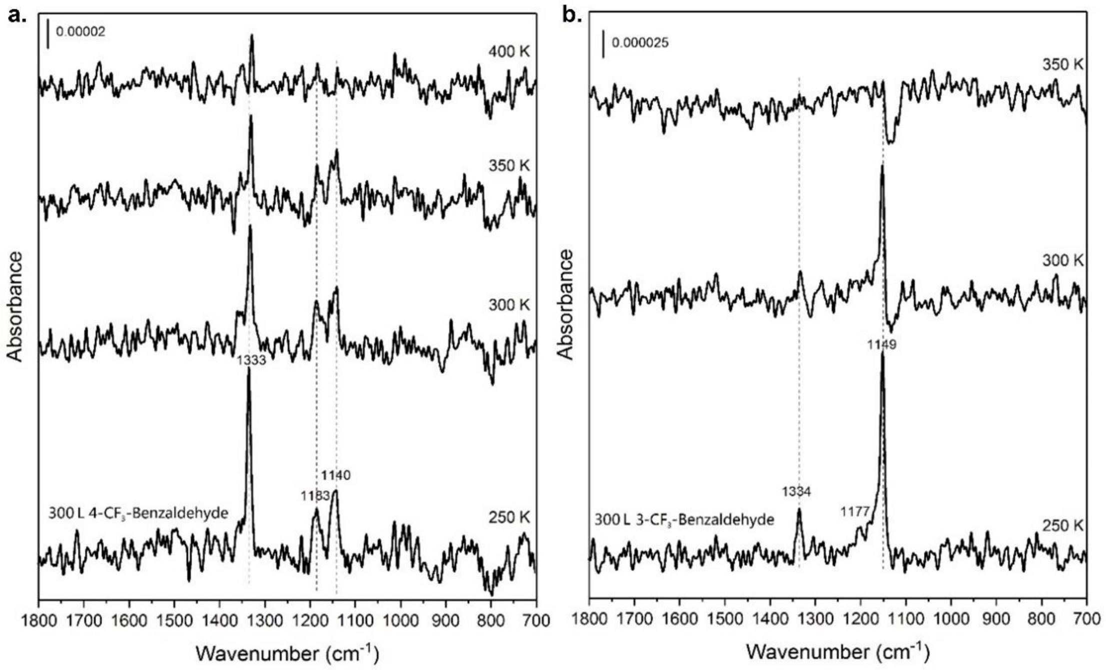

Figure 64 RAIRS spectra for 4-CF$_3$-benzaldehyde and 3-CF$_3$-benzaldehyde adsorption on 2D-Mo$_2$C/Cu. (a) 300 L 4-CF$_3$-benzaldehyde (10^{-6} Torr, 300 s) exposure with the sample at 200 K, followed by annealing to the indicated temperatures for 5 min. The background spectrum was acquired at 250 K. (b) 300 L 3-CF$_3$-benzaldehyde (10^{-6} Torr, 300 s) exposure with the sample at 200 K, followed by annealing to the indicated temperatures for 5 min. The background spectrum was acquired at 200 K.

The XPS spectra shown **Figure 59** present evidence that 4-CF$_3$-styrylidene ligands are formed on the 2D-Mo$_2$C/Cu 2D-Mo$_2$C surface when 30 L 4-CF$_3$-benzaldehyde is dosed on the surface at 300 K. In this context, **Figure 65** presents RAIRS spectra for 30 L 4-CF$_3$-benzaldehyde (3 × 10^{-7} Torr, 100 s) exposure at 300 K. The detection of the υ_{sym}(C-CF$_3$) band at 1330 cm^{-1} further confirms that 4-CF$_3$-styrylidene ligands are formed under these conditions.

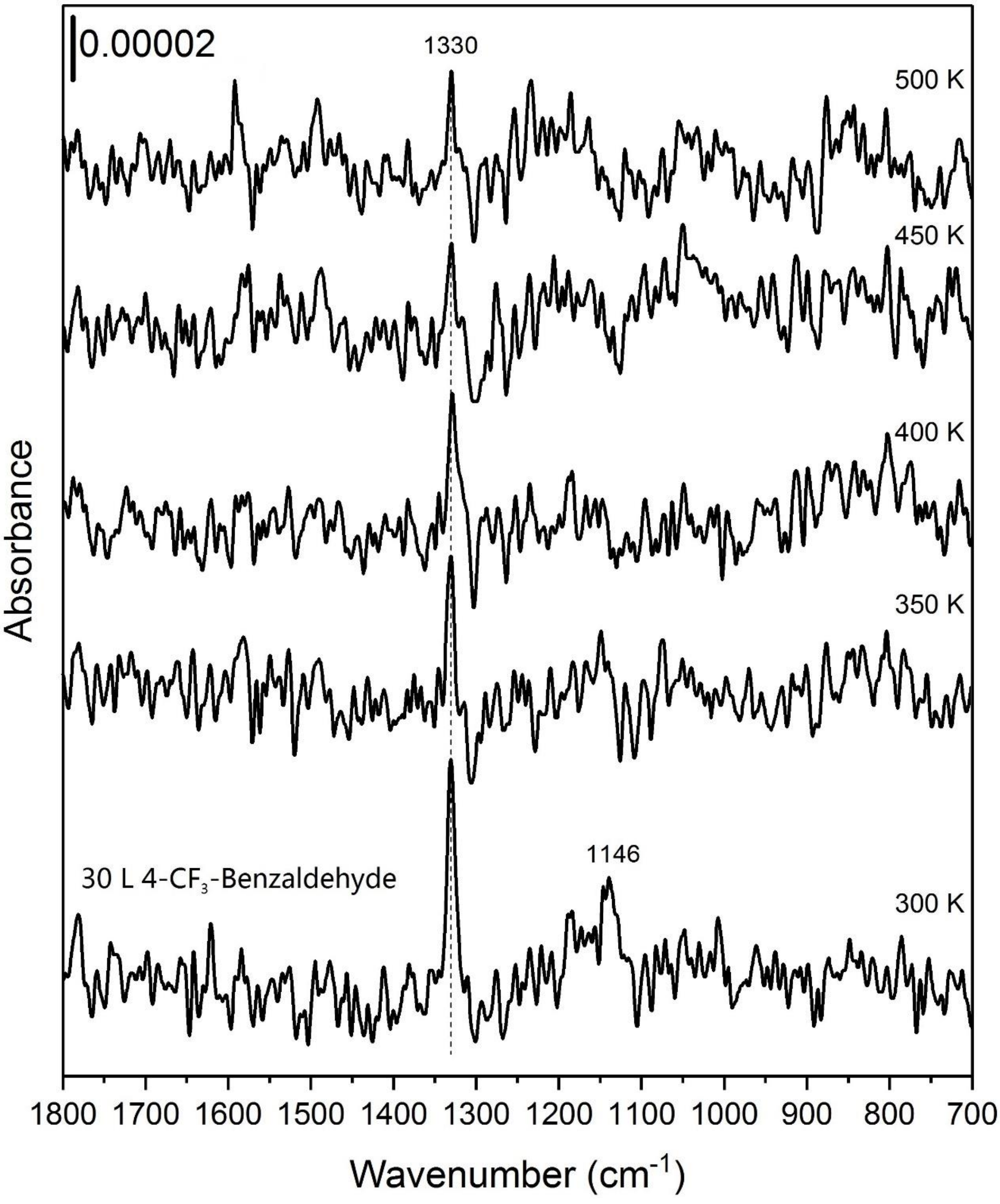

Figure 65 RAIRS spectra for 4-CF$_3$-benzaldehyde adsorption on 2D-Mo$_2$C/Cu. 30 L 4-CF$_3$-benzaldehyde (3 × 10^{-7} Torr, 100 s) at 300 K. The background spectrum was acquired at 250 K.

4.6 Summary and Conclusions

In conclusion, the surface of the as-received 2D-Mo_2C samples are covered by excess carbon, and there may even be a Gr/2D-Mo_2C/Gr sandwich structure [72]. Atomic hydrogen treatment is an effective method to remove carbon contamination, but excess carbon remains on the surface. O/Ar ion sputtering is an effective method to reduce the amount of excess carbon. Additional annealing at high temperature (1100 K) is able to greatly reduce the oxygen content. Therefore, O/Ar ion sputtering combined with high temperature annealing is an effective method for cleaning 2D-Mo_2C produced by the CVD method.

The existence of excess carbon on the 2D-Mo_2C surface inhibits **NHC-2** from forming a covalent bond with 2D-Mo_2C at 300 K, resulting in a very weak RAIRS signal that can be attributed to surface NHC. In contrast, **NHC-2** is able to form a covalent bond with 2D-Mo_2C at 300 K after O/Ar ion sputtering treatment. At higher temperatures, **NHC-2** is decomposed on 2D-Mo_2C due to the reactive Mo sites.

4-CF_3-benzaldehyde undergoes deoxygenation on 2D-Mo_2C at 250 K, resulting in adsorbed 4-CF_3-styrylidene and O formation. In addition, the total O 1s XPS peak areas, from the C-O and Mo-O peaks remained constant, but O atoms shifts from the Mo sites to the C sites as the temperature increases. 4-CF_3-benzaldehyde and 3-CF_3-benzaldehyde are condensed on 2D-Mo_2C/Cu at 200 K. Monolayer chemisorption is achieved at 250 K and the relative intensities of the υ_{sym}(C-CF_3) bands are consistent with the formation of surface alkylidenes.

Conclusions

The main objective of this thesis was to study covalent functionalization of different surfaces, including Pt-group surfaces, metal-supported graphene and two-dimensional (2D) molybdenum carbides, using NHCs. In addition, this thesis also studied the possibility of surface alkylidene formation on 2D-Mo_2C. RAIRS measurements were used to explore covalent bonding between NHCs (**NHC-1** and **NHC-2**) and Pt(111), Ru(0001), Gr/Pt(111), Gr/Ru(0001) and Gr/O/Ru(0001) surfaces. Combined XPS and RAIRS measurements were used to explore **NHC-2** adsorption on 2D-Mo_2C/Cu and 3-CF_3-benzaldehyde and 4-CF_3-benzaldehyde deoxygenation on 2D-Mo_2C/Cu.

First, we studied NHCs ligands on Pt-group surfaces. RAIRS measurements provided evidence of NHC monolayer formation on Pt(111) and Ru(0001). **NHC-1** ligands are generated on Pt(111) at 300 K as evidenced by the appearance of the aromatic CH stretching band at 3064 cm^{-1} and the disappearance of the carbonate O-H vibration at 3355 cm^{-1}. Vibrations at 2975 cm^{-1} (CH_3 asymmetric stretching), 2933 cm^{-1} (CH_3 symmetric stretching) and 2874 cm^{-1} (CH stretching) are removed at 475 K but the aromatic CH band still remains until 515 K. These observations indicate that the isopropyl wings are decomposed on the reactive Pt(111) surface but that the backbone core of **NHC-1** remains intact. **NHC-2** ligands on Pt(111) and Ru(0001) display -CF_3 vibrations including $\upsilon_{sym}(C\text{-}CF_3)$, in-plane $\upsilon_{asym}(CF_3)$ and out-of-plane $\upsilon_{asym}(CF_3)$ stretching. The $\upsilon_{sym}(C\text{-}CF_3)$ and in-plane $\upsilon_{asym}(CF_3)$ modes are RAIRS active if the **NHC-2** is oriented normal to the surface while only the out-of-plane $\upsilon_{asym}(CF_3)$ mode is active for flat-lying **NHC-2**. Carbonate-related vibrations on Pt(111) and Ru(0001) surfaces are removed by 400 K, but all of the -CF_3 vibrations still can be detected. Vertically oriented **NHC-2** are formed on the Pt(111) and Ru(0001) surface but there is also competitive adsorption into flat-lying states. Especically for **NHC-2** on Ru(0001), there is strong signal from a flat-lying state at 400 K. In addition, the removal of the out-of-plane $\upsilon_{asym}(CF_3)$ band on annealing from 400 to 500 K results in an increase in the integrated intensity of the $\upsilon_{sym}(C\text{-}CF_3)$ band, indicating that the flat-lying state of **NHC-2** can conver to a vertical state. The $\upsilon_{sym}(C\text{-}CF_3)$ intensity is used to monitor the thermal stability of the vertically oriented NHC surface ligands. The surface **NHC-2** is detected to 700 K on Pt(111) and to 600 K on Ru(0001).

Next, we studied the functionalization of graphene that was formed on Pt(111) and Ru(0001) surfaces by chemical vapor deposition. It is known that the quasi-freestanding Gr/Pt(111) layer is strongly p-doped whereas the Gr/Ru(0001) layer is strongly n-doped. The interaction of the **NHC-2** with Gr/Pt(111) is stronger than with Gr/Ru(0001). This difference mainly is attributed to the p-doped and n-doped character of the respective systems coupled with the electron-donor character of the NHC. Oxygen intercalation of Gr/Ru(0001) was carried out between 400-600 K. The interaction of **NHC-2** with Gr/O/Ru(0001) is different from that with Gr/Ru(0001) but is similar to that for Gr/Pt(111). Intercalation of oxygen between graphene and Ru(0001) leads to **NHC-2** bonding similar to that for Gr/Pt(111) consistent with the removal of the strong Gr/Ru interaction to form a quasi-freestanding p-doped and wrinkled layer.

As-received 2D-Mo_2C/Cu samples are covered by a poorly defined carbon layer or layers, and exposure to air leads to the formation of oxycarbides. Atomic hydrogen treatment is an effective method to remove carbon contamination but a carbon layer on the surface still remains after atomic hydrogen treatment. O/Ar ion sputtering is an effective method to remove the surface carbon layer. Additional annealing at high temperature (1100 K) is greatly reduces the oxygen content. **NHC-2** interacts weakly with carbon covered 2D-Mo_2C/Cu prepared by atomic hydrogen treatment. In contrast, 2D-Mo_2C/Cu surfaces prepared by O/Ar treatment are reactive to **NHC-2** ligands at 300 K. **NHC-2** is decomposed on 2D-Mo_2C/Cu at higher temperatures. Next, alkylidene functionalization of O/Ar ion sputtered 2D-Mo_2C/Cu was explored. Condensed layers of 4-CF_3-benzaldehyde and 3-CF_3-benzaldehyde molecules are formed on the 2D-Mo_2C/Cu surface at 200 K. 4-CF_3-styrylidene and 3-CF_3-styrylidene ligands together with O atoms are formed on 2D-Mo_2C/Cu when the temperature is increased to 250 K. As the temperature increases, the total XPS signal from O atoms, from the C-O and Mo-O peaks, remains constant, but the Mo-O signal decreases and the C-O signal increases. This observation indicates that a transfer of oxygen from molybdenum to carbon sites occurs. There is no evidence in the literature of such an O transfer on bulk Mo_2C. We conclude that O atoms have an increased mobility on the 2D-Mo_2C surface and O atoms can shift from Mo sites to C sites at higher temperature.

List of Publications

1. Zeng, Y.; Zhang, T.; Narouz, M. R.; Crudden C. M.; McBreen, P. H. Generation and Conversion of an N-Heterocyclic Carbene on Pt(111). *Chemical Communications* **2018**, *54*, 12527–12530. Chapter 2
2. N-Heterocyclic Carbene Formation, Structure and Stability on Pt(111) and Ru(0001). *In preparation*. Chapter 2.
3. Covalent Fuctionalization of Graphene by an N-Heterocyclic Carbene. *In preparation*. Chapter 3.

References

(1) Koy, M.; Bellotti, P.; Das, M.; Glorius, F. N-Heterocyclic Carbenes as Tunable Ligands for Catalytic Metal Surfaces. *Nature Catalysis*. *Journal of the American Chemical Society* **2021**, *4*, 352–363. https://doi.org/10.1038/s41929-021-00607-z.

(2) Zhukhovitskiy, A. v; Mavros, M. G.; Voorhis, T. van; Johnson, J. A. Addressable Carbene Anchors for Gold Surfaces. *Journal of the American Chemical Society* **2013**, *135* (20), 7418–7421. https://doi.org/10.1021/ja401965d.

(3) Crudden, C. M.; Horton, J. H.; Ebralidze, I. I.; Zenkina, O. v.; McLean, A. B.; Drevniok, B.; She, Z.; Kraatz, H. B.; Mosey, N. J.; Seki, T.; Keske, E. C.; Leake, J. D.; Rousina-Webb, A.; Wu, G. Ultra Stable Self-Assembled Monolayers of N-Heterocyclic Carbenes on Gold. *Nature Chemistry* **2014**, *6*, 409–414. https://doi.org/10.1038/nchem.1891.

(4) Hopkinson, M. N.; Richter, C.; Schedler, M.; Glorius, F. An Overview of N-Heterocyclic Carbenes. *Nature* **2014**, *510*, 485–496. https://doi.org/10.1038/nature13384.

(5) Gómez-Suárez, A.; Nelson, D. J.; Nolan, S. P. Quantifying and Understanding the Steric Properties of N-Heterocyclic Carbenes. *Chemical Communications* **2017**, *53* (18), 2650–2660. https://doi.org/10.1039/c7cc00255f.

(6) Weidner, T.; Baio, J. E.; Mundstock, A.; Große, C.; Karthäuser, S.; Bruhn, C.; Siemeling U. NHC-Based Self-Assembled Monolayers on Solid Gold Substrates. *Australian journal of chemistry* **2011**, *64* (8), 1177–1179. https://doi.org/10.1071/CH11173.

(7) Nuzzo, R. G.; Zegarski, B. R.; DuBois, L. H. Fundamental Studies of the Chemisorption of Organosulfur Compounds on Au(111). Implications for Molecular Self-Assembly on Gold Surfaces. *Journal of the American Chemical Society* **1987**, *109* (3), 733–740. https://doi.org/10.1021/ja00237a017.

(8) Vericat, C.; Vela, M. E.; Benitez, G.; Carro, P.; Salvarezza, R. C. Self-Assembled Monolayers of Thiols and Dithiols on Gold: New Challenges for a Well-Known System. *Chemical Society Reviews* **2010**, *39* (5), 1805–1834. https://doi.org/10.1039/b907301a.

(9) Schoenfisch, M. H.; Pemberton, J. E. Air Stability of Alkanethiol Self-Assembled Monolayers on Silver and Gold Surfaces. *Journal of the American Chemical Society* **1998**, *120* (18), 4502–4513. https://doi.org/10.1021/ja974301t.

(10) Li, Y.; Huang, J.; McIver, R. T.; Hemminger, J. C. Characterization of Thiol Self-Assembled Films by Laser Desorption Fourier Transform Mass Spectrometry. *Journal of the American Chemical Society* **1992**, *114* (7), 2428–2432. https://doi.org/10.1021/ja00033a018.

(11) Noh, J.; Kato, H. S.; Kawai, M.; Hara, M. Surface Structure and Interface Dynamics of Alkanethiol Self-Assembled Monolayers on Au(111). *Journal of Physical Chemistry B* **2006**, *110* (6), 2793–2797. https://doi.org/10.1021/jp055538b.

(12) Gooding, J. J.; Ciampi, S. The Molecular Level Modification of Surfaces: From Self-Assembled Monolayers to Complex Molecular Assemblies. *Chemical Society Reviews* **2011**, *40* (5), 2704–2718. https://doi.org/10.1039/c0cs00139b.

(13) Wang, G.; Rühling, A.; Amirjalayer, S.; Knor, M.; Ernst, J. B.; Richter, C.; Gao, H.; Timmer, A.; Gao, H.; Doltsinis, N. L.; Glorius, F.; Fuchs, H. Ballbot-Type Motion of N-Heterocyclic Carbenes on Gold Surfaces

Ballbot-Type Motion of N-Heterocyclic Carbenes on Gold Surfaces. *Nature Chemistry* **2017**, *9*, 152–156. https://doi.org/10.1038/NCHEM.2622.

(14) Lovat, G.; Doud, E. A.; Lu, D.; Kladnik, G.; Inkpen, M. S.; Steigerwald, M. L.; Cvetko, D.; Hybertsen, M. S.; Morgante, A.; Venkataraman, L. Chemical Science Resolution Spectroscopy. *Chemical Science* **2019**, *10*, 930–935. https://doi.org/10.1039/C8SC03502D.

(15) Larrea, C. R.; Baddeley, C. J.; Narouz, M. R.; Mosey, N. J.; Horton, J. H.; Crudden, C. M. N-Heterocyclic Carbene Self-Assembled Monolayers on Copper and Gold: Dramatic Effect of Wingtip Groups on Binding, Orientation and Assembly. *ChemPhysChem* **2017**, *18* (24), 3536–3539. https://doi.org/10.1002/cphc.201701045.

(16) Wu, C. Y.; Wolf, W. J.; Levartovsky, Y.; Bechtel, H. A.; Martin, M. C.; Toste, F. D.; Gross, E. High-Spatial-Resolution Mapping of Catalytic Reactions on Single Particles. *Nature* **2017**, *541* (7638), 511–515. https://doi.org/10.1038/nature20795.

(17) Levratovsky, Y.; Gross, E. High Spatial Resolution Mapping of Chemically-Active Self-Assembled N-Heterocyclic Carbenes on Pt Nanoparticles. *Faraday Discussions* **2016**, *188*, 345–353. https://doi.org/10.1039/c5fd00194c.

(18) Zeng, Y.; Zhang, T.; Narouz, M. R.; Crudden C. M.; McBreen, P. H. Generation and Conversion of an N-Heterocyclic Carbene on Pt(111). *Chemical Communications* **2018**, *54*, 12527–12530. https://doi.org/10.1039/C8CC06894A.

(19) Wang, B.; König, M.; Bromley, C. J.; Yoon, B.; Treanor, M. J.; Garrido Torres, J. A.; Caffio, M.; Grillo, F.; Früchtl, H.; Richardson, N. V.; Esch, F.; Heiz, U.; Landman, U.; Schaub, R. Ethene to Graphene: Surface Catalyzed Chemical Pathways, Intermediates, and Assembly. *Journal of Physical Chemistry C* **2017**, *121* (17), 9413–9423. https://doi.org/10.1021/acs.jpcc.7b01999.

(20) Cazzanelli, E.; Caruso, T.; Castriota, M.; Marino, A. R.; Politano, A.; Chiarello, G.; Giarola, M.; Mariotto, G. Spectroscopic Characterization of Graphene Films Grown on Pt(111) Surface by Chemical Vapor Deposition of Ethylene. *Journal of Raman Spectroscopy* **2013**, *44* (10), 1393–1397. https://doi.org/10.1002/jrs.4285.

(21) Politano, A.; Borca, B.; Minniti, M.; Hinarejos, J. J.; Vázquez De Parga, A. L.; Farías, D.; Miranda, R. Helium Reflectivity and Debye Temperature of Graphene Grown Epitaxially on Ru(0001). *Physical Review B* **2011**, *84* (3), 23–25. https://doi.org/10.1103/PhysRevB.84.035450.

(22) Borca, B.; Barja, S.; Garnica, M.; Minniti, M.; Politano, A.; Rodriguez-García, J. M.; Hinarejos, J. J.; Farías, D.; Vázquez De Parga, A. L.; Miranda, R. Electronic and Geometric Corrugation of Periodically Rippled, Self-Nanostructured Graphene Epitaxially Grown on Ru(0001). *New Journal of Physics* **2010**, *12* (9), 093018. https://doi.org/10.1088/1367-2630/12/9/093018.

(23) You, A.; Be, M. A. Y.; In, I. Atmospheric Stability and Doping Protection of Noble-Metal Intercalated Graphene on Ni(111). *Applied Physics Letters* **2011**, *98*, 122111. https://doi.org/10.1063/1.3565248.

(24) Miniussi, E.; Pozzo, M.; Baraldi, A.; Vesselli, E.; Zhan, R. R.; Comelli, G.; Menteş, T. O.; Niño, M. A.; Locatelli, A.; Lizzit, S.; Alfè, D. Thermal Stability of Corrugated Epitaxial Graphene Grown on Re(0001). *Physical Review Letters* **2011**, *106* (21), 216101. https://doi.org/10.1103/PhysRevLett.106.216101.

(25) Eom, D.; Prezzi, D.; Rim, K. T.; Zhou, H.; Lefenfeld, M.; Xiao, S.; Nuckolls, C.; Hybertsen, M. S.; Heinz, T. F.; Flynn, G. W. Structure and Electronic Properties of Graphene Nanoislands on Co(0001). *Nano Letters* **2009**, *9* (8), 2844–2848. https://doi.org/10.1021/nl900927f.

(26) Sicot, M.; Leicht, P.; Zusan, A.; Bouvron, S.; Zander, O.; Weser, M.; Dedkov, Y. S.; Horn, K.; Fonin, M. Size-Selected Epitaxial Nanoislands underneath Graphene Moiré on Rh(111). *ACS Nano* **2012**, *6* (1), 151–158. https://doi.org/10.1021/nn203169j.

(27) Murata, Y.; Starodub, E.; Kappes, B. B.; Ciobanu, C. V.; Bartelt, N. C.; McCarty, K. F.; Kodambaka, S. Orientation-Dependent Work Function of Graphene on Pd(111). *Applied Physics Letters* **2010**, *97*, 143114. https://doi.org/10.1063/1.3495784.

(28) Sutter, P.; Sadowski, J. T.; Sutter, E. Graphene on Pt(111): Growth and Substrate Interaction. *Physical Review B* **2009**, *80* (24), 1–10. https://doi.org/10.1103/PhysRevB.80.245411.

(29) Coraux, J.; N'Diaye, A. T.; Busse, C.; Michely, T. Structural Coherency of Graphene on Ir(111). *Nano Letters* **2008**, *8* (2), 565–570. https://doi.org/10.1021/nl0728874.

(30) Gao, L.; Guest, J. R.; Guisinger, N. P. Epitaxial Graphene on Cu (111). *Nano Letters* **2010**, *10* (9), 3512–3516. https://doi.org/10.1021/nl1016706.

(31) Kiraly, B.; Iski, E. V; Mannix, A. J.; Fisher, B. L.; Hersam, M. C.; Guisinger, N. P. Solid-Source Growth and Atomic-Scale Characterization of Graphene on Ag(111). *Nature Communications* **2013**, *4* (1), 1–7. https://doi.org/10.1038/ncomms3804.

(32) Dahal, A.; Batzill, M. Graphene-Nickel Interfaces: A Review. *Nanoscale* **2014**, *6*, 2548–2562. https://doi.org/10.1039/c3nr05279f.

(33) Zhao, G.; Li, X.; Huang, M.; Zhen, Z.; Zhong, Y.; Chen, Q.; Zhao, X.; He, Y.; Hu, R.; Yang, T.; Zhang, R.; Li, C.; Kong, J.; Xu, J. bin; Ruoff, R. S.; Zhu, H. The Physics and Chemistry of Graphene-on-Surfaces. *Chemical Society Reviews* **2017**, *46*, 4417–4449. https://doi.org/10.1039/c7cs00256d.

(34) Zhu, L.; Ding, F. How the Moiré Superstructure Determines the Formation of Highly Stable Graphene Quantum Dots on Ru(0001) Surface. *Nanoscale Horizons* **2019**, *4* (3), 625–633. https://doi.org/10.1039/c8nh00383a.

(35) Pisarra, M.; Diáz, C.; Martín, F. Defect Formation in a Graphene Overlayer on Ruthenium under High Pressure. *Physical Review B* **2020**, *102* (7), 5406. https://doi.org/10.1103/PhysRevB.102.075406.

(36) Wang, B.; Günther, S.; Wintterlin, J.; Bocquet, M. L. Periodicity, Work Function and Reactivity of Graphene on Ru(0001) from First Principles. *New Journal of Physics* **2010**, *12* (4), 3041. https://doi.org/10.1088/1367-2630/12/4/043041.

(37) Navarro, J. J.; Leret, S.; Calleja, F.; Stradi, D.; Black, A.; Bernardo-Gavito, R.; Garnica, M.; Granados, D.; Vázquez De Parga, A. L.; Pérez, E. M.; Miranda, R. Organic Covalent Patterning of Nanostructured Graphene with Selectivity at the Atomic Level. *Nano Letters* **2016**, *16* (1), 355–361. https://doi.org/10.1021/acs.nanolett.5b03928.

(38) Zhu, L.; Ding, F. How the Moiré Superstructure Determines the Formation of Highly Stable Graphene Quantum Dots on Ru(0001) Surface. *Nanoscale Horizons* **2019**, *4* (3), 625–633. https://doi.org/10.1039/c8nh00383a.

(39) Iannuzzi, M.; Kalichava, I.; Ma, H.; Leake, S. J.; Zhou, H.; Li, G.; Zhang, Y.; Bunk, O.; Gao, H.; Hutter, J.; Willmott, P. R.; Greber, T. Moiré Beatings in Graphene on Ru(0001). *Physical Review B* **2013**, *88* (12), 1–5. https://doi.org/10.1103/PhysRevB.88.125433.

(40) Sutter, P.; Albrecht, P.; Tong, X.; Sutter, E. Mechanical Decoupling of Graphene from Ru(0001) by Interfacial Reaction with Oxygen. *Journal of Physical Chemistry C* **2013**, *117* (12), 6320–6324. https://doi.org/10.1021/jp400838j.

(41) Wu, G.; Tang, X.; Meyyappan, M.; Lai, K. W. C. Doping Effects of Surface Functionalization on Graphene with Aromatic Molecule and Organic Solvents. *Applied Surface Science* **2017**, *425*, 713–721. https://doi.org/10.1016/j.apsusc.2017.07.048.

(42) Zhang, Y.; Fu, Q.; Cui, Y.; Mu, R.; Jin, L.; Bao, X. Enhanced Reactivity of Graphene Wrinkles and Their Function as Nanosized Gas Inlets for Reactions under Graphene. *Physical Chemistry Chemical Physics* **2013**, *15* (43), 19042–19048. https://doi.org/10.1039/c3cp52115j.

(43) Johánek, V.; Cushing, G. W.; Navin, J. K.; Harrison, I. Real-Time Observation of Graphene Oxidation on Pt(111) by Low-Energy Electron Microscopy. *Surface Science* **2016**, *644*, 165–169. https://doi.org/10.1016/j.susc.2015.08.042.

(44) Yao, Y.; Fu, Q.; Zhang, Y. Y.; Weng, X.; Li, H.; Chend, M.; Jin, L.; Dong, A.; Mu, R.; Jiang, P.; Liu, L.; Bluhm, H.; Liu, Z.; Zhang, S. B.; Bao, X. Graphene Cover-Promoted Metal-Catalyzed Reactions. *Proceedings of the National Academy of Sciences of the United States of America* **2014**, *111* (48), 17023–17028. https://doi.org/10.1073/pnas.1416368111.

(45) Telieps, W.; Bauer, E. Low Energy Electron Microscopy (LEEM). The Structure of Surfaces II **1988**, 53–57. https://doi.org/10.1007/978-3-642-73343-7_10.

(46) Low, J.; Yu, J.; Ho, W. Graphene-Based Photocatalysts for CO_2 Reduction to Solar Fuel. *Journal of Physical Chemistry Letters* **2015**, 6 (21), 4244–4251. https://doi.org/10.1021/acs.jpclett.5b01610.

(47) Tit, N.; Said, K.; Mahmoud, N. M.; Kouser, S.; Yamani, Z. H. Ab-Initio Investigation of Adsorption of CO and CO_2 Molecules on Graphene: Role of Intrinsic Defects on Gas Sensing. *Applied Surface Science* **2017**, *394* (1), 219–230. https://doi.org/10.1016/j.apsusc.2016.10.052.

(48) Yun, S.; Lee, H.; Lee, W. E.; Park, H. S. Multiscale Textured, Ultralight Graphene Monoliths for Enhanced CO_2 and SO_2 Adsorption Capacity. *Fuel* **2016**, *174*, 36–42. https://doi.org/10.1016/j.fuel.2016.01.068.

(49) Jana, M.; Saha, S.; Khanra, P.; Samanta, P.; Koo, H.; Murmu, N. C.; Kuila, T. Non-Covalent Functionalization of Reduced Graphene Oxide Using Sulfanilic Acid Azocromotrop and Its Application as a Supercapacitor Electrode Material. *Journal of Materials Chemistry A* **2015**, *3* (14), 7323–7331. https://doi.org/10.1039/c4ta07009g.

(50) Demers-Carpentier, V.; Rasmussen, A. M. H.; Goubert, G.; Ferrighi, L.; Dong, Y.; Lemay, J. C.; Masini, F.; Zeng, Y.; Hammer, B.; McBreen, P. H. Stereodirection of an α-Ketoester at Sub-Molecular Sites on Chirally Modified Pt(111): Heterogeneous Asymmetric Catalysis. *Journal of the American Chemical Society* **2013**, *135* (27), 9999–10002. https://doi.org/10.1021/ja403955k.

(51) Yang, K.; Xiao, W. D.; Jiang, Y. H.; Zhang, H. G.; Liu, L. W.; Mao, J. H.; Zhou, H. T.; Du, S. X.; Gao, H. J. Molecule-Substrate Coupling between Metal Phthalocyanines and Epitaxial Graphene Grown on Ru(0001) and Pt(111). *Journal of Physical Chemistry C* **2012**, *116* (26), 14052–14056. https://doi.org/10.1021/jp304068a.

(52) Mao, J.; Zhang, H.; Jiang, Y.; Pan, Y.; Gao, M.; Xiao, W.; Gao, H. J. Tunability of Supramolecular Kagome Lattices of Magnetic Phthalocyanines Using Graphene-Based Moiré Patterns as Templates. *Journal of the American Chemical Society* **2009**, *131* (440), 14136–14137. https://doi.org/10.1021/ja904907z.

(53) Stradi, D.; Garnica, M.; Díaz, C.; Calleja, F.; Barja, S.; Martín, N.; Alcamí, M.; Vazquez De Parga, A. L.; Miranda, R.; Martín, F. Controlling the Spatial Arrangement of Organic Magnetic Anions Adsorbed on Epitaxial Graphene on Ru(0001). *Nanoscale* **2014**, *6* (24), 15271–15279. https://doi.org/10.1039/c4nr02917h.

(54) Lauffer, P.; Emtsev, K. v.; Graupner, R.; Seyller, T.; Ley, L. Molecular and Electronic Structure of PTCDA on Bilayer Graphene on SiC(0001) Studied with Scanning Tunneling Microscopy. In *Physica Status Solidi (B) Basic Research* **2008**, *245*, 2064–2067. https://doi.org/10.1002/pssb.200879615.

(55) Wang, Q. H.; Hersam, M. C. Room-Temperature Molecular-Resolution Characterization of Self-Assembled Organic Monolayers on Epitaxial Graphene. *Nature Chemistry* **2009**, *1* (3), 206–211. https://doi.org/10.1038/nchem.212.

(56) Niyogi, S.; Bekyarova, E.; Itkis, M. E.; Zhang, H.; Shepperd, K.; Hicks, J.; Sprinkle, M.; Berger, C.; Lau, C. N.; Walt, A.; Conrad, E. H.; Haddon, R. C. Spectroscopy of Covalently Functionalized Graphene. *Nano Letters* **2010**, *10* (10) 4061–4066. https://doi.org/10.1021/nl1021128.

(57) Park, J.; Yan, M. Covalent Functionalization of Graphene with Reactive Intermediates. *Accounts of Chemical Research* **2013**, *46* (1), 181–189. https://doi.org/10.1021/ar300172h.

(58) Zhong, X.; Jin, J.; Li, S.; Niu, Z.; Hu, W.; Li, R.; Ma, J. Aryne Cycloaddition: Highly Efficient Chemical Modification of Graphene. *Chemical Communications* **2010**, *46* (39), 7340–7342. https://doi.org/10.1039/c0cc02389b.

(59) Strom, T. A.; Dillon, E. P.; Hamilton, C. E.; Barron, A. R. Nitrene Addition to Exfoliated Graphene: A One-Step Route to Highly Functionalized Graphene. *Chemical Communications* **2010**, 46, 4097–4099. https://doi.org/10.1039/c001488e.

(60) Sarkar, S.; Bekyarova, E.; Niyogi, S.; Haddon, R. C. Diels-Alder Chemistry of Graphite and Graphene: Graphene as Diene and Dienophile. *Journal of the American Chemical Society* **2011**, 133 (10), 3324–3327. https://doi.org/10.1021/ja200118b.

(61) Sainsbury, T.; Passarelli, M.; Naftaly, M.; Gnaniah, S.; Spencer, S. J.; Pollard, A. J. Covalent Carbene Functionalization of Graphene: Toward Chemical Band-Gap Manipulation. *ACS Applied Materials & Interfaces* **2016**, *8* (7), 4870–4877. https://doi.org/10.1021/acsami.5b10525.

(62) Ambrosio, G.; Brown, A.; Daukiya, L.; Drera, G.; di Santo, G.; Petaccia, L.; de Feyter, S.; Sangaletti, L.; Pagliara, S. Impact of Covalent Functionalization by Diazonium Chemistry on the Electronic Properties of Graphene on SiC. *Nanoscale* **2020**, *12*, 9032–9037. https://doi.org/10.1039/d0nr01186j.

(63) Greenwood, J.; Phan, T. H.; Fujita, Y.; Li, Z.; Ivasenko, O.; Vanderlinden, W.; van Gorp, H.; Frederickx, W.; Lu, G.; Tahara, K.; Tobe, Y.; Uji-I, H.; Mertens, S. F. L.; de Feyter, S. Covalent Modification of Graphene and Graphite Using Diazonium Chemistry: Tunable Grafting and Nanomanipulation. *ACS Nano* **2015**, *9* (5), 5520–5535. https://doi.org/10.1021/acsnano.5b01580.

(64) Tang, Q.; Jiang, D. E. Computational Insight into the Covalent Organic-Inorganic Interface. *Chemistry of Materials*. **2016**, *28* (17), 5976–5988. https://doi.org/10.1021/acs.chemmater.6b01740.

(65) Chae, S.; Le, T. H.; Park, C. S.; Choi, Y.; Kim, S.; Lee, U.; Heo, E.; Lee, H.; Kim, Y. A.; Kwon, O. S.; Yoon, H. Anomalous Restoration of Sp^2 Hybridization in Graphene Functionalization. *Nanoscale* **2020**, *12* (25), 13351–13359. https://doi.org/10.1039/d0nr03422c.

(66) VahidMohammadi, A.; Rosen, J.; Gogotsi, Y. The World of Two-Dimensional Carbides and Nitrides (MXenes). *Science* **2021**, 372 (6547), https://doi.org/10.1126/science.abf1581.

(67) Halim, J.; Kota, S.; Lukatskaya, M. R.; Naguib, M.; Zhao, M. Q.; Moon, E. J.; Pitock, J.; Nanda, J.; May, S. J.; Gogotsi, Y.; Barsoum, M. W. Synthesis and Characterization of 2D Molybdenum Carbide (MXene). *Advanced Functional Materials* **2016**, *26* (18), 3118-3127. https://doi.org/10.1002/adfm.201505328.

(68) Verger, L.; Xu, C.; Natu, V.; Cheng, H. M.; Ren, W.; Barsoum, M. W. Overview of the Synthesis of MXenes and Other Ultrathin 2D Transition Metal Carbides and Nitrides. *Current Opinion in Solid State and Materials Science* **2019**, *23* (3), 149–163. https://doi.org/10.1016/j.cossms.2019.02.001.

(69) Chaitoglou, S.; Giannakopoulou, T.; Tsoutsou, D.; Vavouliotis, A.; Trapalis, C.; Dimoulas, A. Direct versus Reverse Vertical Two-Dimensional Mo_2C/Graphene Heterostructures for Enhanced Hydrogen Evolution Reaction Electrocatalysis. *Nanotechnology* **2019**, *30* (41), 5404. https://doi.org/10.1088/1361-6528/ab3155.

(70) Geng, D. C.; Zhao, X. X.; Chen, Z. X.; Sun, W. W.; Fu, W.; Chen, J. Y.; Liu, W.; Zhou, W.; Loh, K. P. Direct Synthesis of Large-Area 2D Mo_2C on in Situ Grown Graphene. *Advanced Materials* **2017**, *29* (35), 1700072. https://doi.org/10.1002/adma.201700072.

(71) Xu, C.; Wang, L.; Liu, Z.; Chen, L.; Guo, J.; Kang, N.; Ma, X. L.; Cheng, H. M.; Ren, W. Large-Area High-Quality 2D Ultrathin Mo_2C Superconducting Crystals. *Nature Materials* **2015**, *14* (11), 1135–1141. https://doi.org/10.1038/nmat4374.

(72) Turker, F.; Caylan, O. R.; Mehmood, N.; Kasirga, T. S.; Sevik, C.; Cambaz Buke, G. CVD Synthesis and Characterization of Thin Mo_2C Crystals. *Journal of the American Ceramic Society* **2020**, *103* (10), 5586–5593. https://doi.org/10.1111/jace.17317.

(73) Cumpson, P. J.; Seah, M. P. Elastic Scattering Corrections in AES and XPS. II. Estimating Attenuation Lengths and Conditions Required for Their Valid Use in Overlayer/Substrate Experiments. *Surface and Interface Analysis* **1997**, *25* (6), 430–446. https://doi.org/10.1002/(SICI)1096-9918(199706)25:6<430::AID-SIA254>3.0.CO;2-7.

(74) Seah, M. P.; Dench, W. A.; Quantitative Electron Spectroscopy of Surfaces: A Standard Data Base for Electron Inelastic Mean Free Paths in Solids. *Surface and interface analysis* **1979**, 1 (1), 2–11. https://doi.org/10.1002/sia.740010103.

(75) Humblot, V.; Pradier, C. M. RAIRS under Ultrahigh Vacuum Conditions on Metal Surfaces. In Biointerface Characterization by Advanced IR Spectroscopy **2011**, 1-26. https://doi.org/10.1016/B978-0-444-53558-0.00001-1.

(76) Sundaraganesan, N.; Illakiamani, S.; Meganathan, C.; Joshua, B. D. Vibrational Spectroscopy Investigation Using Ab Initio and Density Functional Theory Analysis on the Structure of 3-Aminobenzotrifluoride. *Spectrochimica Acta - Part A: Molecular and Biomolecular Spectroscopy* **2007**, *67* (1), 214–224. https://doi.org/10.1016/j.saa.2006.07.004.

(77) Gunasekaran, S.; Seshadri, S.; Muthu, S.; Kumaresan, S.; Arunbalaji, R. Vibrational Spectroscopy Investigation Using Ab Initio and Density Functional Theory on P-Anisaldehyde. *Spectrochimica Acta - Part A: Molecular and Biomolecular Spectroscopy* **2008**, *70* (3), 550–556. https://doi.org/10.1016/j.saa.2007.07.050.

(78) Smith, C. A.; Narouz, M. R.; Lummis, P. A.; Singh, I.; Nazemi, A.; Li, C. H.; Crudden, C. M. N-Heterocyclic Carbenes in Materials Chemistry. *Chemical Reviews* **2019**, *119* (8), 4986–5056. https://doi.org/10.1021/acs.chemrev.8b00514.

(79) Zhukhovitskiy, A. v.; MacLeod, M. J.; Johnson, J. A. Carbene Ligands in Surface Chemistry: From Stabilization of Discrete Elemental Allotropes to Modification of Nanoscale and Bulk Substrates. *Chemical Reviews* **2015**, *115* (20), 11503–11532. https://doi.org/10.1021/acs.chemrev.5b00220.

(80) Siaj, M.; McBreen, P. H. Creating, Varying, and Growing Single-Site Molecular Contacts. *Science* **2005**, *309* (5734), 588–590. https://doi.org/10.1126/science.1113667.

(81) Mieres-Perez, J.; Lucht, K.; Trosien, I.; Sander, W.; Sanchez-Garcia, E.; Morgenstern, K. Controlling Reactivity-Real-Space Imaging of a Surface Metal Carbene. *Journal of the American Chemical Society* **2021**, *143* (12), 4653–4660. https://doi.org/10.1021/jacs.0c12995.

(82) Matena, M.; Riehm, T.; Stöhr, M.; Jung, T. A.; Gade, L. H. Transforming Surface Coordination Polymers into Covalent Surface Polymers: Linked Polycondensed Aromatics through Oligomerization of N-Heterocyclic Carbene Intermediates. *Angewandte Chemie - International Edition* **2008**, *47* (13), 2414–2417. https://doi.org/10.1002/anie.200704072.

(83) Khramov, D. M.; Lynch, V. M.; Bielawski, C. W. N-Heterocyclic Carbene-Transition Metal Complexes : Spectroscopic and Crystallographic Analyses of π-Back-Bonding Interactions. **2007**, 6042–6049. https://doi.org/10.1021/om700591z.

(84) Gaggioli, C. A.; Bistoni, G.; Ciancaleoni, G.; Tarantelli, F.; Belpassi, L.; Belanzoni, P. Modulating the Bonding Properties of N-Heterocyclic Carbenes (NHCs): A Systematic Charge-Displacement Analysis. *Chemistry - A European Journal* **2017**, *23* (31), 7558–7569. https://doi.org/10.1002/chem.201700638.

(85) Herrmann, W. A. N-Heterocyclic Carbenes: A New Concept in Organometallic Catalysis. *Angewandte Chemie - International Edition* **2002**, *41* (8), 1290–1309. https://doi.org/10.1002/1521-3773(20020415)41:8<1290::AID-ANIE1290>3.0.CO;2-Y.

(86) Arduengo, A. J. Looking for Stable Carbenes: The Difficulty in Starting Anew. *Accounts of Chemical Research* **1999**, *32* (11), 913–921. https://doi.org/10.1021/ar980126p.

(87) Huynh, H. V. Electronic Properties of N-Heterocyclic Carbenes and Their Experimental Determination. *Chemical Reviews* **2018**, *118* (19), 9457–9492. https://doi.org/10.1021/acs.chemrev.8b00067.

(88) Soleilhavoup, M.; Bertrand, G. Stable Carbenes, Nitrenes, Phosphinidenes, and Borylenes: Past and Future. *Chem* **2020**, *6* (6), 1275–1282. https://doi.org/10.1016/j.chempr.2020.04.015.

(89) Crudden, C. M.; Horton, J. H.; Narouz, M. R.; Li, Z.; Smith, C. A.; Munro, K.; Baddeley, C. J.; Larrea, C. R.; Drevniok, B.; Thanabalasingam, B.; McLean, A. B.; Zenkina, O. v.; Ebralidze, I. I.; She, Z.; Kraatz, H. B.; Mosey, N. J.; Saunders, L. N.; Yagi, A. Simple Direct Formation of Self-Assembled N-Heterocyclic Carbene Monolayers on Gold and Their Application in Biosensing. *Nature Communications* **2016**, *7*, 1–7. https://doi.org/10.1038/ncomms12654.

(90) Mo, H.; Amirjalayer, S.; Glorius, F.; Fuchs, H. Elucidating the Binding Modes of N-Heterocyclic Carbenes on a Gold Surface. *Journal of the American Chemical Society* **2018**, 140 (38), 11889–11892. https://doi.org/10.1021/jacs.8b06180.

(91) Lovat, G.; Doud, E. A.; Lu, D.; Kladnik, G.; Inkpen, M. S.; Steigerwald, M. L.; Cvetko, D.; Hybertsen, M. S.; Morgante, A.; Roy, X.; Venkataraman, L. Determination of the Structure and Geometry of N-Heterocyclic Carbenes on Au(111) Using High-Resolution Spectroscopy. *Chemical Science* **2019**, *10* (3), 930–935. https://doi.org/10.1039/c8sc03502d.

(92) Jiang, L.; Zhang, B.; Médard, G.; Seitsonen, A. P.; Haag, F.; Allegretti, F.; Reichert, J.; Kuster, B.; Barth, J. v.; Papageorgiou, A. C. N-Heterocyclic Carbenes on Close-Packed Coinage Metal Surfaces: Bis-

Carbene Metal Adatom Bonding Scheme of Monolayer Films on Au, Ag and Cu. *Chemical Science* **2017**, *8* (12), 8301–8308. https://doi.org/10.1039/c7sc03777e.

(93) Chang, K.; Chen, J. G.; Lu, Q.; Cheng, M. Quantum Mechanical Study of N-Heterocyclic Carbene Adsorption on Au Surfaces. *The Journal of Physical Chemistry A* **2017**, *121* (13), 2674–2 https://doi.org/10.1021/acs.jpca.7b01153.

(94) Crasto De Lima, F.; Fazzio, A.; McLean, A. B.; Miwa, R. H. Simulations of X-Ray Absorption Spectroscopy and Energetic Conformation of N-Heterocyclic Carbenes on Au(111). *Physical Chemistry Chemical Physics* **2020**, *22* (37), 21504–21511. https://doi.org/10.1039/d0cp04240d.

(95) Wróbel, M.; Żaba, T.; Sauter, E.; Krawiec, M.; Sobczuk, J.; Terfort, A.; Zharnikov, M.; Cyganik, P. Thermally Stable and Highly Conductive SAMs on Ag Substrate—The Impact of the Anchoring Group. *Advanced Electronic Materials* **2021**, *7* (2), 2000947. https://doi.org/10.1002/aelm.202000947.

(96) Amirjalayer, S.; Bakker, A.; Freitag, M.; Glorius, F.; Fuchs, H. Cooperation of N-Heterocyclic Carbenes on a Gold Surface. *Angewandte Chemie - International Edition* **2020**, *59* (47), 21230–21235. https://doi.org/10.1002/anie.202010634.

(97) Dery, S.; Kim, S.; Tomaschun, G.; Berg, I.; Feferman, D.; Cossaro, A.; Verdini, A.; Floreano, L.; Klüner, T.; Toste, F. D.; Gross, E. Elucidating the Influence of Anchoring Geometry on the Reactivity of NO_2-Functionalized N-Heterocyclic Carbene Monolayers. *Journal of Physical Chemistry Letters* **2019**, *10* (17), 5099–5104. https://doi.org/10.1021/acs.jpclett.9b01808.

(98) Dery, S.; Berg, I.; Kim, S.; Cossaro, A.; Verdini, A.; Floreano, L.; Toste, F. D.; Gross, E. Strong Metal-Adsorbate Interactions Increase the Reactivity and Decrease the Orientational Order of OH-Functionalized N-Heterocyclic Carbene Monolayers. *Langmuir* **2020**, *36* (3), 697–703. https://doi.org/10.1021/acs.langmuir.9b02401.

(99) Cao, Z.; Derrick, J. S.; Xu, J.; Gao, R.; Gong, M.; Nichols, E. M.; Smith, P. T.; Liu, X.; Wen, X.; Copéret, C.; Chang, C. J. Chelating N-Heterocyclic Carbene Ligands Enable Tuning of Electrocatalytic CO_2 Reduction to Formate and Carbon Monoxide: Surface Organometallic Chemistry. *Angewandte Chemie - International Edition* **2018**, *57* (18), 4981–4985. https://doi.org/10.1002/anie.201800367.

(100) Amit, E.; Dery, S.; Kim, S.; Roy, A.; Hu, Q.; Toste, F. D.; Gross, E. Electrochemical Deposition of Addressable N-Heterocyclic Carbene Monolayers. *Physical Chemistry* **2020**. https://doi.org/10.26434/chemrxiv.11522418.v1.

(101) Deng, C.; Chen, J.; Tang, Q. Theoretical Investigation on the Adsorption and Interface Bonding between N-Heterocyclic Carbenes and Metal Surfaces. *Journal of Physical Chemistry C* **2021**, *125* (8), 4489–4497. https://doi.org/10.1021/acs.jpcc.0c09899.

(102) Adhikari, B.; Meng, S.; Fyta, M. Carbene-Mediated Self-Assembly of Diamondoids on Metal Surfaces. **2016**, 8966–8975. https://doi.org/10.1039/c5nr08709k.

(103) Knecht, P.; Zhang, B.; Reichert, J.; Duncan, D. A.; Schwarz, M.; Haag, F.; Ryan, P. T. P.; Lee, T. L.; Deimel, P. S.; Feulner, P.; Allegretti, F.; Auwärter, W.; Médard, G.; Seitsonen, A. P.; Barth, J. v.; Papageorgiou, A. C. Assembly and Manipulation of a Prototypical N-Heterocyclic Carbene with a Metalloporphyrin Pedestal on a Solid Surface. *Journal of the American Chemical Society* **2021**, *143* (11), 4433–4439. https://doi.org/10.1021/jacs.1c01229.

(104) Kang, S.; Byeon, S. E.; Yoon, H. J. N-Heterocyclic Carbene Anchors in Electronics Applications. *Bulletin of the Korean Chemical Society* **2021**, *42* (5), 712–723. https://doi.org/10.1002/bkcs.12261.

(105) An, Y. Y.; Yu, J. G.; Han, Y. F. Recent Advances in the Chemistry of N-Heterocyclic-Carbene-Functionalized Metal-Nanoparticles and Their Applications. *Chinese Journal of Chemistry* **2019**, *37* (1), 76–87. https://doi.org/10.1002/cjoc.201800450.

(106) Cerezo-Navarrete, C.; Lara, P.; Martínez-Prieto, L. M. Organometallic Nanoparticles Ligated by NHCS: Synthesis, Surface Chemistry and Ligand Effects. *Catalysts* **2020**, 10 (10), 1144. https://doi.org/10.3390/catal10101144.

(107) Lara, P.; Rivada-Wheelaghan, O.; Conejero, S.; Poteau, R.; Philippot, K.; Chaudret, B. Ruthenium Nanoparticles Stabilized by N-Heterocyclic Carbenes: Ligand Location and Influence on Reactivity. *Angewandte Chemie - International Edition* **2011**, *50* (50), 12080–12084. https://doi.org/10.1002/anie.201106348.

(108) Ruiz-varilla, A. M.; Baquero, E. A.; Chaudret, B.; Jesús, E. de; Gonzalez, C. Water-Soluble NHC-Stabilized Platinum Nanoparticles as Recoverable Catalysts for Hydrogenation in Water. *Catalysis Science & Technology* **2020,** 10 (9), 2874–2881. https://doi.org/10.1039/D0CY00481B.

(109) Valero, M.; Bouzouita, D.; Palazzolo, A.; Atzrodt, J.; Dugave, C.; Tricard, S.; Feuillastre, S.; Pieters, G.; Chaudret, B.; Derdau, V. NHC-Stabilized Iridium Nanoparticles as Catalysts in Hydrogen Isotope Exchange Reactions of Anilines. *Angewandte Chemie - International Edition* **2020**, *59* (9), 3517–3522. https://doi.org/10.1002/anie.201914369.

(110) Ernst, J. B.; Muratsugu, S.; Wang, F.; Tada, M.; Glorius, F. Tunable Heterogeneous Catalysis: N-Heterocyclic Carbenes as Ligands for Supported Heterogeneous Ru/K-Al_2O_3 Catalysts to Tune Reactivity and Selectivity. *Journal of the American Chemical Society* **2016**, *138* (34), 10718–10721. https://doi.org/10.1021/jacs.6b03821.

(111) Ernst, J. B.; Schwermann, C.; Yokota, G. I.; Tada, M.; Muratsugu, S.; Doltsinis, N. L.; Glorius, F. Molecular Adsorbates Switch on Heterogeneous Catalysis: Induction of Reactivity by N-Heterocyclic Carbenes. *Journal of the American Chemical Society* **2017**, *139* (27), 9144–9147. https://doi.org/10.1021/jacs.7b05112.

(112) Martínez-Prieto, L. M.; Ferry, A.; Rakers, L.; Richter, C.; Lecante, P.; Philippot, K.; Chaudret, B.; Glorius, F. Long-Chain NHC-Stabilized Ru NPs as Versatile Catalysts for One-Pot Oxidation/Hydrogenation Reactions. *Chemical Communications* **2016**, *52* (26), 4768–4771. https://doi.org/10.1039/c6cc01130f.

(113) Bouzouita, D.; Asensio, J. M.; Pfeifer, V.; Palazzolo, A.; Lecante, P.; Pieters, G.; Feuillastre, S.; Tricard, S.; Chaudret, B. Chemoselective H/D Exchange Catalyzed by Nickel Nanoparticles Stabilized by N-Heterocyclic Carbene Ligands. *Nanoscale* **2020**, *12* (29), 15736–15742. https://doi.org/10.1039/d0nr04384b.

(114) Palazzolo, A.; Naret, T.; Daniel-Bertrand, M.; Buisson, D. A.; Tricard, S.; Lesot, P.; Coppel, Y.; Chaudret, B.; Feuillastre, S.; Pieters, G. Tuning the Reactivity of a Heterogeneous Catalyst Using N-Heterocyclic Carbene Ligands for C−H Activation Reactions. *Angewandte Chemie - International Edition* **2020**, *59* (47), 20879–20884. https://doi.org/10.1002/anie.202009258.

(115) Martinez-Espinar, F.; Blondeau, P.; Nolis, P.; Chaudret, B.; Claver, C.; Castillón, S.; Godard, C. NHC-Stabilised Rh Nanoparticles: Surface Study and Application in the Catalytic Hydrogenation of Aromatic Substrates. *Journal of Catalysis* **2017**, *354*, 113–127. https://doi.org/10.1016/j.jcat.2017.08.010.

(116) Ernst, J. B.; Muratsugu, S.; Wang, F.; Tada, M.; Glorius, F. Tunable Heterogeneous Catalysis: N-Heterocyclic Carbenes as Ligands for Supported Heterogeneous Ru/K-Al_2O_3 Catalysts to Tune Reactivity and Selectivity. *Journal of the American Chemical Society* **2016**, *138* (34), 10718–10721. https://doi.org/10.1021/jacs.6b03821.

(117) Lepron, M.; Daniel-Bertrand, M.; Mencia, G.; Chaudret, B.; Feuillastre, S.; Pieters, G. Nanocatalyzed Hydrogen Isotope Exchange. *Accounts of Chemical Research* **2021**, 54, 6, 1465–1480. https://doi.org/10.1021/acs.accounts.0c00721.

(118) Yadav, R. A.; Singh, I. S. Vibrational Studies of Trifluoromethyl Benzene Derivatives-III. p-Trifluoromethyl Aniline. *Spectrochimica Acta Part A: Molecular Spectroscopy* **1985**, *41* (1–2), 191–197. https://doi.org/10.1016/0584-8539(85)80096-9.

(119) Ribeiro-Claro, P. J. A.; Teixeira-Dias, J. J. C.; Gordon, R. D.; Hollas, J. M. Vibration Wavenumbers of 3-Aminobenzotrifluoride in the Ground and S1 Electronic States from Its Infrared, Raman, and Supersonic Jet S1-S0 Fluorescence Spectra. *Journal of Molecular Spectroscopy* **1991**, *150* (1), 46–55. https://doi.org/10.1016/0022-2852(91)90192-D.

(120) García.G.; Rodríguez, P.; Rosca, V.; Koper, M. T. M. Fourier Transform Infrared Spectroscopy Study of CO Electro-Oxidation on Pt(111) in Alkaline Media. *Langmuir* **2009**, *25* (23), 13661–13666. https://doi.org/10.1021/la902251z.

(121) Katayama, Y.; Giordano, L.; Rao, R. R.; Hwang, J.; Muroyama, H.; Matsui, T.; Eguchi, K.; Shao-Horn, Y. Surface (Electro)Chemistry of CO_2 on Pt Surface: An in Situ Surface-Enhanced Infrared Absorption Spectroscopy Study. *Journal of Physical Chemistry C* **2018**, *122* (23), 12341–12349. https://doi.org/10.1021/acs.jpcc.8b03556.

(122) Trujillo, M. J.; Strausser, S. L.; Becca, C.; Dejesus, J. F.; Jensen, L.; Jenkins, D. M.; Camden, J. P. Using SERS to Understand the Binding of N - Heterocyclic Carbenes to Gold Surfaces. *The Journal of Physical Chemistry Letters* **2018**, 9 (23), 6779–6785. https://doi.org/10.1021/acs.jpclett.8b02764.

(123) Amende, M.; Gleichweit, C.; Werner, K.; Schernich, S.; Zhao, W.; Lorenz, M. P. A.; Höfert, O.; Papp, C.; Koch, M.; Wasserscheid, P.; Laurin, M.; Steinrück, H. P.; Libuda, J. Model Catalytic Studies of Liquid Organic Hydrogen Carriers: Dehydrogenation and Decomposition Mechanisms of Dodecahydro-n-Ethylcarbazole on Pt(111). *ACS Catalysis* **2014**, *4* (2), 657–665. https://doi.org/10.1021/cs400946x.

(124) Gleichweit, C.; Amende, M.; Bauer, U.; Schernich, S.; Höfert, O.; Lorenz, M. P. A.; Zhao, W.; Müller, M.; Koch, M.; Bachmann, P.; Wasserscheid, P.; Libuda, J.; Steinrück, H. P.; Papp, C. Alkyl Chain Length-Dependent Surface Reaction of Dodecahydro-N-Alkylcarbazoles on Pt Model Catalysts. *Journal of Chemical Physics* **2014**, *140* (20), 4711. https://doi.org/10.1063/1.4875921.

(125) Land, T. A.; Michely, T.; Behm, R. J.; Hemminger, J. C.; Comsa, G. STM Investigation of the Adsorption and Temperature Dependent Reactions of Ethylene on Pt(111). *Applied Physics A Solids and Surfaces* **1991**, *53* (5), 414–417. https://doi.org/10.1007/BF00348154.

(126) Malik, I. J.; Brubaker, M. E.; Trenary, M. Infrared Spectroscopy of Ethylidyne on Pt(111). *Journal of Electron Spectroscopy and Related Phenomena* **1987**, *45* (C), 57–63. https://doi.org/10.1016/0368-2048(87)80054-3.

(127) Nakamura, M.; Ito, M. Infrared Spectroscopic Study of Water Coadsorbed with Na on the Ru(001) Surface. *Surface Science* **2002**., 502, 144–148. https://doi.org/10.1016/S0039-6028(01)01920-3.

(128) Garbarino, G.; Bellotti, D.; Finocchio, E.; Magistri, L.; Busca, G. Methanation of Carbon Dioxide on Ru/Al_2O_3: Catalytic Activity and Infrared Study. *Catalysis Today* **2016**, *277*, 21–28. https://doi.org/10.1016/j.cattod.2015.12.010.

(129) Jia, X.; An, W. Adsorption of Monocyclic Aromatics on Transition Metal Surfaces: Insight into Variation of Binding Strength from First-Principles. *Journal of Physical Chemistry C* **2018**, *122* (38), 21897–21909. https://doi.org/10.1021/acs.jpcc.8b06321.

(130) Avery, N. R. Adsorption of Hexafluoroacetone on Pt(111): Is Bonding End-on (H1) or Side-on (H2)? *Langmuir* **1985**, *1* (1), 162–166. https://doi.org/10.1021/la00061a029.

(131) Jensen, M. B.; Jenks, C. J.; Thiel, P. A.; Pylant, E. D.; White, J. M. Reactivity and Structure of CF_3I on Ru (001). **1995**, 99 (21), 8736–8744. https://doi.org/10.1021/j100021a045.

(132) Armentrout, D. D.; Grassian, V. H. Vibrational Spectroscopy of CF_x (x = 2 and 3) Groups Adsorbed on Pt(111). *Langmuir* **1994**, *10* (7), 2071–2076. https://doi.org/10.1021/la00019a009.

(133) Krzykawska, A.; Wróbel, M.; Kozieł, K.; Cyganik, P. N-Heterocyclic Carbenes for the Self-Assembly of Thin and Highly Insulating Monolayers with High Quality and Stability. *ACS Nano* **2020**, *14* (5), 6043–6057. https://doi.org/10.1021/acsnano.0c01733.

(134) Green, J. H. S.; Harrison, D. J. Vibrational Spectra of Benzene Derivatives-XXII. Benzotrifluoride and Mono-Substituted Derivatives. *Spectrochimica Acta Part A: Molecular Spectroscopy* **1977**, *33* (9), 837–842. https://doi.org/10.1016/0584-8539(77)80080-9.

(135) Chang, K.; Chen, J. G.; Lu, Q.; Cheng, M. J. Grand Canonical Quantum Mechanical Study of the Effect of the Electrode Potential on N-Heterocyclic Carbene Adsorption on Au Surfaces. *Journal of Physical Chemistry C* **2017**, *121* (39), 24618–24625. https://doi.org/10.1021/acs.jpcc.7b07866.

(136) Mao, J.; Xu, P.; Zhou, Z.; Zhou, Y.; Tang, Y. Eelectrochemical Evaluation of Self-Assembled Monolayers of N-Heterocyclic Carbenes on Gold and DFT Studies. *Journal of the Electrochemical Society* **2021**, *168* (1), 6513. https://doi.org/10.1149/1945-7111/abdc5d.

(137) Steinhauer, J.; Bachmann, P.; Freiberger, E. M.; Bauer, U.; Steinrück, H. P.; Papp, C. Model Catalytic Studies of Liquid Organic Hydrogen Carriers: Indole/Indoline/Octahydroindole on Ni(111). *Journal of Physical Chemistry C* **2020**, *124* (41), 22559–22567. https://doi.org/10.1021/acs.jpcc.0c06988.

(138) Oudghiri-Hassani, H.; Siaj, M.; McBreen, P. H. Origins of the High Thermal Stability of Alkylidene Groups on the Surface of β-Mo_2C. *Journal of Physical Chemistry C* **2007**, *111* (16), 5954–5962. https://doi.org/10.1021/jp0665224.

(139) Jensen, M. B.; Myler, U.; Jenks, C. J.; Thiel, P. A.; Pylant, E. D.; White, J. M. Reactivity and Structure of CF_3I on Ru(001). *Journal of physical chemistry* **1995**, *99* (21), 8736–8744. https://doi.org/10.1021/j100021a045.

(140) Garnica, M.; Stradi, D.; Calleja, F.; Barja, S.; Díaz, C.; Alcamí, M.; Arnau, A.; Vázquez De Parga, A. L.; Martín, F.; Miranda, R. Probing the Site-Dependent Kondo Response of Nanostructured Graphene with Organic Molecules. *Nano Letters* **2014**, *14* (8), 4560–4567. https://doi.org/10.1021/nl501584v.

(141) Daukiya, L.; Seibel, J.; de Feyter, S. Chemical Modification of 2D Materials Using Molecules and Assemblies of Molecules. *Advances in Physics: X* **2019**, *4* (1), 1625723. https://doi.org/10.1080/23746149.2019.1625723.

(142) Bottari, G.; Ángeles Herranz, M.; Wibmer, L.; Volland, M.; Rodríguez-Pérez, L.; Guldi, D. M.; Hirsch, A.; Martín, N.; D'Souza, F.; Torres, T. Chemical Functionalization and Characterization of Graphene-Based Materials. *Chemical Society Reviews* **2017**, *46* (15), 4464–4500. https://doi.org/10.1039/c7cs00229g.

(143) Chua, C. K.; Ambrosi, A.; Pumera, M. Introducing Dichlorocarbene in Graphene. *Chemical Communications* **2012**, *48* (43), 5376–5378. https://doi.org/10.1039/c2cc31936e.

(144) Clancy, A. J.; Au, H.; Rubio, N.; Coulter, G. O.; Shaffer, M. S. P. Understanding and Controlling the Covalent Functionalisation of Graphene. *Dalton Transactions* **2020**, *49* (30), 10308–10318. https://doi.org/10.1039/d0dt01589j.

(145) Yu, M.; Chen, C.; Liu, Q.; Mattioli, C.; Sang, H.; Shi, G.; Huang, W.; Shen, K.; Li, Z.; Ding, P.; Guan, P.; Wang, S.; Sun, Y.; Hu, J.; Gourdon, A.; Kantorovich, L.; Besenbacher, F.; Chen, M.; Song, F.; Rosei, F. Long-Range Ordered and Atomic-Scale Control of Graphene Hybridization by Photocycloaddition. *Nature Chemistry* **2020**, *12* (11), 1035–1041. https://doi.org/10.1038/s41557-020-0540-2.

(146) Rodríguez-Pérez, L.; Herranz, Á.; Martín, N. The Chemistry of Pristine Graphene. *Chemical Communications* **2013**, *49* (36), 3721–3735. https://doi.org/10.1039/c3cc38950b.

(147) Plutnar, J.; Pumera, M.; Sofer, Z. The Chemistry of CVD Graphene. *Journal of Materials Chemistry C* **2018**, *6*, 6082-6101. https://doi.org/10.1039/c8tc00463c.

(148) Park, J.; Yan, M. Covalent Functionalization of Graphene with Reactive Intermediates. *Accounts of Chemical Research* **2013**, *46* (1), 181–189. https://doi.org/10.1021/ar300172h.

(149) Zhong, X.; Jin, J.; Li, S.; Niu, Z.; Hu, W.; Li, R.; Ma, J. Aryne Cycloaddition: Highly Efficient Chemical Modification of Graphene. *Chemical Communications* **2010**, *46* (39), 7340–7342. https://doi.org/10.1039/c0cc02389b.

(150) Yang, X.; Chen, F.; Kim, M. A.; Liu, H.; Wolf, L. M.; Yan, M. On the Reactivity Enhancement of Graphene by Metallic Substrates towards Aryl Nitrene Cycloadditions. *Chemistry – A European Journal* **2021**, 27 (29), 1–11. https://doi.org/10.1002/chem.202100227.

(151) Strom, T. A.; Dillon, E. P.; Hamilton, C. E.; Barron, A. R. Nitrene Addition to Exfoliated Graphene: A One-Step Route to Highly Functionalized Graphene. *Chemical Communications* **2010**, *46* (23), 4097–4099. https://doi.org/10.1039/c001488e.

(152) Sarkar, S.; Bekyarova, E.; Niyogi, S.; Haddon, R. C. Diels-Alder Chemistry of Graphite and Graphene: Graphene as Diene and Dienophile. *Journal of the American Chemical Society* **2011**, *133* (10), 3324–3327. https://doi.org/10.1021/ja200118b.

(153) Paulus, G. L. C.; Wang, Q. H.; Strano, M. S. Covalent Electron Transfer Chemistry of Graphene with Diazonium Salts. *Accounts of Chemical Research* **2013**, *46* (1), 160–170. https://doi.org/10.1021/ar300119z.

(154) Ossonon, B. D.; Bélanger, D. Functionalization of Graphene Sheets by the Diazonium Chemistry during Electrochemical Exfoliation of Graphite. *Carbon* **2017**, *111*, 83–93. https://doi.org/10.1016/j.carbon.2016.09.063.

(155) Niyogi, S.; Bekyarova, E.; Itkis, M. E.; Zhang, H.; Shepperd, K.; Hicks, J.; Sprinkle, M.; Berger, C.; Lau, C. N.; Deheer, W. A.; Conrad, E. H.; Haddon, R. C. Spectroscopy of Covalently Functionalized Graphene. *Nano Letters* **2010**, *10* (10), 4061–4066. https://doi.org/10.1021/nl1021128.

(156) Sainsbury, T.; Passarelli, M.; Naftaly, M.; Gnaniah, S.; Spencer, S. J.; Pollard, A. J. Covalent Carbene Functionalization of Graphene: Toward Chemical Band-Gap Manipulation. *ACS Applied Materials and Interfaces* **2016**, *8* (7), 4870–4877. https://doi.org/10.1021/acsami.5b10525.

(157) Jiang, D. E.; Sumpter, B. G.; Dai, S. How Do Aryl Groups Attach to a Graphene Sheet? *Journal of Physical Chemistry B* **2006**, *110* (47), 23628–23632. https://doi.org/10.1021/jp065980.

(158) Abellán, G.; Schirowski, M.; Edelthalhammer, K. F.; Fickert, M.; Werbach, K.; Peterlik, H.; Hauke, F.; Hirsch, A. Unifying Principles of the Reductive Covalent Graphene Functionalization. *Journal of the American Chemical Society* **2017**, *139* (14), 5175–5182. https://doi.org/10.1021/jacs.7b00704.

(159) Ulbricht, H.; Zacharia, R.; Cindir, N.; Hertel, T. Thermal Desorption of Gases and Solvents from Graphite and Carbon Nanotube Surfaces. *Carbon* **2006**, 44 (14), 2931–2942. https://doi.org/10.1016/j.carbon.2006.05.040.

(160) Björk, J.; Hanke, F.; Palma, C. A.; Samori, P.; Cecchini, M.; Persson, M. Adsorption of Aromatic and Anti-Aromatic Systems on Graphene through π-π Stacking. *Journal of Physical Chemistry Letters* **2010**, *1* (23), 3407–3412. https://doi.org/10.1021/jz101360k.

(161) van Gorp, H.; Walke, P.; Teyssandier, J.; Hirsch, B. E.; Uji-I, H.; Tahara, K.; Tobe, Y.; van der Auweraer, M.; de Feyter, S. On the Thermal Stability of Aryl Groups Chemisorbed on Graphite. *Journal of Physical Chemistry C* **2020**, *124* (3), 1980–1990. https://doi.org/10.1021/acs.jpcc.9b09808.

(162) Sivapragasam, N.; Nayakasinghe, M. T.; Chakradhar, A.; Burghaus, U. Effects of the Support on the Desorption Kinetics of n-Pentane from Graphene: An Ultrahigh Vacuum Adsorption Study. *Journal of Vacuum Science & Technology A: Vacuum, Surfaces, and Films* **2017**, *35* (6), 1404 https://doi.org/10.1116/1.4989814.

(163) Chakradhar, A.; Trettel, K.; Burghaus, U. Benzene Adsorption on Ru(0001) and Graphene/Ru(0001) - How to Synthesize Epitaxial Graphene without STM or LEED? *Chemical Physics Letters* **2013**, *590*, 146-152. https://doi.org/10.1016/j.cplett.2013.10.069.

(164) Voloshina, E.; Berdunov, N.; Dedkov, Y. Restoring a Nearly Free-Standing Character of Graphene on Ru(0001) by Oxygen Intercalation. *Scientific Reports* **2016**, *6* (1), 1–10. https://doi.org/10.1038/srep20285.

(165) Deng, S.; Rhee, D.; Lee, W. K.; Che, S.; Keisham, B.; Berry, V.; Odom, T. W. Graphene Wrinkles Enable Spatially Defined Chemistry. *Nano Letters* **2019**, *19* (8), 5640–5646. https://doi.org/10.1021/acs.nanolett.9b02178.

(166) Brülls, S. M.; Cantatore, V.; Wang, Z.; Tam, P. L.; Malmberg, P.; Stubbe, J.; Sarkar, B.; Panas, I.; Mårtensson, J.; Eigler, S. Evidence for Electron Transfer between Graphene and Non-Covalently Bound π-Systems. *Chemistry - A European Journal* **2020**, *26* (29), 6694. https://doi.org/10.1002/chem.202000488.

(167) Land, T. A.; Michely, T.; Behm, R. J.; Hemminger, J. C.; Comsa, G. Direct Observation of Surface Reactions by Scanning Tunneling Microscopy: Ethylene-Tethylidyne → Carbon Particles → Graphite on Pt(111). *The Journal of Chemical Physics* **1992**, *97* (9), 6774–6783. https://doi.org/10.1063/1.463655.

(168) Johánek, V.; Nehasil, V.; Skála, T.; Tsud, N. Carbon Chain Length Dependence of Graphene Formation via Thermal Decomposition of Alkenes on Pt(111). *Journal of Physical Chemistry C* **2019**, *123* (13), 7911–7921. https://doi.org/10.1021/acs.jpcc.8b07165.

(169) Kim, H. W.; Ko, W.; Ku, J.; Kim, Y.; Park, S.; Hwang, S. Evolution of Graphene Growth on Pt(111): From Carbon Clusters to Nanoislands. *Journal of Physical Chemistry C* **2017**, *121* (45), 25074–25078. https://doi.org/10.1021/acs.jpcc.7b06540.

(170) Liang, Z.; Khosravian, H.; Uhl, A.; Meyer, R. J.; Trenary, M. Graphene Domain Boundaries on Pt(111) as Nucleation Sites for Pt Nanocluster Formation. *Surface Science* **2012**, *606* (21–22), 1643–1648. https://doi.org/10.1016/j.susc.2012.07.005.

(171) Wang, B.; Bocquet, M. L.; Marchini, S.; Günther, S.; Wintterlin, J. Chemical Origin of a Graphene Moiré Overlayer on Ru(0001). *Physical Chemistry Chemical Physics* **2008**, *10* (24), 3530–3534. https://doi.org/10.1039/b801785a.

(172) Zhang, H. G.; Sun, J. T.; Low, T.; Zhang, L. Z.; Pan, Y.; Liu, Q.; Mao, J. H.; Zhou, H. T.; Guo, H. M.; Du, S. X.; Guinea, F.; Gao, H. J. Assembly of Iron Phthalocyanine and Pentacene Molecules on a Graphene Monolayer Grown on Ru(0001). *Physical Review B - Condensed Matter and Materials Physics* **2011**, *84* (24), 1–6. https://doi.org/10.1103/PhysRevB.84.245436.

(173) Novotny, Z.; Nguyen, M. T.; Netzer, F. P.; Glezakou, V. A.; Rousseau, R.; Dohnálek, Z. Formation of Supported Graphene Oxide: Evidence for Enolate Species. *Journal of the American Chemical Society* **2018**, *140* (15), 5102–5109. https://doi.org/10.1021/jacs.7b12791.

(174) Martoccia, D.; Willmott, P. R.; Brugger, T.; Björck, M.; Günther, S.; Schlepütz, C. M.; Cervellino, A.; Pauli, S. A.; Patterson, B. D.; Marchini, S.; Wintterlin, J.; Moritz, W.; Greber, T. Graphene on Ru(0001): A 25 × 25 Supercell. *Physical Review Letters* **2008**, *101* (12), 1–4. https://doi.org/10.1103/PhysRevLett.101.126102.

(175) Martoccia, D.; Björck, M.; Schlepütz, C. M.; Brugger, T.; Pauli, S. A.; Patterson, B. D.; Greber, T.; Willmott, P. R. Graphene on Ru(0001): A Corrugated and Chiral Structure. *New Journal of Physics* **2010**, *12* (4), 3028. https://doi.org/10.1088/1367-2630/12/4/043028.

(176) Pan, Y.; Zhang, H.; Shi, D.; Sun, J.; Du, S.; Liu, F.; Gao, H. J. Highly Ordered, Millimeter-Scale, Continuous,Single-Crystalline Graphene Monolayer Formed on Ru (0001). *Advanced Materials* **2009**, *21* (27), 2777–2780. https://doi.org/10.1002/adma.200800761.

(177) Marchini, S.; Günther, S.; Wintterlin, J. Scanning Tunneling Microscopy of Graphene on Ru (0001). **2007**, *76* (7), 1–9. https://doi.org/10.1103/PhysRevB.76.075429.

(178) Dedkov, Y.; Voloshina, E. Spectroscopic and DFT Studies of Graphene Intercalation Systems on Metals. *Journal of Electron Spectroscopy and Related Phenomena* **2017**, *219*, 77–85. https://doi.org/10.1016/j.elspec.2016.11.012.

(179) Li, T.; Yarmoff, J. A. Intercalation and Desorption of Oxygen between Graphene and Ru(0001) Studied with Helium Ion Scattering. *Physical Review B* **2017**, *96* (15), 5441. https://doi.org/10.1103/PhysRevB.96.155441.

(180) Ulstrup, S.; Lacovig, P.; Orlando, F.; Lizzit, D.; Bignardi, L.; Dalmiglio, M.; Bianchi, M.; Mazzola, F.; Baraldi, A.; Larciprete, R.; Hofmann, P.; Lizzit, S. Photoemission Investigation of Oxygen Intercalated Epitaxial Graphene on Ru(0001). *Surface Science* **2018**, *678*, 57–64. https://doi.org/10.1016/j.susc.2018.03.017.

(181) Fu, Q.; Bao, X. Surface Chemistry and Catalysis Confined under Two-Dimensional Materials. *Chemical Society Reviews* **2017**, *46*, 1842–1874. https://doi.org/10.1039/c6cs00424e.

(182) Jang, W. J.; Kim, H.; Jeon, J. H.; Yoon, J. K.; Kahng, S. J. Recovery and Local-Variation of Dirac Cones in Oxygen-Intercalated Graphene on Ru(0001) Studied Using Scanning Tunneling Microscopy and Spectroscopy. *Physical Chemistry Chemical Physics* **2013**, *15* (38), 16019–16023. https://doi.org/10.1039/c3cp52431k.

(183) Sutter, P. Scanning Tunneling Microscopy in Surface Science. *Springer Handbooks* **2019**, 969–1024. https://doi.org/10.1007/978-3-030-00069-1_27.

(184) Dong, A.; Fu, Q.; Wei, M.; Liu, Y.; Ning, Y.; Yang, F.; Bluhm, H.; Bao, X. Facile Oxygen Intercalation between Full Layer Graphene and Ru(0001) under Ambient Conditions. *Surface Science* **2015**, *634*, 37–43. https://doi.org/10.1016/j.susc.2014.10.008.

(185) Cui, Y.; Fu, Q.; Zhang, H.; Tan, D.; Bao, X. Dynamic Characterization of Graphene Growth and Etching by Oxygen on Ru(0001) by Photoemission Electron Microscopy. *Journal of Physical Chemistry C* **2009**, *113* (47), 20365–20370. https://doi.org/10.1021/jp907949a.

(186) Starodub, E.; Bartelt, N. C.; McCarty, K. F. Oxidation of Graphene on Metals. *Journal of Physical Chemistry C* **2010**, *114* (11), 5134–5140. https://doi.org/10.1021/jp912139e.

(187) Zhang, H.; Fu, Q.; Cui, Y.; Tan, D.; Bao, X. Growth Mechanism of Graphene on Ru(0001) and O_2 Adsorption on the Graphene/ Ru(0001) Surface. *Journal of Physical Chemistry C* **2009**, *113* (19), 8296–8301. https://doi.org/10.1021/jp810514u.

(188) Xu, C.; Song, S.; Liu, Z.; Chen, L.; Wang, L.; Fan, D.; Kang, N.; Ma, X.; Cheng, H. M.; Ren, W. Strongly Coupled High-Quality Graphene/2D Superconducting Mo_2C Vertical Heterostructures with Aligned Orientation. *ACS Nano* **2017**, *11* (6), 5906–5914. https://doi.org/10.1021/acsnano.7b01638.

(189) Guillén-Cervantes, A.; Rivera-Alvarez, Z.; López-López, M.; López-Luna, E.; Hernández-Calderón, I. GaAs Surface Oxide Desorption by Annealing in Ultra High Vacuum. *Thin Solid Films* **2000**, *373* (1–2), 159–163. https://doi.org/10.1016/S0040-6090(00)01126-3.

(190) Ba, K.; Wang, G.; Ye, T.; Wang, X.; Sun, Y.; Liu, H.; Hu, A.; Li, Z.; Sun, Z. Single Faceted Two-Dimensional Mo_2C Electrocatalyst for Highly Efficient Nitrogen Fixation. *ACS Catalysis* **2020**, *10* (14), 7864–7870. https://doi.org/10.1021/acscatal.0c01127.

(191) Verger, L.; Xu, C.; Natu, V.; Cheng, H. M.; Ren, W.; Barsoum, M. W. Overview of the Synthesis of MXenes and Other Ultrathin 2D Transition Metal Carbides and Nitrides. *Current Opinion in Solid State and Materials Science* **2019**, *23* (3), 149–163. https://doi.org/10.1016/j.cossms.2019.02.001.

(192) Zahidi, E. M.; Oudghiri-Hassani, N.; McBreen, P. H. Formation of Thermally Stable Alkylidene Layers on a Catalytically Active Surface. *Nature* **2001**, *409* (6823), 1023–1026. https://doi.org/10.1038/35059047.

(193) Siaj, M.; Temprano, I.; Dubuc, N.; McBreen, P. H. Preparation and Olefin-Metathesis Activity of Cyclopentylidene-Oxo Initiator Sites on a Molybdenum Carbide Surface. *Journal of Organometallic Chemistry* **2006**, *691* (24–25), 5497–5504. https://doi.org/10.1016/j.jorganchem.2006.09.033.

(194) Siaj, M.; Reed, C.; Oyama, S. T.; Scott, S. L.; McBreen, P. H. Dissociation of Acetaldehyde on β-Mo_2C to Yield Ethylidene and Oxo Surface Groups: A Possible Pathway for Active Site Formation in Heterogeneous Olefin Metathesis. *Journal of the American Chemical Society* **2004**, *126* (31), 9514–9515. https://doi.org/10.1021/ja048640f.